KU LEUVEN

ARENBERG DOCTORAL SCHOOL
FACULTY OF ENGINEERING SCIENCE

Phthalocyanine-based organic solar cells and photodetectors

Kjell Cnops

Dissertation presented
in partial fulfilment of the
requirements for the degree of
PhD in Engineering Science

September 2015

Phthalocyanine-based organic solar cells and photodetectors

Kjell Cnops

Jury:
Yves Willems, chair
Paul Heremans, supervisor
Jan Genoe, co-supervisor
Jef Poortmans
Andre Stesmans
Koen Vandewal (TU Dresden, DE)
Barry Rand (Princeton University, US)

Dissertation presented
in partial fulfilment of the
requirements for the degree of
PhD in Engineering Science

In collaboration with imec
Kapeldreef 75
B-3001 Heverlee - Belgium

September 2015

Uitgegeven in eigen beheer, Kjell Cnops, Leuven

Dankwoord

Dit zijn de eerste en de laatste pagina's van mijn 'werkje': de eerste pagina's die iedereen zal lezen, en de laatste pagina's die ik zal schrijven. De voorbereiding van dit werkje heeft ongeveer vier jaar in beslag genomen. Tijdens deze periode hebben uiteraard heel wat mensen mij op weg geholpen en in de juiste richting gestuurd. De volgende 129 pagina's zijn daarom het resultaat van de samenwerking en ondersteuning van al deze mensen, die ik bij deze uitdrukkelijk wil bedanken.

Ten eerste wil ik mijn promotor Paul Heremans bedanken om mij de kans te geven een doctoraatsproject uit te voeren onder zijn begeleiding. Door zijn enorme ervaring kon hij mijn onderzoek altijd bijsturen met verhelderende inzichten en nieuwe suggesties. Daarnaast wil ik Jan Genoe bedanken. Ook voordat hij officieel mijn copromotor werd, hadden wij al interessante discussies over mijn onderzoeksresultaten. Als lid van mijn begeleidingscommissie leverden ook Jef Poortmans en Andre Stesmans nuttige feedback tijdens de tussentijdse evaluaties. At the private defense also Koen Vandewal and Barry Rand raised critical questions and comments, which improved the quality of this work. Uiteraard wil ik ook de sympathieke Yves Willems bedanken om de preliminaire verdediging in goede banen te leiden. Ik ben er zeker van dat zijn aanwezigheid ook de publieke verdediging iets minder onaangenaam zal maken.

Barry has the honor to be acknowledged twice here. During the first part of my PhD study he was always ready to answer all my questions and assist me to design clever experiments. Also after he left imec, he took the time to continue discussions about my work. Nadat Barry vertrok, heeft David deze rol met glans overgenomen en stond hij mij met raad en daad bij. De dagelijkse begeleiding van Barry en David vormt dan ook de onmisbare basis van dit werk. Nog voordat ik aan mijn doctoraatsonderzoek begon, waren het Cédric en Karolien die mij introduceerden in de wereld van organische halfgeleiders. Hun enthousiaste begeleiding tijdens mijn masterproef heeft mij grotendeels overtuigd een doctoraatsopleiding te beginnen. Ook nadien waren zij nog bereid mij te helpen met AFM of PL experimenten. Thank you!

Vier jaar geleden startte ik dus mijn doctoraatsproject in het toenmalige OPV team. Besides Barry and David, the research skills of Afshin, Bobby and Griet formed the strong basis of this team, which was later reinforced by Tamara and Ulrich. Eventually also Bart, Guy and Sylvester joined the TFPV-group in the 'aquarium'. It was Tom's job to manage all these changes and ensure the continued successes of this group. I want to thank all of them, not only for providing scientific help whenever possible, but mainly for creating a great work environment every day. I also want to wish good luck to the PhD students of the group - a.k.a 'the solar boys'. Jeffrey - a.k.a. Jeffreypedia - please never stop sharing random facts and trivia, maybe someday someone will find some useful information in this endless vessel of knowledge. João, jouw Nederlands is nu bijna beter dan dat van mij, blijven oefenen! I also know that Weiming, the 'founding father' of perovskites solar cells in our group, will make many more record devices, while Manoj will bridge the worlds of Si and thin-film photovoltaics. And I'm sure Lucija, who just started her PhD study, will fit perfectly in this amazing group.

Ook mijn voorgangers, die hun doctoraat reeds hebben behaald en ondertussen de groep verlaten hebben, wil ik bedanken. I always regarded my predecessors as role models, and I tried to combine the perfectionism of Eszter and Karolien with the (apparent?) relaxedness of Bjoern and Bregt. Adrian, Benjamin, en Maarten kwamen dan weer vaak op de proppen met praktische tips over het doctoraatsleven. And of course I have to thank Max, who helped me with my PL measurements and was always ready to start a discussion about our experiments. Allemaal bedankt!

Uiteraard ben ik de onvoorwaardelijke hulp van Erwin niet vergeten. In de vroege uurtjes was hij al in de o-lijn bezig met Lesker-runs, het reinigen van ITO-substraten of de purificatie van onze materialen. Dit was een geweldige luxe waarvan ik dan ook enorm geprofiteerd heb. Daarom dus een 'special thanks' aan Erwin! Ook de oneindige inzet van Luuk is bewonderenswaardig. Dankzij hem was het altijd een plezier om in de labo's te werken. Ondertussen heeft Sven al bewezen dat hij een waardige opvolger is. Voor het administratieve werk was de hulp van Inge onontbeerlijk. Met een glimlach regelde zij alle praktische zaken, afspraken met Paul en Jan, en uiteindelijk ook mijn doctoraatsverdediging. Hartelijk dank daarvoor!

Thanks to all LAE-people for the animated, enjoyable, fascinating and funny conversations we had in the lab, during lunch, or during one of the many birthday-cake breaks. As this group of people keeps expanding, I hope I don't forget anyone: thank you Aga, Ajay, Albert, Alexander, Alfonso, Brecht, Cédric, Florian, Jeong-Hwan, Kris, Maarten, Manoj, Marc, Marina, Myriam, Pavlo, Pawel, Peter, Robby, Sarah, Sebastien, Soeren, Stan, Steve, Tony, and Xubin.

En dan zijn er nog een aantal mensen die ik vooral wil bedanken voor hun niet-wetenschappelijke ondersteuning, vaak in de vorm van aan bezoek aan de Oude Markt, een gezellige BBQ of een pensenavond: Bruno, Dries, Evelien, Katleen, Koen, Michiel, Nathan, Pieter, Somya, en Zeger. Jullie hebben mijn leven de voorbije jaren gevuld met vreugde en plezier! En ik hoop uiteraard dat jullie dit in de toekomst ook blijven doen.

De Pol en de Moe, bedankt voor het genetisch materiaal dat jullie mij gegeven hebben. Al 27 jaar staan jullie klaar voor mij, en steunen mij in alles wat ik doe. Zonder jullie kon ik onmogelijk het punt bereikt hebben waar ik nu sta. Ook mijn 'grote' zus Vanja moet ik bedanken. Zij was altijd een jaar voor op schema, dus heb ik veel van haar kunnen ‘afkijken’. Ik ben dus blij dat ik nu eindelijk eens de eerste ben in iets: een doctoraat behalen.

Ten slotte wil ik mijn vrouwtje Sofie bedanken om dit werkje te lay-outen ... en ook omdat jij gewoon de beste bent!

Kjell Cnops
Leuven, September 2015

Abstract

The integration of organic semiconductors in optoelectronic devices has generated a wide range of innovative applications, from flexible displays to light-weight or semi-transparent solar cells. This dissertation investigates the use of phthalocyanines, a specific class of organic semiconducting molecules, as the active components in organic solar cells and organic photodetectors. The unique optoelectronic properties of these molecules enable the development of new photodiode architectures with enhanced performance.

First, the fullerene acceptors in organic solar cells are replaced by subphthalocyanines. The strong absorption of visible light by these molecules improves the photocurrent generation, while the easy tunability of their frontier molecular orbital energy levels adjusts the open-circuit voltage. A systematic study of heterojunction energetics however reveals a trade-off between the open-circuit voltage and the photocurrent. The non-fullerene acceptors furthermore require the use of tailored electron transport layers to enable efficient electron extraction. Optimization of the device structure results in planar-heterojunction devices with a power conversion efficiency of 6.9% and an open-circuit voltage above 1 V, exceeding the performance of their fullerene-based counterparts. The photocurrent generation is further increased in multilayer device architectures. In a charge transfer cascade device with three active materials, in which *chloro boron subphthalocyanine* (SubPc) acts as an ambipolar interlayer, both heterojunctions are active and contribute to the photocurrent in parallel. Alternatively, in an energy transfer cascade device the photocurrent increases by an additional two-step exciton harvesting mechanism. Excitons first transfer from SubPc to *chloro boron subnaphthalocyanine* (SubNc) by long-range Förster resonance energy transfer, and consequently dissociate at the donor-acceptor interface. The obtained PCE of 8.4% is unprecedented for fullerene-free organic solar cells, and even surpasses many state-of-the-art evaporated single-junction cells. These results demonstrate that non-fullerene acceptors and multilayer cascade architectures are promising alternatives to conventional donor-fullerene organic solar cells.

The non-planar molecule *lead phthalocyanine* (PbPc) promotes absorption of near-infrared light (NIR) in organic photodiodes. Such NIR-sensitive photodetectors can be used in a large number of industrial and scientific applications. The detectivity of PbPc-based photodetectors is however limited by their high dark current density. Systematic modification of the device structure reveals the presumable origin of this high leakage current: the formation of interface dipoles and band bending facilitates electron injection in the PbPc layer. Suppression of the leakage current is therefore identified as a major challenge in the development of organic NIR photodetectors applications.

Beknopte samenvatting

De integratie van organische halfgeleiders in opto-elektronische componenten heeft verschillende innovatieve toepassingen mogelijk gemaakt, zoals flexibele beeldschermen of lichte, semi-transparante zonnecellen. Dit proefschrift onderzoekt het gebruik van ftalocyaninen, een specifieke klasse van halfgeleidende moleculen, als de actieve bouwstenen van organische zonnecellen en organische fotodetectoren. De unieke opto-elektronische eigenschappen van deze materialen leiden tot de ontwikkeling van vernieuwde architecturen voor organische fotodiodes, met verbeterde prestaties van hun toepassingen als gevolg.

Eerst worden subftalocyaninen getest als elektronenacceptor in organische zonnecellen, ter vervanging van de veelgebruikte fullerenen. De sterke absorptie van zichtbaar licht door deze moleculen verhoogt de geproduceerde elektrische stroom. Doordat de energieniveaus van de molecuulorbitalen eenvoudig kunnen aangepast worden, kan ook de openketenspanning verhoogd worden. Uit een systematisch studie van de energetische structuur aan de heterojunctie blijkt echter dat er een afweging tussen de openketenspanning en de stroomdichtheid in de zonnecel bestaat. Het gebruik van subftalocyaninen als acceptor vereist bovendien aangepaste transportlagen om de extractie van elektronen te vergemakkelijken. Door de lagenstructuur van de zonnecellen te optimaliseren wordt uiteindelijk een rendement van 6,9% gerealiseerd, met een openketenspanning groter dan 1 V. Deze waarden overtreffen zonnecellen met fullerenen als acceptor. De stroomproductie in een organische zonnecel kan verder verhoogd worden door het gebruik van meerlaagse architecturen. In een ladingstransfercascade met drie actieve materialen, waarbij *boor subftalocyanine chloride* (SubPc) fungeert als een ambipolaire tussenlaag, dragen beide heterojuncties bij tot de stroomproductie. Anderzijds kan een energietransfercascade de stroom in de zonnecel verhogen door een twee-staps excitondissociatieproces. Hierbij springen de excitonen eerst van SubPc naar *boor subnaftalocyanine chloride* (SubNc) door Förster-resonantie energietransfer, waarna ze dissociëren aan het grensvlak tussen de donor- en de acceptorlaag. Het behaalde rendement van 8,4% vormt een huidig record voor fullereen-vrije organische zonnecellen, en sluit zelfs aan bij de hoogste rendementen gerapporteerd voor enkelvoudige cellen. Deze resultaten tonen aan dat fullereen-vrije acceptoren en meerlaagse cascade-architecturen veelbelovende alternatieven vormen voor conventionele organische zonnecellen.

Het molecule *lood ftalocyanine* (PbPc) bevordert de absorptie van nabij-infrarood licht (NIR) in organische fotodiodes. Dergelijke NIR-gevoelige fotodetectoren kennen vele toepassingen in zowel de industriële als de wetenschappelijke wereld. De detectiviteit van fotodetectoren gebaseerd op PbPc wordt echter beperkt door hun grote donkerstroom. Door systematische wijzigingen aan de structuur van de fotodiode kan de vermoedelijke oorsprong van deze hoge donkerstroom bepaald worden: dipolen aan het oppervlak en bandenbuiging in de PbPc-laag vergemakkelijken de injectie van elektronen. Reductie van de lekstroom vormt dus een belangrijke uitdaging bij de verdere ontwikkeling van organische NIR fotodetectoren.

Contents

List of figures

List of tables

Abbreviations and symbols

A	Absorptance [%]
AFM	Atomic force microscopy
AM1.5G	Air mass 1.5 global solar spectrum
BCP	Bathocuproine
CT	Charge transfer
CuI	Copper iodide
D	Diffusion coefficient [m^2/s]
D^*	Specific detectivity [(cm·Hz$^{-1/2}$)/W]
DIP	Diindenoperylene
E_{CT}	CT state energy [eV]
E_{DA}	Donor-acceptor interface energy gap [eV]
EQE	External quantum efficiency [%]
ETL	Electron transport layer
FF	Fill factor [%]
FRET	Förster resonance energy transfer
HOMO	Highest occupied molecular orbital
HTL	Hole transport layer
IPES	Inverse photoemission spectroscopy
IQE	Internal quantum efficiency [%]
I_{SC}	Short-circuit current [mA]
ITO	Indium tin oxide
J	Current density [mA/cm^2]
J_0 , $J_{0,n}$	Saturation current density [mA/cm^2]
J_{photo}	Photocurrent density [mA/cm^2]
J_{SC}	Short-circuit current density [mA/cm^2]
k	Boltzman constant (= 8.617 x 10^{-5} eV/K)
k_{f}	Förster transfer rate [s^{-1}]
L_{D}	Exciton diffusion length [nm]
LUMO	Lowest unoccupied molecular orbital

n	Ideality factor / Exciton density [nm^{-3}]
NIR	Near-infrared
NPB	N,N′-di(1-naphthyl)-N,N′-diphenyl-(1,1′-biphenyl)-4,4′-diamine
OPD	Organic photodetector
OPV	Organic photovoltaics
PbPc	Lead phthalocyanine
Pc	Phthalocyanine
PCE	Power conversion efficiency [%]
PEDOT:PSS	Poly(3,4-ethylenedioxythiophene)-poly(styrenesulfonate)
P_{in}	Incident light intensity [mW/cm^2]
PL	Photoluminescence
Q	Exciton generation rate [nm^{-3} s^{-1}]
q	Elementary electric charge (= 1.602 x 10^{-19} C)
r	Intermolecular distance [nm]
R	Responsivity [mA/mW] / Reflectance [%]
R_0	Förster radius [nm]
RMS	Root mean square
R_{P}	Shunt resistance [$\Omega\cdot$cm^2]
R_{S}	Series resistance [$\Omega\cdot$cm^2]
SubNc	(Chloro boron) subnaphthalocyanine
SubPc	(Chloro boron) subphthalocyanine
T	Temperature [K]
Tc	Tetracene
UPS	Ultraviolet photoelectron spectroscopy
V	Voltage [V]
V_{OC}	Open-circuit voltage [V]
ZnPc	Zinc phthalocyanine
α-6T	α-sexithiophene
ϕ	Spectral photon flux [m$^{-2}\cdot$s$^{-1}\cdot$nm^{-1}] / Surface folding ratio
η_{PL}	Photoluminescence yield
λ	Wavelength [nm]
μ	Charge carrier mobility [cm^2/(V$\cdot$s)]
ρ	Molecular density [nm^{-3}]
τ	Exciton lifetime [s]

1. Introduction

Organic electronics is an emerging branch of electronics comprising the application of small organic molecules or polymers in various electronic and optoelectronic devices. The advantages of organic materials over the classical inorganic semiconductors (e.g. Si, Ge, and GaAs) include their mechanical flexibility and compatibility with low-temperature and low-cost deposition techniques. The use of organic semiconductors therefore enables the development of thin, light-weight, and flexible electronic components using cost-effective, large-area production processes.[1] Furthermore, the endless possible variations in molecular structure facilitates tuning of the optical and electronic properties of organic semiconductors. Hence, organic semiconductors have been exploited in a large variety of (opto)electronic devices, such as thin-film transistors (TFT), light-emitting diodes, solar cells, and sensors.[2–6] Applications exploiting the key benefits of organic semiconductors include

- flexible or rollable displays,
- cheap and disposable radio-frequency identification tags that store product information and can replace traditional barcodes,
- transparent and light-weight solar cells integrated in windows or textiles,
- large-area imagers for use in medical or scientific equipment,
- and various sensors for industrial process monitoring, security, or remote control.

While some of these innovative applications are still in an early conceptual or product development phase, several products employing organic components are already commercially available, for example in displays and lighting systems.

Despite the bright prospects, organic electronics faces certain technological challenges that hinder the realization of potential applications. For example, the power conversion efficiency of organic photovoltaics should be further increased to make this technology economically viable.[7] Likewise, circuit designs with increasing complexity will benefit from increased charge carriers mobility and reduced variability of TFT performance parameters. The rapid degradation of organic semiconductors under external stress factors furthermore limits the stability and lifetime of many applications. Also the upscaling to large-area production processes poses certain material requirements, such as the use of Earth-abundant, non-toxic, and environmentally friendly materials and solvents. To overcome these challenges an improved understanding of the physical processes involved in the operation of organic electronic devices is needed. Such knowledge provides guidelines to optimize the active materials, device design and processing.

This dissertation will focus on two applications of organic electronics, namely organic photovoltaics and organic photodetectors. Both applications are realized using an organic photodiode device structure. More specifically, phthalocyanines and subphthalocyanines will be investigated as the active materials in such photodiodes. This chapter provides the relevant background for the research described in this dissertation. First, the class of phthalocyanine and subphthalocyanine molecules is introduced. Next, a general overview of the structural, optical and electronic properties of organic semiconductors and thin films is given, followed by a review of the operation principles and device architectures of organic photodiodes. Also the basic characterization techniques to evaluate the performance of organic solar cells and photodetectors are discussed. This framework will clarify which material and device properties are essential for device performance enhancement. Finally, the research objectives of this work are formulated, and the content of the remaining chapters is sketched.

1.1 Phthalocyanines and subphthalocyanines

Phthalocyanines[8,9] (Pc) are organic molecules that consist of four isoindole subunits linked together through nitrogen atoms. Unsubstituted phthalocyanine, abbreviated H_2Pc, is a planar molecule which contains two hydrogen atoms in its central cavity. These hydrogens atoms can however be substituted by a divalent metal ion, forming two covalent and two coordination bonds with the surrounding nitrogen atoms (**Figure 1.1(a)**).[10] Most commonly transition-metal ions such as Cu, Zn, or Ni are used to form such metallophthalocyanines, but also metal-oxygen, metal-halide or metal-organic compounds can be used to fill the central cavity; for example in titanyl Pc (TiOPc) or chloro aluminium Pc (ClAlPc). All together, more than 70 elements of the periodic table are known to form coordination complexes with the Pc macrocycle.

Phthalocyanines were originally known as colorful dyes and pigments. Because they absorb visible light at wavelengths between 600 nm and 700 nm, most Pc complexes have an intense green or blue color.[11] Consequently, these molecules are commonly used as dyes in textiles and inks. However, phthalocyanines also possess interesting electronic properties due to their aromatic ring structure. Addition of peripheral or axial substituents to the molecular structure enables tailoring of the optical and electronic properties. As a consequence of this chemical versatility, phthalocyanines have been widely studied for application in organic thin-film transistors, light-emitting devices, thin-film solar cells, optical switches, molecular sensors, or even photosensitizers for photodynamic therapy or quantum computing.[12–16]

Phthalocyanines are thermally stable molecules and can be sublimed without decomposition. Therefore, thin Pc films can easily be applied by vacuum evaporation as the building blocks of many electronic and optoelectronic devices. Alternatively, peripheral substitution of Pc molecules with bulky groups or hydrocarbon chains enhances their solubility and permits thin-film deposition by solution-processing techniques. The macroscopic solid-state properties of such thin films are largely determined by the molecular interactions at the nanoscale. For example, the π-π molecular orbital overlap by cofacial stacking of the Pc molecules generally results in a high conductivity. Control of the solid-state phase in thin Pc films therefore enables further tuning of their optoelectronic properties.[14,17–19]

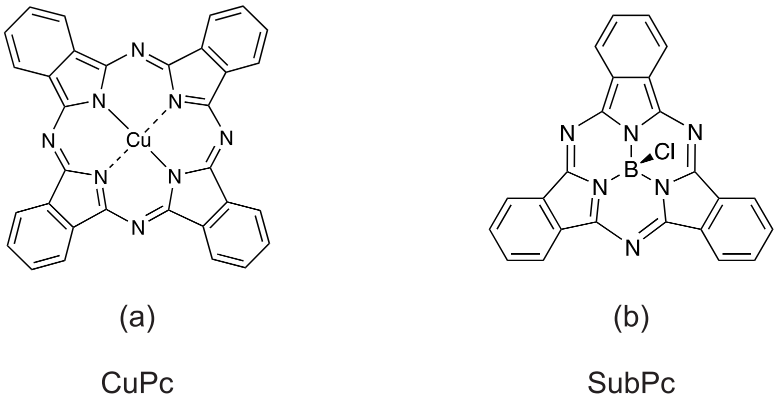

(a)

CuPc

(b)

SubPc

Figure 1.1: Molecular structure of (a) CuPc, exemplifying phthalocyanines containing a metal ion in the central cavity, and (b) SubPc, a prototypical subphthalocyanine.

Subphthalocyanines[20,21] are Pc homologues with three isoindole units instead of four. Only boron, which has the smallest atomic radius of all metals and metalloids, fits in the central cavity of the reduced macrocycle. Commonly this boron atom is covalently bonded to a halogen atom. The prototypical chloro boron subphthalocyanine (**Figure 1.1(b)**) will be simply abbreviated as SubPc in this work. Due to the removal of one isoindole unit, subphthalocyanine molecules assume a non-planar, cone-shaped structure.

Subphthalocyanines have only emerged during the last decade as promising materials in organic electronics, and were mainly explored as absorber in organic photovoltaics.[22] The smaller conjugated system shifts the absorption spectrum to smaller wavelengths, peaking around 560 nm to 600 nm, and results in the typical purple color of these compounds. Similar to phthalocyanines, the peripheral and axial ligands can be substituted by various functional groups, altering the optical and electronic properties of the molecule. Furthermore, the phenyl moieties can be replaced by naphthalene to form chloro boron subnaphthalocyanine (SubNc).[23] The extension of the conjugated system results in absorption of longer wavelengths.

In summary, the combination of strong absorption, semiconducting properties, thermal stability and chemical versatility makes phthalocyanines and subphthalocyanines ideal candidates for application in organic optoelectronic devices.

1.2 Organic semiconductors and thin-film properties

In general, organic semiconductors are carbon-based materials — either single molecules, oligomers or polymers — that show semiconducting behavior. Extensive reviews on the conduction mechanism in organic semiconductors can be found in the literature.[24–26] Briefly, in a conjugated system the overlap between p_z-orbitals of the sp^2-hybridized carbon atoms results in the formation of molecular π-orbitals. The electrons occupying these molecular π-orbitals are delocalized over the entire conjugated system. Conduction in a thin organic film then results from wavefunction overlap between such π-orbitals in neighboring conjugated systems.

Thin films of organic semiconductors form the basis of many organic optoelectronic devices. The thickness of these films typically varies from tens to several hundreds of nanometers. For polymer semiconductors, thin-film formation is only possible from solution-processing techniques, such as spin-coating, blade-coating or spray-coating. Small-weight organic molecules, on the other hand, can either be deposited by solution processing or by vacuum thermal evaporation.

The structural, electronic and optical properties of organic semiconducting films, and consequently the performance of organic optoelectronic devices, depends on both the molecular structure of the active materials, as well as the nanoscale organization in the deposited films. This section will therefore discuss the relevant material and thin-film properties that are involved in device operation. Because mainly phthalocyanine-related compounds are studied in this thesis, this section will emphasize the solid-state properties of small-molecule semiconductors. Nevertheless, most concepts addressed here are generalizable to polymeric semiconductors.

1.2.1 Intermolecular interactions and crystal structure

Individual molecules in organic thin films are held together by van der Waals forces, which include dispersion, induction and dipole interactions. These van der Waals forces are much weaker compared with the *intra*molecular covalent bonds. Yet, the weak *inter*molecular interactions mainly influence the physical properties of the condensed organic solid, and form the basis of the key benefits of organic materials, such as the low-temperature processing and mechanical flexibility. The weak interactions however have implications for the optical properties and charge transport through the film. The absorption spectra of organic semiconductors are relatively narrow, and charges are often localized on a few neighboring molecules or even on a single molecule, contrary to the charge delocalization in inorganic semiconductors.

The intermolecular interactions moreover determine the crystal structure in organic thin films,[27] which can be amorphous or polycrystalline. Besides the molecular structure itself, the thin-film crystallinity and the crystal structure depend on the deposition conditions, interaction with the substrate, and post-deposition annealing treatments. The crystal structure of organic thin films is therefore hard to predict.[28] Moreover, different crystalline phases can coexist in a condensed organic solid. Information on the crystal structure is usually obtained experimentally by scanning probe microscopy or X-ray diffraction techniques.

The crystal structure defines the intermolecular orbital overlap, and consequently influences the solid-state properties of organic semiconductors. In case of asymmetric molecules, the orbital overlap furthermore differs along dissimilar crystal directions. Polycrystalline films therefore often have anisotropic optical and electrical properties, and the molecular orientation with respect to the substrate influences device performance.[14]

Planar phthalocyanine molecules are known to form two crystal structures. Both polymorphs comprise vertical stacks of Pc molecules, but mainly differ by the tilting angle between the molecular plane and the stacking axis.[10] Non-planar phthalocyanines, such as PbPc or TiOPc, disrupt this packing motif and consequently assume different crystal structures.[18,19] Thin films of SubPc-based molecules are generally assumed amorphous as a result from the non-planar molecular structure, although some reports have indicated long-range organization can occur.[29]

1.2.2 Energetics

In a conjugated molecule, the formation of π-bonds corresponds to the splitting of the electron energy levels: molecular orbitals with energies lowers than the original atomic orbitals are known as bonding π-orbitals, while orbitals with higher energies are anti-bonding π*-orbitals (**Figure 1.2**). In large conjugated systems more p_z-orbitals share their electrons, and further splitting of the individual energy levels results in quasi-continuous energy bands. The highest occupied molecular orbital (HOMO) and lowest unoccupied molecular orbital (LUMO), also known as the frontier molecular orbitals, largely determine the electronic and optical properties of the organic semiconductor. The molecular *fundamental* gap, i.e. HOMO-LUMO energy difference, generally decreases when the numbers of atoms in the conjugated system is increased, whereas the addition of electron-withdrawing (electron-donating) functional groups lowers (raises) the absolute energetic position of the frontier orbitals.

In organic thin films, the energy levels further broaden due to intermolecular interactions. In this case, the HOMO and LUMO correspond respectively to the valence and conduction band in inorganic semiconductors. However, due to disorder in organic thin films and the weak intermolecular interactions, charge carriers are localized and the energy bands are relatively narrow. The energetic position of the HOMO and LUMO levels are crucial in the operation of organic photodiodes. In the remainder of this manuscript, the energetics of organic semiconductors will therefore be characterized by the *bandgap*, i.e. the energy range of forbidden electron states between the HOMO and LUMO level. This bandgap, also known as the *transport* gap, is smaller than the molecular fundamental gap, because polarization of adjacent molecules stabilizes the ionized states.[30]

The bandgap and the energetic position of the HOMO and LUMO levels can be determined experimentally by measuring the ionization energy (IE) and electron affinity (EA) of organic thin films. A direct measurement of IE and EA is possible by ultraviolet photoelectron spectroscopy (UPS) and inverse photoemission spectroscopy (IPES). However, often the IE and EA are estimated by cyclic voltammetry measurements in solution. Conversion factors are then used to translate the redox potentials in solid-state energy levels.

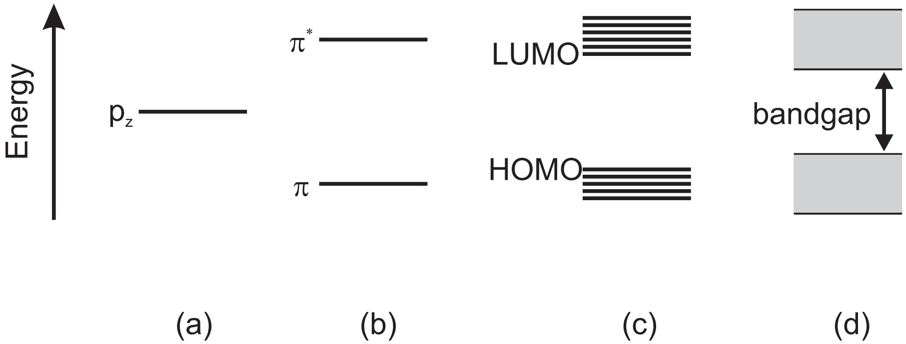

Figure 1.2: Schematic illustration of the energy level splitting of (a) atomic p_z-orbitals upon the formation of (b) molecular π-bonds. (c) The degeneracy of the molecular orbitals increases when the number of atoms in the conjugated system increases. (d) In a molecular solid the energy levels broaden and form quasi-continuous energy bands.

Common metallophthalocyanines, such as ZnPc and CuPc, have HOMO energies around -5.1 eV, and a bandgap of approximately 2.0 eV.[31,32] Thin films of the prototypical SubPc molecule have a lower HOMO energy of -5.5 eV, and a larger bandgap of 2.6 eV.

1.2.3 Optical transitions and excitons

Photon absorption in an organic semiconductor gives rise to the excitation of an electron from the HOMO to the LUMO. However, due to the charge localization and the low dielectric constant in organic semiconductors, the excited electron in the LUMO is Coulombically bound to the positively charged hole left behind in the HOMO. This bound electron-hole pair is an electrically neutral quasi-particle and is called an *exciton*. The exciton energy determines the low-energy absorption edge of an organic semiconductor. This energy, also known as the *optical* bandgap, is smaller than the transport gap, and the energy difference is the exciton binding energy.[4] The exciton binding energy typically varies from 0.2 eV to 1.5 eV in organic semiconductors,[33] significantly larger than the thermal energy at room temperature. The exciton binding energy of ZnPc, CuPc and SubPc is estimated around 0.4 eV to 0.6 eV.[32]

The electron and hole in an exciton may have parallel or anti-parallel spins, and therefore form either a singlet state with zero total spin, or a triplet state with unity total spin. Due to the reduced electronic repulsion, triplet states typically have a lower energy than singlet states. Photon absorption however results in a singlet excited state as the transition from the singlet ground state to the triplet excited state is forbidden by spin selection rules. Yet, singlet and triplet excitons can coexist in organic semiconductors under photoexcitation because singlet excitons can convert to triplets by intersystem crossing (ISC). In phthalocyanines and subphthalocyanines ISC is generally inefficient as a result of the aromatic molecular structure. The ISC rate can be increased by exploiting the strong spin-orbit coupling of heavy metal atoms, such as in platinum octaethylporphyrin (PtOEP) or tris(2-phenylpyridine) iridium(III) ($Ir(ppy)_3$).[34,35] Also fullerene C_{60} has a high ISC efficiency.[36,37] Alternatively, triplet excitons can be formed by singlet exciton fission, which occurs when the singlet exciton energy is twice the triplet energy. Rapid and efficient singlet fission has for example been observed in thin films of tetracene molecules.[38]

Relaxation of excited states in an organic semiconductor is either radiative, by emitting a photon, or non-radiative, by dissipating energy to the surroundings. The radiative decay of a photoexcited state gives rise to photoluminescence (PL), which is called fluorescence for the decay of singlet states, or phosphorescence for triplet states. Phosphorescence is typically a slower process because the decay to the singlet ground state is forbidden by spin selection rules. As a consequence, the triplet exciton lifetime can exceed the singlet lifetime by many orders of magnitude. The PL quantum yield (η_{PL}) is defined as the percentage of photogenerated excitons that decay radiatively, either by fluorescence or phosphorescence. According to Kasha's rule, PL typically occurs from the most vibrationally relaxed excited state. The PL emission is therefore red-shifted with respect to the absorption spectrum. This shift is known as the Stokes shift.

In organic thin films excitons can diffuse by hopping between neighboring molecules. This exciton diffusion gives rise to additional exciton quenching mechanisms in thin films, such as quenching at grain boundaries, impurities, interfaces, or exciton-exciton annihilation. The diffusion of excitons to organic heterojunctions is crucial for efficient operation of organic photodiodes (see next section). Hence, the exciton diffusion length (L_D), being the average distance an exciton can diffuse before it decays, is an important material parameter. For many phthalocyanines and subphthalocyanines, L_D is in the order of 5 nm to 25 nm.[14,39,40]

1.2.4 Charge transport

As a result of the weak intermolecular interactions and disorder in thin organic films, free charges – electrons or holes – are localized. A charge carrier localized on a molecule is stabilized by electronic polarization of the surrounding molecules. Furthermore, the ionized molecule undergoes vibronic relaxation. The combination of the localized charge carrier and the induced stabilization effects is known as a molecular *polaron*.[41] Under influence of an electric field or a charge carrier density gradient, these polarons can drift or diffuse to neighboring molecules. This charge transport takes place by a temperature-activated hopping process.[42] As a consequence of the charge localization, polaronic stabilization and hopping transport, the charge carrier mobility in organic semiconductors is much lower compared with inorganic semiconductors that exhibit band-like charge transport. Phthalocyanines and subphthalocyanines typically conduct holes easier than electrons. For ZnPc and CuPc hole mobilities around 10^{-3} $cm^2/(V{\cdot}s)$ have been reported.[43,44]

1.3 Organic photodiodes

An organic photodiode is an optoelectronic device that absorbs photons and converts their energy in an electric current, employing (a combination of) organic molecules or polymers in the active layer. The active layer in an organic photodiode is sandwiched between two electrodes. At least one of the electrodes is (semi-)transparent and transmits light to the active layer, while the other electrode is usually a reflecting metal contact. Typically also transparent charge transport layers are inserted between the active layer and the electrodes to improve the electrical contact. Such devices can be applied either as thin-film solar cells or photodetectors.[3] The materials used in this work as active layers, transport layers and electrodes are discussed in **Section 2.1**.

The active layer in organic photodiodes typically comprises two absorbing organic semiconductors, an electron donor and an electron acceptor. The donor material has a lower ionization energy and electron affinity (or, equivalently, higher HOMO and LUMO levels) with respect to the acceptor. This energetic offset at the donor-acceptor interface is necessary to enable efficient exciton dissociation and generation of free charge carriers in organic semiconductors. In the most basic configuration the donor-acceptor junction consists of a bilayer structure, known as a planar heterojunction (**Figure 1.3(a)**). To optimize the photocurrent generation process, alternative device structures have been developed, including bulk heterojunctions and tandem architectures. In this section, the benefits and limitations of each device architecture will become clear by taking a closer look at the individual steps of the photocurrent generation process. Next, the basic optoelectric characterization techniques are described and the requirements for efficient operation of organic solar cells and photodetectors are discussed.

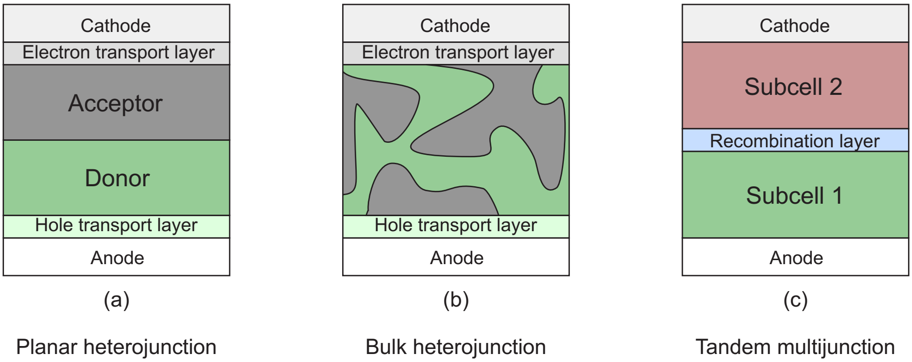

Figure 1.3: Organic photodiode device architectures.

1.3.1 Photocurrent generation

The photocurrent generation process in organic photodiodes can be considered as a sequence of four basic steps: (1) photon absorption, (2) exciton diffusion, (3) exciton dissociation, and (4) charge collection (**Figure 1.4**). Absorption of a photon in an organic semiconductor leads to the formation of an exciton, i.e. a Coulombically bound electron-hole pair. In contrast to inorganic semiconductors, the exciton binding energy in organic media exceeds the thermal energy at room temperature, and excitons do not spontaneously dissociate in free electrons and holes. Instead, excitons have to diffuse to the donor-acceptor interface, where the energetic offset between the frontier molecular orbitals enables exciton dissociation. This exciton dissociation process comprises the transfer of an electron from the donor to the acceptor, or, conversely, transfer of a hole from the acceptor to the donor. Finally, these separated charge carriers can travel to the electrodes, and an electric current is supplied to an external circuit. The efficiency of each process step is determined by the optoelectronic properties of the materials incorporated in the photodiode device structure.

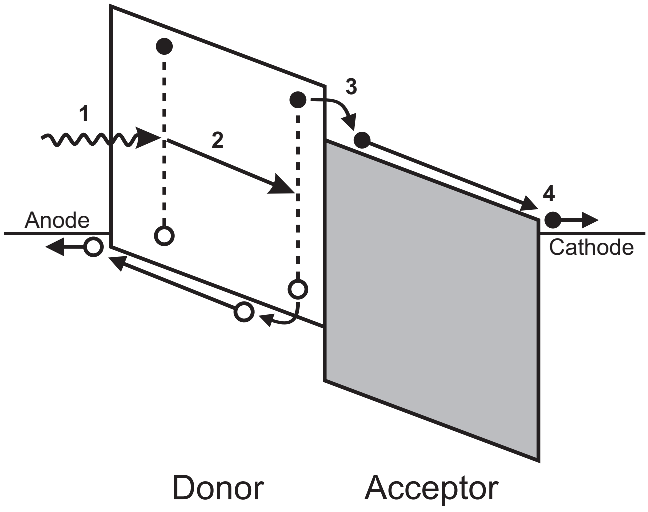

Figure 1.4: Schematic energy diagram of a bilayer organic photodiode illustrating the consecutive steps in the photocurrent generation process: **(1)** photon absorption, **(2)** exciton diffusion, **(3)** exciton dissociation, and **(4)** charge collection.

Photon absorption

The first step in the photocurrent generation process in a photodiode is the absorption of light in the active layer. Most organic semiconductors possess high absorption coefficients above 10^5 cm^{-1}. This means that 100 nm thick films suffice to absorb most of the incident light. However, the active layer thickness is often limited by the low charge carrier mobility and exciton diffusion length (see below), which results in a trade-off between light absorption and efficient charge generation and extraction. Moreover, light absorption in organic semiconductors is limited to a narrow spectral region, resulting from the lack of a continuous electronic band structure. Instead, electronic transitions in molecular solids are constrained to the specific energy levels of the molecular orbitals and vibrational modes thereof. As a result, a single donor-acceptor pair only has a narrow absorption spectrum. Because the absorption in organic solar cells ideally covers a broad range of the solar spectrum, tandem devices have been developed, in which multiple subcells with complementary absorption profiles are incorporated in a multijunction device structure (**Figure 1.3(c)**).[45–47]

Due to the thin photoactive layers, optical interference effects play an important role in organic photodiodes.[3] The optical field intensity in the active layer depends on the wavelength, layer thicknesses and the presence of a reflecting electrode. In case the optical constants of all materials are known, the absorption profile in a certain device structure can be simulated using a transfer matrix approach.[48] Knowledge of this absorption profile is important for optimization of organic photodiodes, especially in complex tandem architectures. Other factors influencing the absorption of light in the photoactive layers are the parasitic absorption and scattering of light by the electrodes and transport layers. The use of anti-reflecting coatings or light-incoupling layers can further enhance light absorption in organic photodiodes.

Exciton diffusion

Photon absorption in organic semiconductors does not directly lead to the generation of free charge carriers. Instead excitons are formed, which must first reach the donor-acceptor heterojunction in order to dissociate into free charge carriers. Because an exciton is considered as a neutral particle, exciton transport is voltage-independent, and excitons rely on diffusion to reach the heterojunction.

Excitons are assumed to be localized on a single molecules. Exciton diffusion can therefore be modeled by a random walk approximation, where each step corresponds to an exciton hopping between neighboring molecules. In this case, the exciton density $n(x)$ in an organic layer is described by a second order differential equation:

$$D\frac{\mathrm{d}^2 n(x)}{\mathrm{d}x^2} - \frac{n(x)}{\tau} + Q(x) = 0 \tag{1.1}$$

where D is the diffusivity, τ is the exciton lifetime, and x the position inside the layer. The generation rate $Q(x)$ can be determined from transfer matrix modeling of the optical field intensity.[48] By applying quenching or non-quenching boundary conditions, this equation provides the exciton density profile in a layer. The efficiency of the exciton diffusion step is then related to the exciton diffusion length ($L_D = \sqrt{D\tau}$), which is the average distance an exciton diffuses befores it decays to the ground state. This simple model does not account for energetic, spatial, and orientational disorder present in many organic films. Moreover, the presence of additional quenching mechanisms is neglected, such as exciton-polaron annihilation, exciton trapping by impurities, or exciton energy transfer to adjacent layers. Nevertheless, **equation (1.1)** can be accurate in most cases, and is suitable to analyze the exciton diffusion in organic semiconducting films.[49]

Taking a closer look at exciton transport on a molecular scale, three prevalent mechanisms can be distinguished that mediate intermolecular transfer of exciton energy, each acting on a characteristic length scale.

- Radiative energy transfer involves the emission and reabsorption of a photon between two molecules. The efficiency of this energy transfer mechanism is related to the photoluminescence quantum yield η_{PL}, the absorption coefficient α, and the Stokes shift. Moreover, it occurs over relatively long length scales, proportional to the optical penetration depth ($L_A = 1/\alpha \approx 100$ nm). In thin films of typical organic absorbers, only a small percentage of reemitted photons is absorbed; hence radiative energy transfer is usually negligible with respect to the competing energy transfer mechanisms.

- Förster energy transfer[50] is mediated by dipole-dipole coupling between two molecules, typically occurring on a length scale of 1 nm to 10 nm. The transfer rate depends on the relative dipole alignment and the overlap between the absorption and the emission spectrum. Förster energy transfer is further discussed in **Section 4.2**, where interlayer exciton energy transfer is explored to harvest excitons from an additional absorber in a multilayer cascade architecture.

- Dexter energy transfer[51] comprises the direct exchange of electrons between two neighboring molecules. This mechanism requires the overlap of molecular orbitals, and is therefore limited to length scales of 0.1 nm to 1 nm.

The efficiency of each exciton diffusion mechanism, depends on the structural and optical properties of the organic film. Moreover, singlet and triplet excitons have different diffusion characteristics. Because Förster energy transfer can only mediate energy transfer of singlet excitons due to spin conservation rules, diffusion of triplet excitons is dominated by the shorter-range Dexter transfer mechanism. Exciton diffusion lengths and exciton lifetimes can be measured by photoluminescence experiments.[39,52] The exciton diffusion length in amorphous or polycrystalline organic semiconducting films is typically in the order of 10 nm. The lifetime of singlet excitons is in the order of 1 ns, while triplet excitons have orders of magnitude longer lifetime because decay to the ground state is forbidden by spin selection rules. Despite their lower diffusivity, triplet excitons can therefore have a longer diffusion length compared with singlet excitons.

Only excitons generated within a distance of L_D from the heterojunction can eventually be dissociated. Because L_D is in many cases much shorter than L_A, the exciton diffusion step can severely limit the photocurrent generation in planar-heterojunction devices. As a consequence, many organic photodiodes employ a bulk-heterojunction structure, in which the donor and acceptor form an interpenetrating network, such that excitons are always generated within diffusion range of the donor-acceptor interface (**Figure 1.3(b)**).[53,54] Optimization of such bulk heterojunctions requires precise control of the phase segregation, which can be achieved by altering the deposition conditions or applying post-deposition annealing treatments.

Other methods to enhance the efficiency of the exciton diffusion step aim to increase the exciton diffusion length itself, which could enable the use of planar heterojunctions without compromising device performance, or alleviate the phase size constraints in bulk heterojunctions.[49] High exciton diffusion lengths can be accomplished by enhancing the crystalline ordering of the organic film,[55] diluting the absorber in a host material,[40,56] or exploiting long-lived triplet excitons by incorporating a phosphorescent sensitizer.[34,57] Furthermore, exciton quenching at the electrodes must be avoided, especially in planar-heterojunction device structures. This can be accomplished by inserting exciton-blocking layers at the contacts.[58,59] Such exciton-blocking layers should have a large bandgap with higher LUMO (lower HOMO) than the adjacent donor (acceptor) layer.

Exciton dissociation

Various reports have demonstrated that exciton dissociation at the donor-acceptor interface proceeds through an intermediate charge transfer (CT) state.[60,61] This CT state consists of an electron located on an acceptor molecule bound to a hole located on an adjacent donor molecule. The presence of this interfacial CT state has been demonstrated by electroluminescence and photoluminescence measurements,[62] as well as sensitive photocurrent measurements revealing a weak sub-bandgap excitation.[63] Furthermore, it is clear that the formation, recombination and separation of these CT states plays a crucial role in the operation of organic photodiodes. Evidently, the CT separation yield determines the photocurrent generation in a photodiode, but the CT state energy also influences the maximal voltage output, which is an important performance parameter in organic solar cells (see next section).

The CT state formation from photoexcited donor or acceptor molecules occurs very fast when the CT state energy is smaller than the initial exciton energy.[64,65] In other words, the exciton binding energy must be overcome by the charge transfer reaction, which is often described by the semi-classical Marcus theory.[66,67] Next, this CT state must be separated in free charge carriers in order for a photocurrent to flow. Although the binding energy of the CT state is typically lower than the exciton binding energy, it is still estimated ten times larger than the available thermal energy. The exact mechanisms enabling efficient CT state separation are still under debate, and extensive reviews on charge transfer processes are available in the literature.[60,61]

This CT separation process competes with several recombination mechanisms (**Figure 1.5**). Most importantly, the CT state can recombine through radiative or non-radiative transitions to the ground state. If the CT state originated from a single exciton this process is called geminate recombination. The CT separation is however a reversible process. This means that free electrons and holes can form a CT state when they meet at the donor-acceptor interface. If this CT state subsequently recombines this process is known as non-geminate recombination, since the free charge carriers were originally generated independently. An additional recombination mechanism is back transfer from the CT state, which results in the formation of a singlet or triplet exciton on the donor or acceptor. The CT separation yield depends on the relative rate constants for these different reactions.

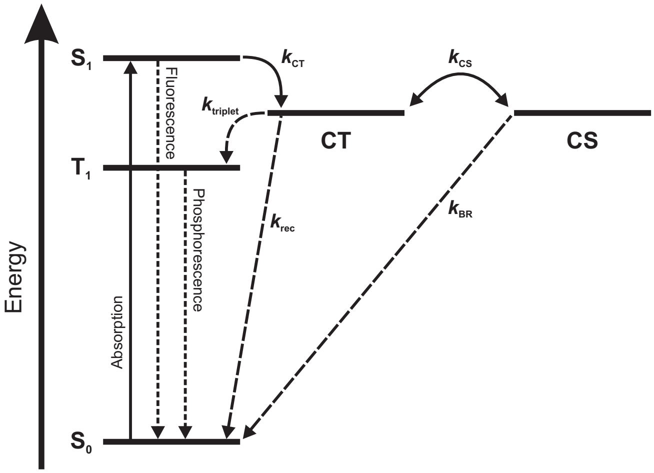

Figure 1.5: Simplified representation of the energetic states that play a role in the exciton dissociation process. Optical excitation of the ground state (S_0) result in the formation of a singlet exciton (S_1), which can undergo charge transfer (k_{CT}) to the CT state. This CT state can either be separated (k_{CS}) in free charge carriers, recombine (radiatively or non-radiatively) to the ground state (k_{rec}), or undergo back transfer ($k_{triplet}$) to the triplet exciton (T_1). Furthermore, the charge separated state (CS) is prone to bimolecular recombination of free charge carriers (k_{BR}).[60]

A commonly used approach to describe CT state separation is based on the Onsager-Braun theory,[68] which relates the charge separation rate to macroscopic parameters such as the charge mobility, dielectric constant and the internal electric field. The separation efficiency depends on the distance between the charge pair in the CT state, also known as the thermalization length. This model is however a basic approximation, and does not account for other factors that might influence the CT separation yield, such as energetic disorder, excess kinetic energy, charge delocalization, and the entropy contribution to the free energy.[60,61]

As will become clear in the next section, the CT state energy is related to the open-circuit voltage of an organic photodiode. As the efficiency of organic solar cells is determined by both photocurrent and photovoltage, it is important to keep the energy losses related to the charge transfer processes to a minimum, without limiting the charge transfer efficiency.

Charge collection

The final step in the photocurrent generation process is the collection of electrons and holes at their respective electrodes. Transport of the charge carriers through organic layers is governed by drift and diffusion, and the charge carrier mobility and lifetime are the main parameters determining the charge collection efficiency. The mobility mainly depends on the crystallinity of the organic material. In highly crystalline layers, charge transport can be described by bandlike transport, similar to inorganic semiconductors. However, as a consequence of the molecular disorder and charge localization in most organic materials, charge carriers are usually transported by a hopping mechanism, and low charge carrier mobilities of 10^{-5} cm^2/(V·s) to 0.1 cm^2/(V·s) are typically observed.[4] Many different models for charge transport have been proposed, emphasizing the dependence of charge carrier mobilities on temperature, electric field, and charge carrier density.[42,69,70] If drift is the dominant transport mechanism, the mobility is directly related to the transit time of the charge carriers to the electrodes. This transit time must be smaller than the charge carrier lifetime to obtain a high charge collection efficiency. The carrier lifetime can however be significantly reduced by charge traps due to structural and morphological defects, grain boundaries, and impurities. In bulk heterojunctions free charge carriers are also prone to bimolecular recombination at the donor-acceptor interface. Furthermore, a too close intermixing in the blend can create isolated donor or acceptor phases from which the charge carriers cannot escape.

An additional issue regarding charge collection in organic photodiodes is the existence of energy barriers at the interface of the active layer and the electrodes. Extraction barriers can block charge collection at the contacts, but also injection barriers have been shown inhibit charge extraction in planar-heterojunction devices by causing inversion of the electric field in the active layers.[71] For this reason, charge transport layers are commonly used to form an ohmic contact with the electrode. Ideally, these transport layers are transparent to visible light and selective for one type of carriers, especially in bulk-heterojunction devices. Hence, large-bandgap materials are typically used. Often the conductivity of these transport layers is increased by doping them with low concentrations of small molecules, metals or metal oxides.[72] Such doped transport layers induce negligible ohmic losses, even when the layer thickness exceeds 100 nm, and consequently don't impede the charge collection. Moreover, they can be used as optical spacer layer to adjust the interference pattern in the device stack and increase absorption in the active layers.

1.3.2 Characterization

The performance of an organic photodiode is evaluated by measuring the current output as function of the externally applied voltage. This measurement can be done in dark or under illumination (usually the standard AM1.5G solar spectrum in case of organic solar cells). Knowing the active area of the device, the current density-voltage (*J*-*V*) curve is obtained. Due to the asymmetric device structure the *J*-*V* curve follows a diode behavior, which can be modeled by the ideal diode equation:[73]

$$J = J_0 \cdot \left[\exp\left(\frac{qV}{kT}\right) - 1\right] - J_{\text{photo}}(V) \tag{1.2}$$

with q the elementary charge, k the Boltzmann constant, and T the temperature. For organic heterojunctions the saturation current density J_0 is related to the energetics and recombination kinetics at the donor-acceptor interface. As a consequence, J_0 in this expression is not constant but depends on the applied voltage and the charge carriers density.[74] The photocurrent density J_{photo} is proportional to the incident light intensity and the yield of the photocurrent generation process described above. The photocurrent is consequently also voltage-dependent. At zero applied voltage, J_{photo} yields the short-circuit current density: $J_{\text{SC}} = J(V = 0) = J_{\text{photo}}(V = 0)$.

Often the photocurrent generation is also evaluated by measuring the spectral photocurrent response. From this measurement the external quantum efficiency (EQE) can be calculated as the ratio of the amount of collected electrons and the amount of *incident* photons at a certain wavelength. When the EQE is measured at zero applied voltage, J_{SC} is obtained by integrating the EQE over the incident light spectrum

$$J_{\text{SC}} = q \int \text{EQE}(\lambda) \cdot \phi(\lambda)\, \text{d}\lambda \tag{1.3}$$

where $\phi(\lambda)$ is the spectral photon flux, and λ indicates the photon wavelength. The EQE itself depends on the yield of the entire photocurrent generation process. The internal quantum efficiency (IQE), on the other hand, is defined as the ratio of the amount of collected electrons and the amount of *absorbed* photons. The IQE is calculated as the ratio of the EQE and the absorptance A, $\text{IQE}(\lambda) = \text{EQE}(\lambda)/A(\lambda)$, and is determined by the efficiency of exciton diffusion, charge transfer and charge collection.

The open-circuit voltage (V_{OC}) is the voltage at which no current flows through the illuminated photodiode. By reformulating **equation (1.2)** it becomes clear that the V_{OC} is determined by the balance between the photocurrent and the recombination current:

$$V_{\text{OC}} = \frac{kT}{q} \cdot \ln\left(\frac{J_{\text{photo}}}{J_0} + 1\right) \tag{1.4}$$

Here J_{photo} and J_0 should be evaluated at open-circuit conditions. However, assuming the spectral shape of the EQE does not depend on voltage, Rau's reciprocity relation suggest that the J_{photo}/J_0 ratio can also be evaluated at short-circuit conditions.[75,76] Further assuming that the dark current is dominated by CT state recombination, and that the CT state absorption and emission can be modeled by Marcus theory, the following expression for V_{OC} is obtained:[77]

$$V_{\text{OC}} = \frac{E_{\text{CT}}}{q} + \frac{kT}{q} \cdot \ln\left(\frac{J_{\text{SC}} \cdot h^3 \cdot c^2}{2\pi \cdot f \cdot q \cdot (E_{\text{CT}} - \lambda)}\right) + \frac{kT}{q} \cdot \ln(\text{EQE}_{\text{EL}}) \tag{1.5}$$

where E_{CT} is the CT state energy, λ the molecular reorganization energy, h the Planck constant, c the speed of light, EQE_{EL} the integrated electroluminescence quantum efficiency, and f a factor related to the photovoltaic quantum yield and electronic coupling between the ground state and the CT states.

Equation (1.5) successfully describes the dependence of V_{OC} on temperature and light intensity observed in the literature.[78,79] Furthermore, this expression indicates the CT state energy as the maximum limit for $q \cdot V_{\text{OC}}$. As a consequence of detailed balance between absorption and emission, however, the maximal V_{OC} cannot be achieved due to radiative recombination of CT states. This minimal voltage loss is described by the second term in **equation (1.5)**. The last term in this expression represents the voltage loss due to non-radiative recombination.

Due to the presence of series and shunt resistances the J-V curves deviate from the ideal shape expected from **equation (1.2)**. The series resistance of an organic photodiode is related to the charge collection process, and depends on materials parameters such as the mobility of the active layers, the presence of extraction barriers, and the resistance of the electrodes. The shunt resistance, on the other hand, results from a leakage current through the device, which can be caused by pinholes, recombination at trap states, or edge effects. Considering the equivalent circuit of an organic photodiode **(Figure 1.6)**, including series (R_S) and shunt resistances (R_P), the generalized diode equation is given by:[4]

$$J = \frac{R_P}{R_S+R_P} \cdot \left\{ J_{0,n} \cdot \left[\exp\left(\frac{q\cdot(V-JR_S)}{nkT}\right) - 1 \right] + \frac{V}{R_P} - J_{\mathrm{photo}}(V) \right\} \tag{1.6}$$

The ideality factor n accounts for the dependence of the saturation current density on voltage and charge carrier density. Consequently, $J_{0,n}$ can be considered as a constant, in contrast to J_0 in **equation (1.2)**. Experimental values for R_S, R_P, n, and $J_{0,n}$ can be obtained by fitting measured J-V curves with **equation (1.6)**.

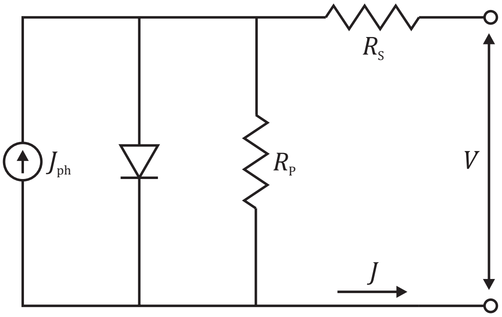

Figure 1.6: Equivalent circuit of an organic photodiode, including series (R_S) and shunt (R_P) resistances.

1.3.3 Applications

Two major applications of organic photodiodes will be studied in this work, organic solar cells and organic photodetectors. Although both applications use similar device structures, different operating conditions are applied, and therefore different materials properties are required for optimal performance.

Solar cells

The purpose of (organic) solar cells is to convert the energy of light in electrical energy. Under illumination, a photodiode generates power for applied voltages between zero and V_{OC}. In this range the output power is maximized for a certain applied voltage $V_{\max}$

and current density J_{max} (**Figure 1.7**). This condition is known as the maximum power point, where the solar cell produces a power density $P_{\mathrm{max}} = V_{\mathrm{max}} \times J_{\mathrm{max}}$. The power conversion efficiency (PCE) of a solar cell is defined as the ratio of this maximal power output and the power supplied by the incident light:

$$\mathrm{PCE} = \frac{P_{\mathrm{max}}}{P_{\mathrm{in}}} = \frac{J_{\mathrm{SC}} \cdot V_{\mathrm{OC}} \cdot \mathrm{FF}}{P_{\mathrm{in}}} \tag{1.7}$$

The incident light intensity P_{in} is given by

$$P_{\mathrm{in}} = \int \frac{hc}{\lambda} \cdot \phi(\lambda)\, \mathrm{d}\lambda \tag{1.8}$$

where $\phi(\lambda)$ is the spectral photon flux of the illumination source. Usually, solar cells are characterized under the standard AM1.5G solar spectrum with an intensity of 100 mW/cm^2, which corresponds to the typical solar irradiance on Earth's surface (**Figure 1.8**). However, as organic solar cells can be applied as indoor light harvesters, illumination sources with different spectra and intensities can be used to evaluate the performance under non-standard lighting conditions (see **Section 4.3.1**).

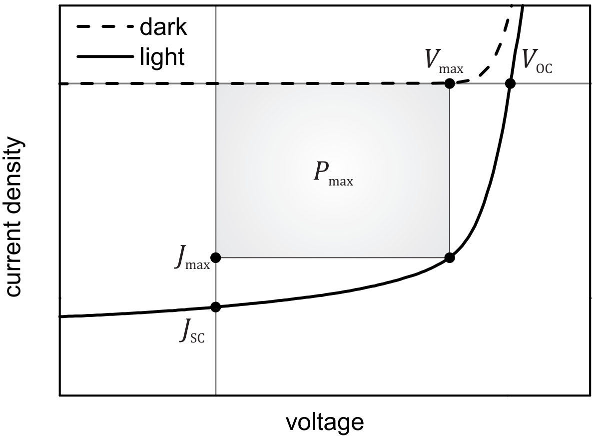

Figure 1.7: Typical current density-voltage curve of an organic solar cell, indicating the voltage (V_{max}) and current density (J_{max}) at maximum power point, the open-circuit voltage (V_{OC}), and the short-circuit current density (J_{SC}).

In **equation (1.7)**, the fill factor (FF) is defined as

$$\mathrm{FF} = \frac{J_{\mathrm{max}} \cdot V_{\mathrm{max}}}{J_{\mathrm{SC}} \cdot V_{\mathrm{OC}}} \tag{1.9}$$

The FF in organic solar cells is largely determined by the balance between charge extraction and recombination. The transport of free charge carriers to the electrodes, reflected by the series and shunt resistance of the cell, depends on material properties such as the charge carrier mobility, the presence of energy barriers, and the probability for bimolecular recombination.[44,71,80] In addition, the FF is determined by the voltage dependence of the photocurrent in the fourth quadrant of the J-V graph. When the photocurrent slope is large, and the dark current is not yet significant, an 'S-kink' can be observed in the J-V curve under illumination. Such voltage-dependent photocurrents can occur because the CT dissociation and recombination rates depend on the internal electric field.[74] Changing the configuration of the active layer and transport layers can alter the built-in field in the device, and consequently influence the CT dissociation yield. Because geminate recombination is expected to depend only on the electric field, while bimolecular recombination also depends on the charge carrier density, the different processes influencing the FF can be distinguished by looking at the effect of illumination intensity on the J-V curves.

Driven by the report of Tang in 1986,[81] introducing the donor-acceptor interface to enable efficient exciton dissociation, the PCE of organic photovoltaic (OPV) devices has increased rapidly during the last decades. This progress resulted from many adaptations to the original bilayer OPV device structure, including the design of new molecules and polymers, introduction of bulk heterojunctions, control of the active layer morphology, and the introduction of charge-selective transport layers. However, as consequence of the multistep photoconversion process, a delicate balance exists between the J_{SC}, V_{OC} and FF of organic solar cells. Therefore, a deliberate selection of material combinations and device architectures is crucial to optimize the PCE. For example, the J_{SC} is often limited by the small spectral overlap between the absorption in the active layer and the solar spectrum (**Figure 1.8**). Employing small-bandgap absorbers therefore improves J_{SC} as more infrared light can be harvested.[82] However, the use of such small-bandgap materials limits the maximum V_{OC} of the device.[83] Likewise, bulk heterojunctions (**Figure 1.3(b)**) are often used to circumvent restrictions related to the small exciton diffusion length in many organic semiconductors. Despite the improved charge generation, the intermixing of donor and acceptor phases can hinder charge extraction and enhance bimolecular recombination, possibly decreasing the FF and V_{OC} in such device architectures.

Currently, state-of-the-art OPV devices reach PCE values up to 12%, measured under 100 mW/cm^2 AM1.5G illumination.[84,85] The best performing devices employ a tandem architecture, in which multiple complementary absorbing subcells are stacked on top of each other and connected in series by a charge recombination layer (**Figure 1.3(c)**).[86,87] Besides the broadened absorption spectrum, tandem devices obtain high V_{OC} values because the serial connection adds up the voltages of the individual subcells. For single junction OPV cells efficiencies up to 10% have been reported, using either polymers or small molecules as the active materials.[88–90] Even though OPV performance has rapidly increased in the last few years, the thermodynamic efficiency limit has not yet been achieved and the PCE of OPV devices can be further enhanced.

As the IQE of the best performing OPV devices already approaches 100%,[91,92] further PCE improvements are expected by enhancing the absorption in the active layer, and consequently increasing the EQE, or by increasing the operating voltage without sacrificing efficient photocurrent generation.

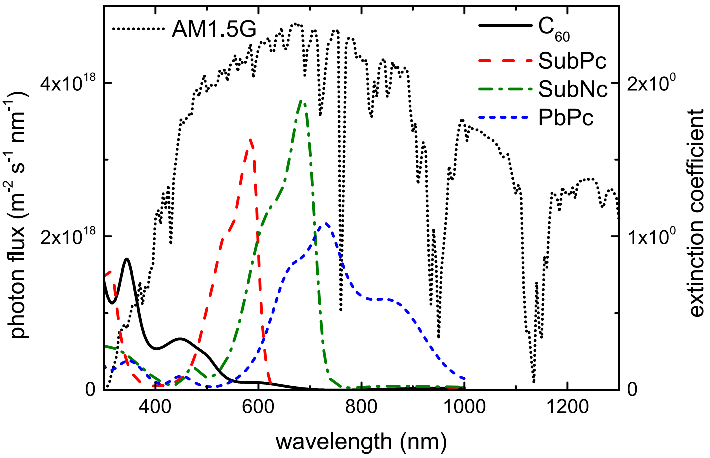

Figure 1.8: The standard AM1.5G solar spectrum compared with the absorption range of some small-molecule organic absorbers used in this work.

The absorption efficiency can evidently be improved by introducing highly absorptive materials in the active layer. The high absorption coefficients of many phthalocyanines explains their widespread use as donor in vacuum-evaporated organic solar cells. In **Chapter 3**, also the fullerene acceptors will be replaced by highly absorptive subphthalocyanines. In addition, the absorption spectrum can be broadened by combining multiple complementary absorbers, as is usually realized with tandem device structures.[46,93,94] In **Chapter 4**, multilayer cascade architectures are presented as alternative to tandem devices. Such cascade devices either enable charge generation at multiple active heterojunctions, or exploit long-range interlayer exciton energy transfer.

In organic solar cells V_{OC} is experimentally observed to increase linearly with the interface energy gap E_{DA}, being the energy difference between the HOMO level of the donor and the LUMO level of the acceptor.[65,95,96] This observation can be explained by **equation (1.5)** and the fact that E_{CT} can be roughly approximated by E_{DA}, neglecting the CT state binding energy, molecular reorganization and interface dipole effects. Besides interface energetics, **equation (1.5)** also reveals that V_{OC} is related to radiative and non-radiative recombination of free charge carriers. The non-radiative voltage loss can be avoided if EQE_{EL} equals unity. The V_{OC} then reaches its radiative limit. However, in many organic photodiodes the EQE_{EL} is below 10^{-6}.[77] The non-radiative recombination of free charge carriers consequently causes an important voltage loss in organic solar cells. Also the radiative voltage loss can be diminished, for example by reducing the electronic coupling at the donor-acceptor interface,[97] or reducing the density of CT recombination sites.[98] Reduction of the exciton dissociation efficiency is however a main concern when such alterations are applied to the donor-acceptor interface. **Chapter 3** will reveal that, besides increased photocurrent generation, the use of non-fullerene acceptors also results in enhanced V_{OC} values.

Photodetectors

In contrast to solar cells, the target of photodetectors is to produce a photocurrent signal, instead of delivering a photoinduced power to an external load. As a consequence, organic photodiodes operate as photodetectors by applying a reverse voltage bias, which improves charge carrier generation and collection. Hence, the J-V parameters V_{OC} and FF are less relevant in the performance evaluation of an organic photodetector (OPD). Instead, the EQE (at reverse bias) and responsivity ($R = J_{\mathrm{photo}}/P_{\mathrm{in}}$) are the main figures of merit. In addition, the photodetector should be optimized for maximal sensitivity, which is quantified by the Noise Equivalent Power (NEP). The NEP of an OPD device corresponds to the minimum optical power that can be distinguished from the electronic noise. The inverse of NEP, normalized for the active area of the device (A) and the frequency bandwidth (Δf), yields the specific detectivity D^*:

$$D^* = \frac{\sqrt{A \cdot \Delta f}}{\mathrm{NEP}} = \frac{R\sqrt{A \cdot \Delta f}}{i_{\mathrm{n}}} \tag{1.10}$$

where the noise current i_{n} consists of thermal noise, flicker noise and shot noise from the dark current. It is often assumed that the latter forms the dominant contribution to the electronic noise at reverse bias.[99, 100] In this case D^* is expressed by:

$$D^* \approx \frac{R}{\sqrt{2q \cdot J_{\mathrm{dark}}}} \tag{1.11}$$

where J_{dark} is the current density flowing through the device in absence of illumination. The performance of OPD devices is thus determined by both the responsivity under illumination as well as the dark current density.

Depending on the final application, the EQE should either cover a broad spectral range, or, in contrast, have a wavelength selective response. For example, a broadband (panchromatic) response is needed for remote sensing applications,[101] while a narrowband (wavelength selective) response is required for industrial quality control or biological imaging.[102,103] Such spectral sensitivity can be achieved by selecting the appropriate absorbing materials in the active layer of the OPD. In **Chapter 5** the use of Pb phthalocyanine (PbPc) yields photocurrent generation at near-infrared (NIR) wavelengths.

The dark current in OPD devices can originate from many different mechanisms, including thermal generation of free charge carriers in the bulk or at the donor-acceptor interface, charge injections from the electrodes, and electric shunt paths through the device. Hence, hole or electron blocking layers are often introduced to prevent leakage current from charge injection or shunts. Such blocking layers should only transport one type of charge carriers to the electrode, and are ideally highly conductive and transparent. The origin of dark current in PbPc-based OPDs will be further investigated in **Chapter 5**, with the goal to improve the detectivity of such NIR sensitive OPDs.

Another performance parameter of photodetectors is the frequency bandwidth, which is related to the reciprocal of the carrier transit time. Furthermore, the OPD device integration completely differs from OPV: whereas solar power generation requires the development of large-area modules, small-area pixels are needed for imaging applications of photodetectors. Although these device characteristics are crucial for the final applications of OPDs, they are not addressed in this work as they are beyond the scope of this research.

1.4 Thesis objectives and outline

In this dissertation phthalocyanines and subphthalocyanines will be employed as active materials in organic photodiode device structures. By exploiting the unique properties of these organic semiconducting molecules, this work aims to enhance the performance of organic solar cells and organic photodetectors. Study of the material properties and device physics will provide guidelines for deliberate modifications of the device structure.

This introductory chapter explored the basic material and device properties involved in the operation of organic photodiodes. In case of organic solar cells, (sub)phthalocyanines can improve the power conversion efficiency by exploiting the strong absorption of visible and near-infrared light. In addition, the chemical versatility of these molecules enables the optimization of heterojunction energetics. For photodetectors, the selective spectral response of phthalocyanines unfolds a wide range of innovative applications.

Chapter 2 assembles all information on the materials, device processing and characterization techniques used in this work.

Chapter 3 describes the development of organic solar cells with non-fullerene acceptors. Replacement of the traditional fullerene acceptors in organic solar cells by subphthalocyanine acceptors enhances the absorption of visible light. Energy level tuning of SubPc derivatives moreover enables the systematic study and optimization of donor-acceptor heterojunction energetics. The simultaneous enhancement of open-circuit voltage and short-circuit current results in fullerene-free OPV devices with power conversion efficiencies exceeding their fullerene-based counterparts.

The unique optoelectronic properties of subphthalocyanines furthermore enable the development of multilayer OPV cascade architectures, which will be explored in **Chapter 4**. First, SubPc is used as an ambipolar interlayer in a three-layer charge transfer cascade device. Here, photocurrent is generated simultaneously at two discrete heterojunctions. Next, energy transfer cascade devices are investigated, in which long-range exciton energy transfer is exploited to harvest excitons from multiple absorbers. Finally, the best performing cascade architecture is evaluated for application-relevant conditions, such as semi-transparency and indoor operation.

In **Chapter 5** a non-planar phthalocyanine, PbPc, is employed in organic photodetectors. Near-infrared sensitivity is obtained by templating the crystal growth of this material. Successful application as OPD however requires a reduction of the dark current density. Hence, the origin of the dark current in PbPc-based OPDs will be investigated.

Finally, in **Chapter 6** the main conclusions of this work will be summarized, together with the possible perspectives for future research.

2. Materials and experimental methods

This chapter collects all information about the materials and experimental methods used in this work. **Section 2.1** first discusses the materials used to fabricate organic photodiodes. Next, the sample fabrication procedure is defined in **Section 2.2**. Finally, **Section 2.3** describes the experimental techniques used to characterize organic thin films and devices.

2.1 Materials

Organic semiconducting molecules exist in an innumerable amount of flavors, resulting from the endless variations that can be introduced by substitutions and changes to the molecular structure. The previous chapter already presented the class of phthalocyanines and subphthalocyanines, which will be used in the active layer of the organic solar cells and photodetectors developed in this work. Besides Pc- and SubPc-based molecules, other types of molecules will be used as donor, acceptor, or transport layer. This section gives an overview of all materials used in this work, grouped by their function in the photodiode device structure. **Table 2.1** moreover summarizes some key properties of the organic small molecules. Also the inorganic semiconductors and thin metal films, used as transport layers and electrodes, are discussed here.

2.1.1 Anode

The anode of the photodiodes described in this work consists of a thin film of indium tin oxide (ITO). Due to its high bandgap (4 eV), ITO is mostly transparent for visible light.[104] The workfunction of ITO varies from 4.4 eV to 4.7 eV, depending on the preceding surface treatment.[105] The ITO film is deposited on glass substrates, with a thickness of 140 nm and a RMS surface roughness around 1 nm. The conductivity of these ITO films is approximately 2.5×10^5 S/m. Patterning of the ITO film forms two parallel lines on the glass substrate. The overlap of these lines with the metal top contact defines the active area of the photodiode.

2.1.2 Hole transport

Hole transport layers (HTL) are often used in organic photodiodes to enhance hole extraction to the ITO anode. Ideally, the materials used as HTL are also optically transparent, and block exciton quenching and electron injection.

Polymers

A commonly used HTL is poly(3,4-ethylenedioxythiophene)-poly(styrenesulfonate) (PEDOT:PSS), which is a mixture of ionized polymers. This mixture is generally available as an aqueous dispersion, and can be applied to the ITO anode by spin-coating. The 5.1 eV workfunction of PEDOT:PSS corresponds to the HOMO level of many donor materials, explaining the widespread use of PEDOT:PSS as HTL. Thin films of PEDOT:PSS are however extremely hygroscopic, and can cause performance degradation of organic photodiodes when they are used in humid environments.[106] Alternatively, poly[N,N'-bis(4-butylphenyl)-N,N'-bis(phenyl)benzidine] (poly-TPD) and poly(triarylamine) (PTAA) can be used as HTL. These polymers have high LUMO levels of -2.3 eV and -1.8 eV, respectively,[107,108] and therefore form hole-selective contacts with most donor materials.

Inorganic semiconductors

Although molybdenum tri-oxide (MoO_3) is often employed as HTL, this transparent oxide is actually a *n*-type semiconductor.[109] Due to its high workfunction (6.9 eV), electrons from an adjacent organic layer transfer to the MoO_3 conduction band (-6.7 eV). This thermodynamic equilibration of the electron chemical potential results in an upward band bending of the organic energy levels. The photogenerated holes in an organic photodiode are then extracted by recombination with electrons in the MoO_3 conduction band. Thin films of MoO_3 are deposited on the substrate by vacuum evaporation, with an evaporation temperature around 550 ˚C. Even though the composition may be slightly non-stoichiometric after evaporation, this compound will be denoted as MoO_3, as also frequently appears in the literature.

Copper iodide (CuI) is an inorganic *p*-type semiconductor with a large bandgap (3.1 eV) and high transmittance of visible and near-infrared wavelengths. The workfunction of CuI is estimated at 5.4 eV to 5.8 eV.[110,111] As a result of this high workfunction strong interface dipoles are induced in the adjacent organic layers. Insertion of a thin CuI layer at the ITO anode has been shown to alter the molecular orientation in CuPc and ZnPc thin films.[14,112] In **Chapter 5** CuI is used to template the growth of a PbPc layer. Thin films of CuI are deposited on the substrate by vacuum evaporation, with an evaporation temperature around 300 ˚C.

Organic small molecules

Also the following wide-bandgap organic small-molecule semiconductors will be employed as HTL in this work:

- 4,4'-bis(N-carbazolyl)-1,1'-biphenyl (CBP),
- diindenoperylene (DIP),
- N,N'-di(1-naphthyl)-N,N'-diphenyl-(1,1'-biphenyl)-4,4'-diamine (NPB),
- and tris[4-(5-phenylthiophen-2-yl)phenyl]amine (TPTPA).

These materials are evaporated in a vacuum chamber at temperatures between 200 ˚C and 300 ˚C. Efficient hole extraction through these HTLs requires alignment of the HOMO energy level with the adjacent donor layer. Due to their large optical bandgap, these molecules are mostly transparent to visible light. In addition, these molecules function as exciton-blocking layers, in contrast to PEDOT:PSS and MoO_3.

2.1.3 Donor

The donor materials used in this work are mostly phthalocyanines, such as ZnPc and PbPc, or subphthalocyanines, such as SubPc and SubNc. Their molecular an solid-state properties were already discussed in **Chapter 1**, and their molecular structure will be illustrated in the appropriate sections of this thesis. In **Chapter 3** and **Chapter 4**, SubPc and SubNc are used as non-fullerene acceptors, requiring donor materials with higher HOMO and LUMO energy levels to enable exciton dissociation at the donor-acceptor interface. In this case, tetracene (Tc) and α-sexithiophene (α-6T) are used as donor, which form polycrystalline thin films with high hole mobility. Compared with phthalocyanine donors, these molecules have a lower evaporation temperature. The solid-state properties of these materials are further discussed in **Section 3.3**.

2.1.4 Acceptor

The most common acceptor material in small-molecule organic photodiodes are the fullerenes C_{60} and C_{70}. **Chapter 3** will however focus on the use of non-fullerene acceptors in organic solar cells. The advantages and disadvantages of various acceptor materials will therefore be further discussed in **Section 3.1**. Besides SubPc and SubNc, four SubPc derivatives will be tested as electron acceptor. These molecules have absorption spectra similar to SubPc, but their peripheral substituents lower the frontier orbital energy levels. Although the addition of substituents increases the evaporation temperature, the SubPc derivatives can be deposited at significantly lower temperatures compared with fullerenes.

2.1.5 Electron transport

Bathocuproine (BCP) will be used as the standard electron transport layer (ETL) in this work. The high bandgap of BCP yields the desired optical transparency and exciton-blocking properties. The insertion of a BCP layer has also been suggested to act as a passivating layer, protecting the active layer during deposition of the metal cathode.[58] The poor conductivity of BCP ($\approx 10^{-9}$ S/m) however limits the series resistance when the layer thickness exceeds 10 nm.[58,113] To increase the conductivity, a doped ETL can be deposited by co-evaporating BCP and a low-workfunction metal such as Yb.[72] Typically low doping concentrations of 5% are used. Alternatively, a 1:1 BCP:C_{60} blend can be used as a transparent, exciton-blocking ETL.[114] Due to the high electron conductivity of these co-evaporated layers ($\approx 10^{-5}$ S/m) the ETL thickness can exceed 10 nm, enabling optimization of the optical interference profile in the active layers of the device. Besides BCP, other small molecules can be used in the ETL. For example, 1,4,5,8-napthalene-tetracarboxylic-dianhydride (NTCDA) is employed in **Chapter 5** as a hole-blocking, electron-transporting layer. Both BCP and NTCDA can be evaporated in a vacuum chamber at relatively low temperatures below 200 ˚C.

2.1.6 Cathode

The top contact of the devices studied in this work generally consists of a 120 nm thick Ag film. Alternatively, Al can be used, decreasing the workfunction of the metal cathode from 4.5 eV for Ag to 4.2 eV for Al. Due to its lower workfunction, Al is more suited for devices with a high V_{OC}. Thim films of both metals are deposited by vacuum evaporation.

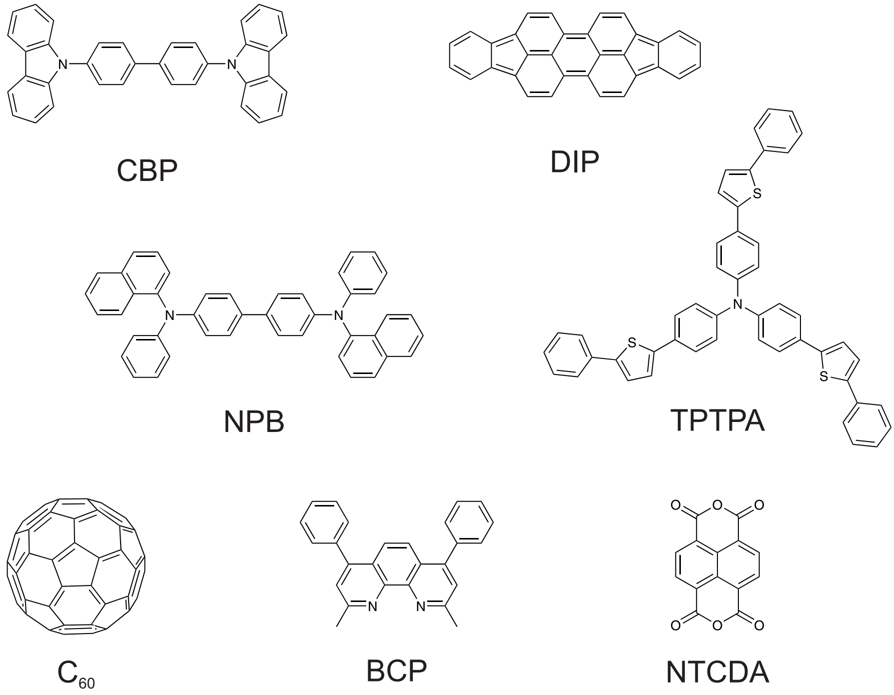

Figure 2.1: Molecular structure of small-molecule hole transport materials (CBP, DIP, NPB, and TPTPTA), acceptors (C_{60}), and electron transport materials (BCP and NTCDA).

ACKNOWLEDGEMENT
The HOMO and LUMO levels of SubPc and SubNc, measured by UPS and IPES, were kindly provided by Barry Rand and Antoine Kahn from Princeton University.

Table 2.1: Overview of the small-molecule organic semiconductors used in this work, summarizing their function in the organic photodiode device structure, frontier molecular orbital energies, and evaporation temperature in the vacuum deposition chamber.

	Function	HOMO (eV)	LUMO (eV)	Evaporation temperature (°C) [c]	Molecular structure
CBP [32]	*Hole transport*	-6.1	-1.9	170 - 200	**Figure 2.1**
DIP [95]	*Hole transport*	-5.35	-2.8	220 - 240	**Figure 2.1**
NPB [32]	*Hole transport*	-5.3	-1.5	190 - 220	**Figure 2.1**
TPTPA [115]	*Hole transport*	-5.25	> -2.75	250 - 290	**Figure 2.1**
α-6T [31,32]	*Donor*	-5.0	-2.5	190 - 230	**Figure 3.7**
Tc [32]	*Donor*	-5.1	-1.8	120 - 150	**Figure 3.7**
PbPc [116,a]	*Donor*	-5.2 (monoclinic) -5.0 (triclinic)	-3.3	290 - 330	**Figure 3.1**
ZnPc [47]	*Donor*	-5.11	-3.2	330 - 380	**Figure 3.1**
F_4-ZnPc [47,a]	*Donor*	-5.46	-3.55	330 - 380	**Figure 3.1**
SubNc [115]	*Donor, Acceptor*	-5.37	-3.1	300 - 340	**Figure 3.1**
SubPc [115]	*Donor, Acceptor*	-5.5	-2.9	200 - 230	**Figure 1.1**
Cl_4-SubPc-Cl [b]	*Acceptor*	-6.14	-3.54	200 - 260	**Figure 3.1**
Cl_6-SubPc-Cl [b]	*Acceptor*	-6.21	-3.61	210 - 300	**Figure 3.1**
$(CN)_3$-SubPc-F [b]	*Acceptor*	-6.31	-3.71	200 - 270	**Figure 3.1**
F_{12}-SubPc-Cl [b]	*Acceptor*	-6.45	-3.85	150 - 190	**Figure 3.1**
C_{60} [32,95]	*Acceptor*	-6.3	-3.9	350 - 420	**Figure 2.1**
C_{70} [117]	*Acceptor*	-6.2	-3.9	380 - 460	
BCP [32]	*Electron transport*	-6.5	-1.6	140 - 170	**Figure 2.1**
NTCDA [118]	*Electron transport*	-8.0	-4.0	150 - 180	**Figure 2.1**

[a] The LUMO level is estimated by assuming a transport gap similar to ZnPc.

[b] The LUMO level is determined from cyclic voltammetry measurements in solution. See **Appendix**. The HOMO levels is estimated by assuming a transport gap similar to SubPc.

[c] Temperature range for typical evaporation conditions of pressure below 2 x 10^{-6} Torr and deposition rate around 1 Å/s.

2.2 Sample fabrication

OPV devices were fabricated on prepatterned ITO-coated glass substrates. Complementary characterization of organic thin films required the use of glass, quartz, or Si/SiO_2 substrates. The latter consists of a Si wafer, with a thermally grown SiO_2 layer of 120 nm to 140 nm.

All substrates were cleaned by sequential sonication in detergent, deionized water, acetone and isopropanol, followed by a 5-minute oxygen-plasma treatment to remove the remaining carbon residue.

Spin-coating of PEDOT:PSS in air was followed by a bake-out at 130 °C in N_2, resulting in a layer thickness of approximately 25 nm. Thin films of poly-TPD and PTAA were spin-coated from a 5-mg/mL chloroform solution in a N_2 environment.

Deposition of the metal cathode, MoO_3, CuI, and all small organic molecules was done by thermal evaporation in a high vacuum chamber at pressure below 2×10^{-6} Torr. All organic materials were purified by thermal gradient sublimation before being loaded into the evaporation crucible. The layer thickness and deposition rate are monitored by a quartz crystal microbalance, calibrated by optical thickness measurements using spectroscopic ellipsometry. Unless stated otherwise, a deposition rate of 1 Å/s was used, including the co-evaporated layers. The Al or Ag cathode is evaporated at 1.5 Å/s through a shadow mask, defining an active area of 13.4 mm^2.

For testing under ambient atmosphere, samples were encapsulated by sealing the active area with a glass lid and epoxy adhesive to avoid degradation. The adhesive was cured by exposing the sample to UV illumination for 1 minute. After curing, the samples were kept in a N_2 environment for at least 24 hours before exposing them to ambient environment.

2.3 Characterization techniques

This section provides experimental details of the most important characterization techniques used in this work. Additional techniques used to characterize specific properties of molecules, thin films or devices are described in the appropriate sections of this dissertation.

2.3.1 Thin films

Absorption spectra of thin films on quartz or glass substrates were measured using a Shimadzu UV-1601PC spectrophotometer. These measurements were done in transmission mode for wavelengths between 260 nm and 900 nm.

The optical properties of organic materials were further analyzed by variable angle spectroscopic ellipsometry (SOPRA GES-5). This technique measures the angle-dependent change in polarization when a light beam is reflected by the sample. From this data the refractive index and extinction coefficient were extracted for thin films of organic materials, deposited on Si/SiO_2 substrates. Furthermore, this technique was used to determine the film thickness of vacuum evaporated layers in order to calibrate the deposition rate of the material in the evaporation chamber.

Photoluminescence (PL) spectra were measured for optical excitation at 532 nm, using a N_2 laser with pulse duration of 1.2 ns operated at 20 Hz. The samples were excited through the quartz substrate at an incidence angle of 45° to the substrate normal. Emission spectra were recorded using a triple-grating monochromator coupled to an intensified CCD camera (PI-MAX from Princeton Instruments) which was synchronized by the electrical trigger of the laser. To increase the signal-to-noise ratio, spectra were accumulated by averaging over 2000 pulses.

The topography of organic films was imaged by atomic force microscopy (AFM) using an Agilent 5100 scanning probe operated in tapping mode. From these AFM images, the surface root-mean-square (RMS) roughness and folding ratio (ϕ) are calculated. The latter is defined as the ratio of the microscopic surface area and the projected scan area. Furthermore, analysis of AFM cross-sections provides information on grain sizes and step heights.

2.3.2 Devices

Current-voltage curves were measured in dark and under illumination using a Keithley 2602 parameter analyzer. An Abet Xe arc lamp was used to simulate the 100 mW/cm^2 AM1.5G solar spectrum. The light intensity was calibrated with a ISE Fraunhofer certified Si photodiode.

For EQE measurements, light from Xe (300 nm to 670 nm) and quartz halogen lamps (670 nm to 1100 nm) was coupled into a monochromator and their intensities were calibrated with a Si photodiode. The light incident on the device was chopped and the modulated current signal was detected with a current-voltage and a lock-in amplifier. The same optics and measurement setup was used with a DTR6 integrating sphere to determine the reflectance R of the complete device structure. The IQE is then estimated as EQE/(1-R).

3. Non-fullerene acceptors in organic solar cells

Solar energy conversion in organic solar cells generally relies on the dissociation of photogenerated excitons at the heterojunction between an electron-donating and an electron-accepting material (see **Section 1.3.1**). The free energy driving this charge transfer process is related to the energetic offset between the excitonic state and the charge-separated state. Transient absorption studies have shown that a reduction of this energetic driving force decreases the quantum yield of free charge carriers.[119,120] As a consequence, efficient photocurrent generation is observed only when sufficient band energy offsets are present at the heterojunction.[64,83] On the other hand, the V_{OC} of OPV devices has been shown to scale with the interface energy gap E_{DA}, being the energy difference between the HOMO level of the donor and the LUMO level of the acceptor.[65,95,96] The photocurrent and V_{OC} are thus both governed by the heterojunction energetics. Energy level engineering of the active materials is therefore crucial to further enhance the power conversion efficiency of OPV devices.

This chapter investigates the role of the acceptor material in organic photovoltaic devices. Traditionally, fullerene-based molecules are employed as the electron accepting material in an organic solar cell. However, the use of non-fullerene acceptors in organic photovoltaic devices could lead to enhanced efficiencies resulting from high V_{OC} values and improved absorption of solar light. In **Section 3.1** the advantages of alternative acceptor materials are further discussed, and the state-of-the-art fullerene-free OPV devices are explored. In **Section 3.2** a series of subphthalocyanine derivatives are employed as acceptor. The device performance is then correlated with heterojunction energetics. In **Section 3.3** non-substituted subphthalocyanines are used as acceptor, which leads to devices with high V_{OC} and efficiency.

3.1 Electron acceptors in organic photovoltaics

Various organic semiconductor materials can be applied as electron accepting material in organic photovoltaic devices. Fullerene-based molecules are commonly used due to their excellent electron transport properties. However, other small organic molecules as well as polymers have been explored as alternatives to fullerenes.

3.1.1 Fullerene acceptors

In 1992 Sariciftci et al. first described the electron transfer from a conductive polymer to fullerene C_{60}.[121] This finding gave rise to the present widespread use of fullerene-based molecules as acceptor in organic photovoltaics. In evaporated small-molecule OPV cells, fullerenes C_{60} and C_{70} are the most prevalent electron acceptors, while solution-processed devices rely mainly on substituted derivatives of these basic fullerenes.[122,123] The dominance of fullerenes as electron acceptor materials in organic photovoltaics is related to their excellent electronic properties. The relatively high electron affinity of fullerenes (around 4 eV) enables efficient charge transfer from most donor materials, while the strong electronic coupling between fullerene molecules result in a high electron mobility ($\mu_e = 3.3 \times 10^{-2}$ cm^2/(V·s) for a thin C_{60} film).[124] The tendency to form crystalline aggregates, as well as the isotropic charge transport due to the symmetric shape of fullerene molecules, further enhances the electron transport in OPV devices.

Fullerene molecules however possess weak absorption at visible wavelengths, resulting in a small absorption overlap with the solar spectrum (**Figure 1.8**). Consequently, the contribution of fullerene acceptors to the photocurrent generation in an organic solar cell is generally rather small. Moreover, the frontier molecular orbital levels of fullerene molecules cannot easily be tuned by chemical modification. Performance enhancement of OPV devices has therefore mainly relied on the development of new donor materials.[125,126] Chemical functionalization of small-molecule or polymer donor materials either adjusts the bandgap to enhance light absorption and photocurrent, or lowers the HOMO level to increase the CT state energy and V_{OC}. However, the V_{OC} of efficient fullerene-based OPV devices is generally limited below 1 V due to the small optical bandgap of fullerene acceptors.[64] Therefore, it has been suggested that non-fullerene acceptors could enable an increased V_{OC} in OPV devices without sacrificing photocurrent generation. The use of non-fullerene acceptors could leverage efficient absorption of solar light and easy energy level tuning by chemical modification. Other disadvantages of fullerene acceptors include chemical degradation under illumination,[127,128] and high production and energy costs due to low synthetic yield and material purity.[129,130]

3.1.2 Non-fullerene acceptors

An early approach to replace fullerenes in organic photovoltaics employed molecules based on an aromatic perylene core. Also the original bilayer heterojunction OPV cell reported by Tang utilized a perylene derivative as acceptor.[81] Such perylene diimide (PDI) derivatives are promising acceptor materials due to their high electron affinity, electron mobility, and superior thermal and chemical stability.[131] Moreover, the PDI LUMO energy can easily be tuned by introducing electron-rich or electron-deficient substituents at the bay position, which consequently affect the V_{OC} of the resulting devices.[132] In evaporated bilayer heterojunction devices, a V_{OC} close to

1.4 V was achieved by using diindenoperylene (DIP) as acceptor.[133] The solubility of PDI molecules can be improved by addition of alkyl chains to the imide nitrogen atoms, while terminal moieties affect the crystallinity. Nevertheless, PDI-based devices yet suffer from difficulties regarding phase segregation in the blend. In solution-processed devices, a PCE of 3.88% has been achieved by combining a symmetrical PDI derivative with a small-molecule donor.[134]

The prospect of enhanced device performance triggered the development of both non-fullerene molecular and polymeric acceptor materials.[135–137] Besides PDI-based molecules, many non-fullerene small-molecule acceptors for solution-processed devices are based on compounds such as diketopyrrolopyrrole,[138] truxenones,[139,140] oligothiophenes,[141,142] and polyacenes;[143] whereas polymer acceptors include cyanated poly(phenylene vinylene),[144,145] and (co-)polymers based on PDI or naphthalene diimide (NDI) units.[146,147] These efforts resulted in improved insight in the development of electron acceptor materials. Besides good electron transport properties and high electron affinity, effective non-fullerene acceptors require extended electron delocalization and weak intermolecular interactions with the donor. Recently, efficiencies exceeding 6% have been reported for polymer solar cells using small-molecule acceptors,[148–151] as well as for all-polymer solar cells.[152] The record efficiency of 6.8% for fullerene-free polymer solar cells was achieved by introducing an acceptor molecule comprising a fused heteroacene core.[153] Clearly, the newest non-fullerene acceptors in solution-processed OPV devices are challenging their fullerene counterparts. However, these solution-processed devices still require careful process optimization by adding co-solvents and applying post-deposition treatments.

In evaporated small-molecule OPV devices, mainly phthalocyanine derivatives have been explored as non-fullerene acceptors. The frontier molecular orbital energy levels of these typical donor materials are lowered by addition of electron-withdrawing substituents on the peripheral positions of their aromatic ring structure,[154–156] enabling the use of these derivative compounds as electron acceptor. However, the use of peripherally halogenated phthalocyanines as non-fullerene acceptor resulted in poor device efficiencies.[157] Similar to phthalocyanines, peripheral halogenation of subphthalocyanines results in a shift of the molecular orbital energy levels. Axial substitution of the chlorine atom, on the other hand, has shown little effect on the molecular orbital levels.[20] Both peripherally and axially substituted SubPc molecules have been applied as electron acceptor material, resulting in high-voltage devices with V_{OC} up to 1.3 V.[158–160] However, low quantum efficiencies and the overlapping absorption profiles of donor and acceptor materials resulted in low photocurrent generation. A fused fluorinated SubPc dimer was used to shift the absorption spectrum of the acceptor to longer wavelengths. With an absorption profile complementary to the (unsubstituted) SubPc donor, this fused compound yielded a higher photocurrent, and an efficiency of 4% was achieved.[161] Recently, efficiencies over 6% were reported for a heterojunction consisting of a SubNc donor and a hexachlorinated SubPc acceptor.[162]

3.2 Energy level tuning of non-fullerene acceptors

This section investigates the correlation between the performance of organic solar cells and their heterojunction energetics by using a unique series of non-fullerene acceptor materials. Four subphthalocyanine derivatives with various electron-withdrawing substituents (-F, -Cl, and -CN) are combined with four small-bandgap donor materials in planar-heterojunction device structures.[163] The peripheral substituents on the subphthalocyanine molecules cause a shift of their LUMO energy levels, without affecting other properties such as bandgap and absorption spectrum. This energy level tuning simplifies the optimization of interface energetics in donor-acceptor heterojunctions. In combination with the small-bandgap donor materials, the effect of heterojunction energetics on device performance is systematically studied. Next, adjustment of the charge transport layers in the device structure results in highly efficient OPV devices. Finally, these non-fullerene acceptors are compared with the fullerene C_{60}.

3.2.1 Subphthalocyanine derivatives

Four peripherally substituted SubPc derivatives (**Figure 3.1(a)**) were synthesized: two partially chlorinated SubPc molecules (Cl_4-SubPc-Cl and Cl_6-SubPc-Cl), a fully fluorinated SubPc molecule (F_{12}-SubPc-Cl), and a tricyanated SubPc molecule ($(CN)_3$-SubPc-F);* where the latter contains a fluoride as axial ligand, instead of a chloride. The F_{12}-SubPc-Cl and Cl_6-SubPc-Cl compounds were synthesized as described in the literature.[162,164] The Cl_4-SubPc-Cl compound was prepared by cross-condensation of 4,5-dichlorophthalonitrile[165] and phthalonitrile. The $(CN)_3$-SubPc-F compound was prepared by palladium-mediated cyanation of triiodo-SubPc-OPh^{t}Bu,[166] and subsequent phenoxy group to fluorine axial exchange.[167] All four SubPc derivatives have very similar absorption spectra in solution (**Figure 3.2(a)**), peaking at wavelengths around 570 nm. The electron affinities of these molecules, indicative of their LUMO energies, were estimated from the reduction potential obtained by cyclic voltammetry measurements. The electron withdrawing character of the peripheral substituents lowers the frontier orbital energies of the SubPc molecule, resulting in LUMO energies ranging from -3.54 eV to -3.85 eV (**Figure 3.1(c)**). Caution should be used when comparing these LUMO levels with molecular energy levels in the literature.[30] First of all, cyclic voltammetry measurements yield an approximate value of the electron affinity (and LUMO energy). Secondly, the literature employs many different approaches to measure and report molecular energy levels, and the experimental error is often large. Therefore, the LUMO levels and interface bandgap energies indicated here only serve to reflect the relative positions of the transport energy levels for the different SubPc derivatives, rather than representing absolute energetic values. More information about the synthesis and characterization of the SubPc derivatives is given in the **Appendix**.

---

* This compound is in fact a 1:3 mixture of C_3 and C_1 regioisomers.

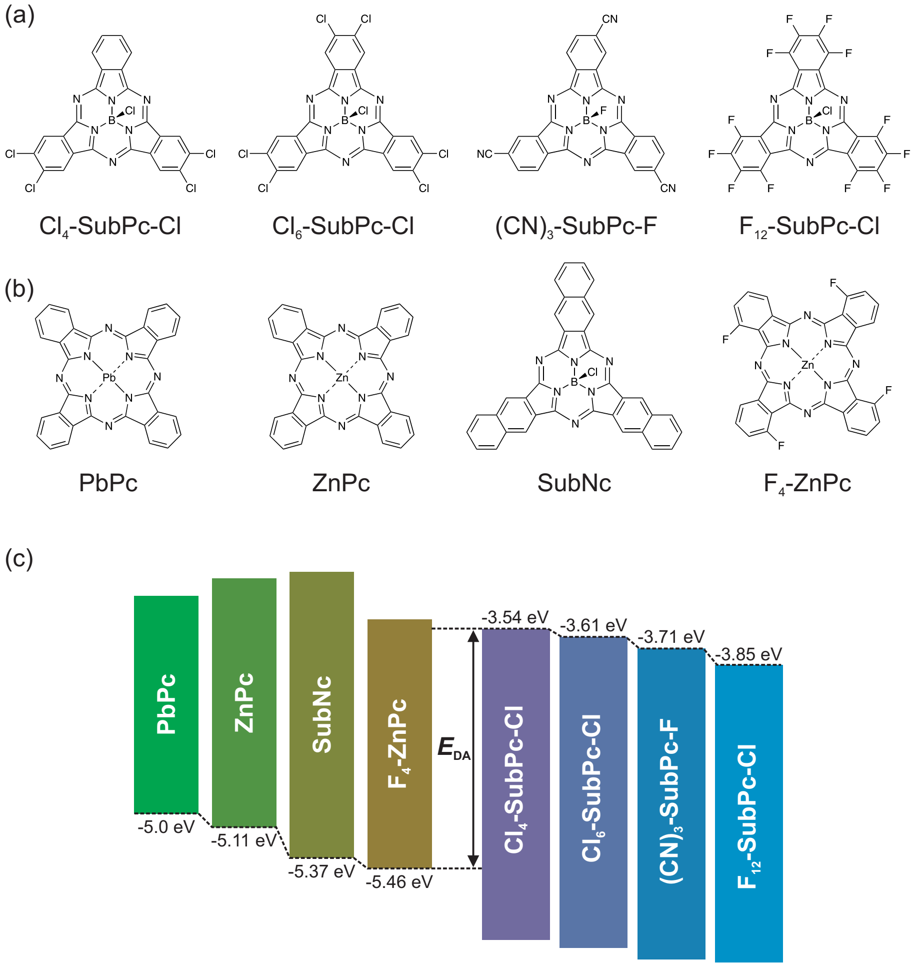

Figure 3.1: Molecular structure of (a) the SubPc derivatives, and (b) the small-bandgap donor materials used to systematically study the effect of heterojunction energetics on device performance. (c) Schematic representation of the LUMO energy levels of the SubPc acceptors, the HOMO energy levels of the donors, and the interface bandgap E_{DA}.[163]

ACKNOWLEDGEMENT
The synthesis and characterization of the subphthalocyanine derivatives was performed at the Universidad Autónomica de Madrid by Germán Zango, Victoria Martinez-Diaz, and Tomás Torres.

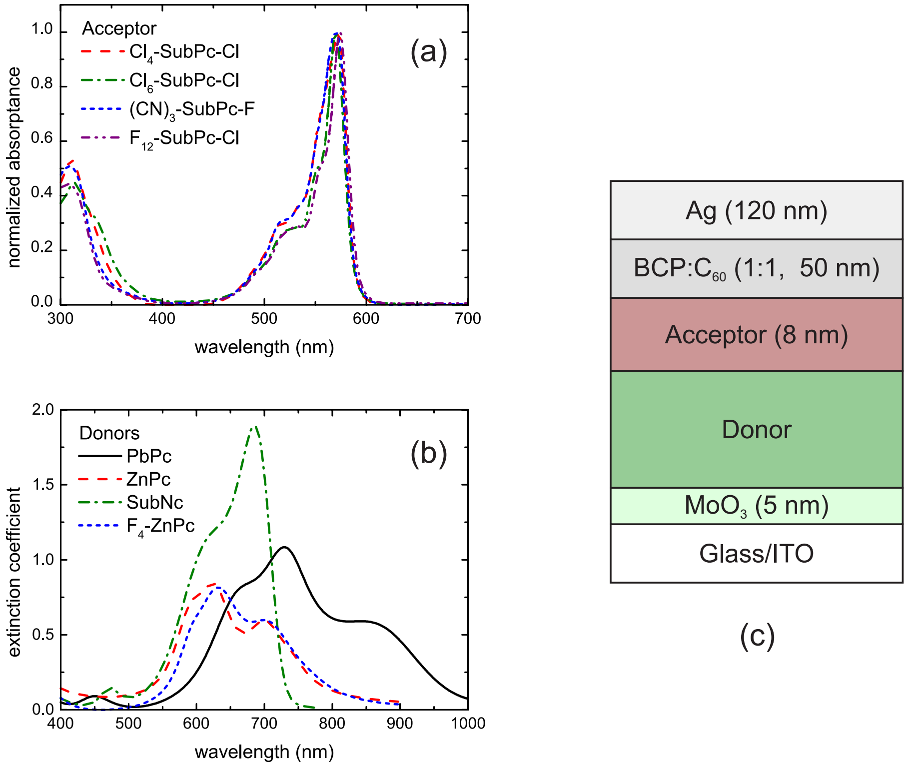

Figure 3.2: (a) Normalized absorption spectra of the SubPc derivatives in chloroform solution. (b) Extinction coefficients of the donor materials, determined by spectroscopic ellipsometry of thin films on Si/SiO_2 substrates. (c) Schematic illustration of the general device structure incorporating non-fullerene acceptors.

3.2.2 Device structure

Planar-heterojunction devices were fabricated using the above mentioned SubPc derivatives as acceptor. These non-fullerene acceptors were combined with the following small-bandgap donor materials (**Figure 3.1(b)**): lead phthalocyanine (PbPc), zinc phthalocyanine (ZnPc), chloro boron subnaphthalocyanine (SubNc), and tetra-fluoro zinc phthalocyanine (F_4-ZnPc). These donor molecules were selected to span a range of HOMO energy levels, being -5.0 eV, -5.11 eV, -5.37 eV, and -5.46 eV, respectively.[47,115,116] Due to their smaller bandgap, all donor materials have absorption spectra complementary to the SubPc acceptors (**Figure 3.2(b)**). A 14 nm thick donor layer was deposited for SubNc, while a thickness of 40 nm was chosen for the other phthalocyanine donors. The thickness of the acceptor layer was set at 8 nm, irrespective of which SubPc derivative was used. Insertion of 5 nm MoO_3 at the anode interface ensures good hole extraction due to an improved energy level alignment with the donor materials.[168] A 50 nm thick 1:1 blend of BCP and C_{60} was used as electron transport layer (ETL). The low optical absorption and high conductivity of this layer ensures sufficient optical spacer thickness without compromising electron extraction.[114] Previous reports have shown that the presence of fullerene in the ETL does not actively contribute to the photocurrent generation.[161,162]

The general device structure incorporating the non-fullerene acceptors is illustrated in **Figure 3.2(c)**. The combination of each SubPc derivative with several donor materials results in a large set of bilayer devices. The effect of heterojunction energetics on device performance was assessed by *J-V* measurements under 100 mW/cm^2 AM1.5G illumination (**Figure 3.3** and **Table 3.1**).

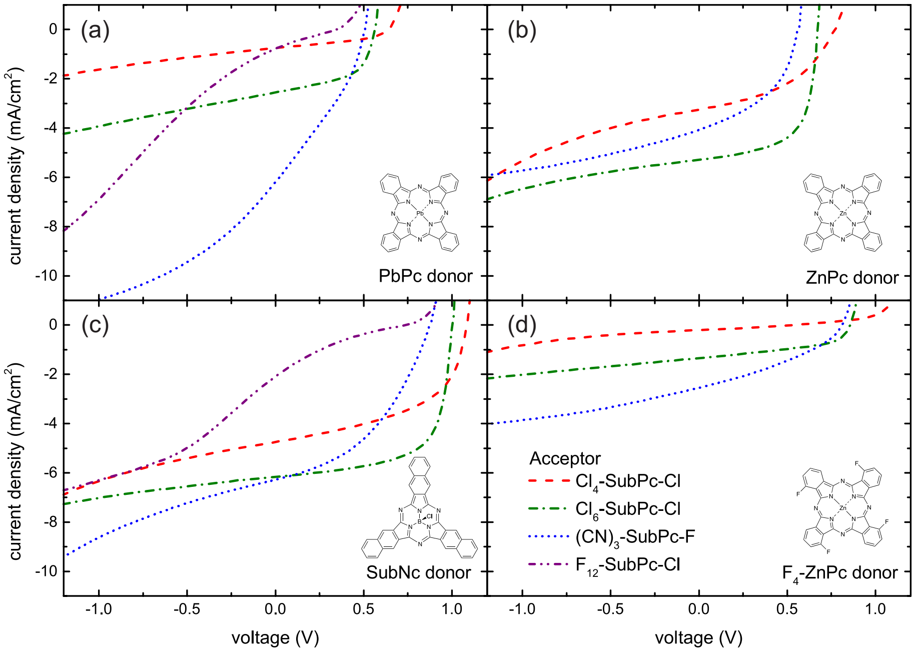

Figure 3.3: Current density-voltage curves, measured under 100 mW/cm^2 AM1.5G illumination, of planar-heterojunction devices comprising (a) PbPc, (b) ZnPc, (c) SubNc, and (d) F$_4$-ZnPc as donor, and different SubPc derivatives as acceptor.

Table 3.1: Interface energy gap (E_{DA}) and solar cell performance parameters, measured under 100 mW/cm^2 AM1.5G illumination, for planar-heterojunction devices with small-bandgap molecules as donor and SubPc derivatives as acceptor.*

Donor	Acceptor	E_{DA} (eV)	V_{OC} (V)	J_{SC} (mA/cm^2)	FF (%)	PCE (%)
PbPc	F_{12}-SubPc-Cl	1.15	0.33 (± 0.01)	0.88 (± 0.07)	23.4 (± 0.2)	0.07 (± 0.01)
	$(CN)_3$-SubPc-F	1.29	0.50 (± 0.01)	6.00 (± 0.1)	32.5 (± 0.4)	0.97 (± 0.02)
	Cl_6-SubPc-Cl	1.39	0.57 (± 0.01)	2.51 (± 0.03)	53.9 (± 0.5)	0.76 (± 0.01)
	Cl_4-SubPc-Cl	1.46	0.64 (± 0.01)	0.76 (± 0.01)	40.1 (± 1.4)	0.19 (± 0.01)
ZnPc	$(CN)_3$-SubPc-F	1.40	0.56 (± 0.01)	4.07 (± 0.04)	43.5 (± 0.7)	0.97 (± 0.02)
	Cl_6-SubPc-Cl	1.50	0.67 (± 0.01)	5.28 (± 0.01)	62.6 (± 1.2)	2.23 (± 0.03)
	Cl_4-SubPc-Cl	1.57	0.77 (± 0.01)	3.25 (± 0.01)	43.9 (± 1.0)	1.10 (± 0.02)
SubNc	F_{12}-SubPc-Cl	1.52	0.75 (± 0.01)	2.4 (± 0.2)	17.2 (± 0.3)	0.30 (± 0.03)
	$(CN)_3$-SubPc-F	1.66	0.89 (± 0.01)	6.18 (± 0.08)	43.2 (± 0.6)	2.36 (± 0.03)
	Cl_6-SubPc-Cl	1.76	1.00 (± 0.01)	6.12 (± 0.04)	65.3 (± 0.4)	3.89 (± 0.04)
	Cl_4-SubPc-Cl	1.83	1.08 (± 0.01)	4.83 (± 0.07)	48.2 (± 3.0)	2.44 (± 0.14)
F_4-ZnPc	$(CN)_3$-SubPc-F	1.75	0.81 (± 0.01)	2.52 (± 0.04)	34.8 (± 0.4)	0.70 (± 0.01)
	Cl_6-SubPc-Cl	1.85	0.87 (± 0.01)	1.34 (± 0.01)	47.4 (± 0.5)	0.53 (± 0.01)
	Cl_4-SubPc-Cl	1.92	0.66 (± 0.1)	0.21 (± 0.02)	26.3 (± 1.1)	0.04 (± 0.01)

* Average values and standard deviations are calculated for at least 3 devices on a single substrate.

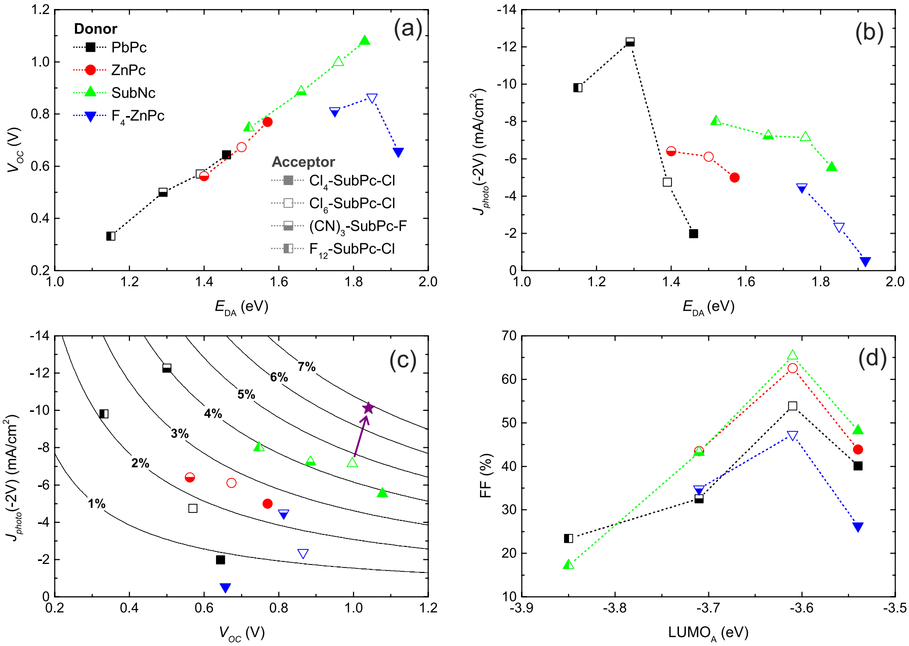

Figure 3.4: Relation of OPV performance parameters to the heterojunction energetics. (a) The V_{OC} scales linearly with the interface bandgap energy E_{DA}. (b) The photocurrent generally decreases with the interface bandgap energy E_{DA}. (c) The trade-off between photocurrent and V_{OC} limits the PCE of organic heterojunction devices. The contour lines represent the calculated PCE, assuming a 65% FF and a voltage-independent photocurrent (J_{photo}(-2 V) = J_{SC}). The arrow indicates a device with an exciton-blocking hole transport layer, which increases the photocurrent. (d) The FF is related to the acceptor LUMO energy by the formation of electron injection or extraction barriers.[163]

3.2.3 Effect of heterojunction energetics on device performance

In this set of bilayer devices the V_{OC} ranges from 0.3 V to 1.1 V. For a single donor material the V_{OC} can be tuned by 0.3 V depending on the choice of the SubPc acceptor. **Figure 3.4(a)** shows that V_{OC} increases linearly with the interface energy gap E_{DA}. This corresponds to the well-known trend reported in the literature, correlating V_{OC} with the interface energetics.[78,79,95,96] The upper limit for V_{OC} is determined by the CT state energy,[77] which is closely related to the interface gap E_{DA}. However, the measured V_{OC} in organic heterojunction devices never reaches this upper limit due to energy losses resulting from charge carrier recombination. The linear increase of V_{OC} with E_{DA} thus suggests that the different recombination processes occurring in these planar-heterojunction devices generally don't influence V_{OC}. Only devices with a F_4-ZnPc donor yield a reduced V_{OC} compared with the other donor materials, possibly resulting from significantly increased recombination losses. However, the reduced V_{OC} could also be related to dipole formation at the F_4-ZnPc interface, as was suggested after similar observations for fullerene-based devices.[155] Hence, also considering the large uncertainty on the reported frontier orbital energies in the literature, both interface energetics and recombination dynamics at non-fullerene heterojunctions are subject to further investigation. The remarkably low V_{OC} for the device with the largest interface gap, i.e. the combination of F_4-ZnPc and Cl_4-SubPc-Cl, is a consequence of the lack of photocurrent generation at this heterojunction. With no free charge carriers available, no considerable photovoltage can be generated in this device structure. Disregarding the F_4-ZnPc-based devices, the average difference between E_{DA} and $q \cdot V_{OC}$ is 0.8 eV. This value corresponds to previous reports,[95,96] considering the estimated interface energy gap E_{DA} exceeds the CT state energy by the CT state binding energy. The advantage of the SubPc acceptors hence lies in the facile tuning of the interface energy gap E_{DA}, rather than reducing the energy losses at the active heterojunction.

The lack of photocurrent generation in the F_4-ZnPc/Cl_4-SubPc-Cl device warrants further investigation of the photocurrent dependence on the heterojunction energetics. Dissociation of bound excitons into free charge carriers is assumed to proceed through an intermediate CT state. A high quantum yield of free charge carriers is obtained only if this charge transfer process is energetically favorable. As the interface energy gap E_{DA} is closely related to the CT state energy, a correlation of E_{DA} with photocurrent generation is expected. Hence, the relation between photocurrent and E_{DA} was examined for all studied donor-acceptor heterojunctions (**Figure 3.4(b)**). The photocurrent generation differs significantly for devices with different donor layers, depending on the absorption and spectral response of the specific donor material. In contrast, the different SubPc derivatives all have similar absorption spectra, and the variation in photocurrent density upon changing the acceptor material in these devices is therefore a good indication of their internal quantum efficiencies. The photocurrent density is evaluated at reverse bias (-2 V), as the photocurrent at short-circuit conditions is reduced by charge extraction issues in some device structures (see discussion further in this section). **Figure 3.4(b)** reveals a general trend toward low photocurrent generation at large E_{DA} for all donor materials. Similar to previous reports,[64,83,119,120] the reduced photocurrent is a consequence of the smaller free energy driving the charge transfer process. The maximal interface gap where efficient charge transfer still occurs differs for every donor material, and depends on the optical bandgap of the donor. For example, devices with a SubNc donor, which has the largest bandgap (~ 2.3 eV) of the studied donor materials, can generate reasonable photocurrent with all SubPc acceptors. In contrast, for devices containing PbPc, the smallest-bandgap donor (~ 1.7 eV) in this study, the photocurrent is significantly reduced when E_{DA} increases. In case of the F_4-ZnPc/Cl_4-SubPc-Cl heterojunction, E_{DA} is too large (1.92 eV) and the CT state energy equals or exceeds the donor exciton energy. As a consequence, no free charges are generated at the heterojunction, and nearly no photocurrent is produced in this device structure. These observations confirm the correlation between heterojunction energetics and charge generation kinetics at the donor-acceptor interface. On the other hand, the reduction of the interface energy gap does not necessarily yield a photocurrent increase. At low E_{DA} the charge generation saturates, or even decreases when the charge transfer reaction occurs in the Marcus inverted region.[79] The reduced photocurrent for the PbPc/F_{12}-SubPc-Cl device (E_{DA} = 1.15 eV) could be related to such an impaired charge transfer reaction. Besides heterojunction energetics, other material properties determine the total photocurrent extraction in these devices, such as charge mobility, bulk recombination, layer morphology and crystallinity. The degree at which these parameters affect the photocurrent however requires further material characterization and is therefore subject for future research.

Figure 3.4(a) and **Figure 3.4(b)** make clear that V_{OC} and photocurrent exhibit opposite trends with respect to the interface energy gap E_{DA}: while V_{OC} linearly increases with E_{DA}, photocurrent generally decreases for large E_{DA}. As a result of this trade-off between V_{OC} and photocurrent, efficiency enhancement of a heterojunction OPV device relies on optimization of the interface energy gap. Both E_{DA} and V_{OC} should be maximized without substantial reduction of the photocurrent. **Figure 3.4(c)** illustrates this trade-off for the presented planar-heterojunction devices. With the contour lines indicating the calculated PCE, assuming a 65% FF and a voltage-independent photocurrent, the highest PCE is expected for the combination of a SubNc donor with a Cl_6-SubPc-Cl acceptor. Disregarding possible variations in FF, all remaining donor-acceptor pairs yield either a reduced V_{OC} or photocurrent, and consequently cannot obtain higher efficiencies. For a specific donor material, however, the PCE can easily be maximized by selecting the most appropriate acceptor material, illustrating the advantage of SubPc LUMO energy level tuning over fullerene acceptors.

Figure 3.4(d) plots the measured FF as a function of the LUMO energy of the SubPc acceptors. While the Cl_6-SubPc-Cl acceptor yields FFs up to 65%, severe S-kinks in the *J*-*V* curve reduce the FF below 25% for the F_{12}-SubPc-Cl acceptor. Low fill factors are often attributed to limited charge extraction by low charge carrier mobility or high bulk recombination in the device structure. The series resistance extracted from the measured *J*-*V* curves is however similar for all donor-acceptor combinations in our study, indicating that potential mobility or bulk recombination effects are not the main cause of the reduced FF. The observed S-kinks are known to occur in planar-heterojunction devices when injection or extraction barriers are present at the interface between the active layers and the charge transport layers.[71] In this device set, the FF is mainly determined by the choice of acceptor material, indicating that the energy alignment at the acceptor/ETL interface is critical to avoid S-kink manifestation. As electron extraction in the BCP:C_{60} ETL likely occurs through percolating conductive pathways of fullerene molecules, this blend functions as an excellent ETL for fullerene acceptors.[114] However, a BCP:C_{60} ETL likely gives rise to charge injection or extraction barriers in combination with most non-fullerene acceptors, and energy level alignment between the SubPc acceptor and C_{60} is required to achieve high FFs. Clearly, Cl_6-SubPc-Cl fulfills this requirement, which explains the highly efficient devices obtained in previous work.[162] The remaining acceptor materials either form an extraction (F_{12}-SubPc-Cl and $(CN)_3$-SubPc-F) or injection barrier (Cl_4-SubPc-Cl) with the BCP:C_{60} ETL, resulting in reduced FFs.*

---

* As the C_{60} LUMO energy is often reported around -3.9 eV,[95] it is repeated that the indicated Cl_6-SubPc-Cl LUMO energy of -3.61 eV is only approximate, and the claimed energy alignment is thus within experimental uncertainty.

3.2.4 Charge transport layers

With an average FF of 65.3%, the SubNc/Cl_6-SubPc-Cl heterojunction indeed yields the highest PCE in this systematic study, as expected from **Figure 3.4(c)**. Due to a voltage-dependent photocurrent the average PCE is yet limited to 3.9% in the general device structure, comprising MoO_3 as HTL and BCP:C_{60} as ETL. Specific modification of these transport layers can however further enhance performance of these planar-heterojunction devices. **Figure 3.5** shows the measured *J-V* curves for the following device structures with adjusted electron and hole transport layers. The corresponding performance parameters are summarized in **Table 3.2**.

A. ITO/MoO_3 (5 nm)/SubNc (14 nm)/F_{12}-SubPc-Cl (8 nm)/BCP:C_{60} (1:1, 50 nm)/Ag

B. ITO/MoO_3 (5 nm)/SubNc (14 nm)/F_{12}-SubPc-Cl (8 nm)/BCP:Yb (5%, 50 nm)/Ag

C. ITO/PEDOT:PSS/DIP (5 nm)/SubNc (14 nm)/F_{12}-SubPc-Cl (8 nm)/BCP:Yb (5%, 50 nm)/Ag

D. ITO/MoO_3 (5 nm)/SubNc (14 nm)/Cl_6-SubPc-Cl (8 nm)/BCP:C_{60} (1:1, 50 nm)/Ag

E. ITO/PEDOT:PSS/DIP (5 nm)/SubNc (14 nm)/Cl_6-SubPc-Cl (8 nm)/BCP:C_{60} (1:1, 50 nm)/Ag

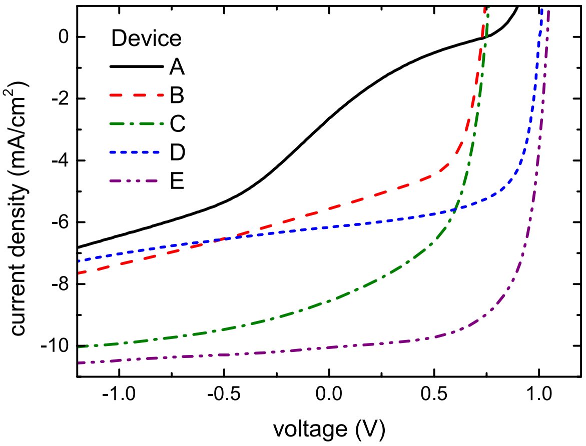

Figure 3.5: Current density-voltage curves, measured under 100 mW/cm^2 AM1.5G illumination, for planar-heterojunction devices with different electron and hole transport layers: (**A**) MoO_3/SubNc/F_{12}-SubPc-Cl/BCP:C_{60}, (**B**) MoO_3/SubNc/F_{12}-SubPc-Cl/BCP:Yb, (**C**) PEDOT:PSS/DIP/SubNc/F_{12}-SubPc-Cl/BCP:Yb, (**D**) MoO_3/SubNc/Cl_6-SubPc-Cl/BCP:C_{60}, and (**E**) PEDOT:PSS/DIP/SubNc/Cl_6-SubPc-Cl/BCP:C_{60}.[163]

In device structures with a F_{12}-SubPc-Cl acceptor layer, the BCP:C_{60} ETL is replaced with an Yb-doped BCP layer. The high conductivity of this BCP:Yb layer ensures a good electron extraction, even at the high thickness needed in these devices structures.[72] **Figure 3.5** illustrates that the severe S-kink in device **A** is no longer present for the BCP:Yb ETL in device **B**, confirming that BCP:C_{60} indeed impedes electron extraction from the F_{12}-SubPc-Cl acceptor. However, a parasitic photoshunt effect in these devices limits the FF to 57%. The photocurrent slope at reverse bias does not depend on the choice of the electron transport layer. The origin of this photoshunt is therefore likely related to bulk effects in the active layers of the device.[169,170] In Cl_6-SubPc-Cl-based devices, for which S-kinks were not present, replacement of the ETL does not significantly affect the FF. However, the photocurrent is slightly reduced with BCP:Yb as ETL, which could result from exciton quenching by Yb-clusters in the ETL or slight changes in the optical interference pattern.

At the anode interface, a MoO_3 HTL was used to ensure efficient hole extraction from all donor layers.[168] Unfortunately MoO_3 also significantly reduces the photocurrent due to quenching of donor excitons at its interface.[171,172] The introduction of exciton-blocking[59,173] or exciton-dissociating HTLs[115,172] has been shown to significantly improve photocurrent generation in planar-heterojunction devices. Recently, DIP was introduced as exciton-blocking HTL for SubNc-based devices.[162] To ensure that DIP forms a closed layer during evaporation, a spin-coated PEDOT:PSS layer is used to provide a smooth growth surface. Indeed, the replacement of MoO_3 by DIP increases the J_{SC} by 54% in device **C**. Also V_{OC} slightly increases upon insertion of the exciton-blocking DIP layer. With both ETL and HTL replaced in the SubNc/F_{12}-SubPc-Cl heterojunction device, the PCE of 3.31% is nearly a tenfold increase compared with the original device structure. Also for the champion heterojunction, comprising a SubNc donor and Cl_6-SubPc-Cl acceptor (device **D**), the photocurrent is further boosted by introducing an exciton-blocking DIP layer at the anode (device **E**). The increased J_{SC} of 10.1 mA/cm^2 leads to further efficiency enhancement for this heterojunction, as illustrated in **Figure 3.4(c)**. Moreover, with a V_{OC} above 1 V and a FF of 67%, the resulting PCE of 6.9% is among the highest reported efficiencies for bilayer OPV devices with a non-fullerene acceptor.

Table 3.2: Solar cell performance parameters measured under 100 mW/cm^2 AM1.5G illumination for planar-heterojunction devices with different electron and hole transport layers.*

Device structure	**V_{OC} (V)**	**J_{SC} (mA/cm^2)**	**FF (%)**	**PCE (%)**
A: MoO_3/SubNc/F_{12}-SubPc-Cl/BCP:C_{60}	0.75	2.64	17.4	0.34
B: MoO_3/SubNc/F_{12}-SubPc-Cl/BCP:Yb	0.73	5.57	57.6	2.25
C: PEDOT:PSS/DIP/SubNc/F_{12}-SubPc-Cl/BCP:Yb	0.75	8.55	53.4	3.31
D: MoO_3/SubNc/Cl_6-SubPc-Cl/BCP:C_{60}	1.00	6.17	65.9	3.96
E: PEDOT:PSS/DIP/SubNc/Cl_6-SubPc-Cl/BCP:C_{60}	1.04	10.1	66.6	6.86

* For each device structure the performance parameters of the best performing cell are given.

3.2.5 Comparison with C_{60}

As a result of the optimization of heterojunction energetics and charge transport layers, OPV devices with a non-fullerene acceptor can compete with their fullerene-based counterparts. For comparison, the Cl_6-SubPc-Cl acceptor in device **E** is replaced by a C_{60} layer. From the *J-V* curves it is clear the use of the non-fullerene acceptor almost doubles the efficiency of the device (**Figure 3.6(a)**). The increase in J_{SC} results from the enhanced absorption of visible light by the SubPc derivative. The increase in FF is related to decreased recombination at the SubNc interface.[162] The increase in V_{OC} could be caused by a larger interface energy gap. However, as mentioned before, it is difficult to compare the LUMO energy of Cl_6-SubPc-Cl and C_{60} due to the large experimental uncertainty. The LUMO of Cl_6-SubPc-Cl was estimated at -3.61 eV by cyclic voltammetry measurements, whereas the C_{60} LUMO is often reported around -3.9 eV in the literature.[95] Nevertheless, the V_{OC} difference induced by these acceptors is only 0.17 V. A more accurate comparison of the heterojunction energetics follows from the analysis of the electroluminescence (EL) spectra. The EL spectra of both SubNc/Cl_6-SubPc-Cl and SubNc/C_{60} heterojunctions shows a broad peak at high wavelengths (**Figure 3.6(b)**), corresponding to the CT state emission. By fitting these peaks with a Gaussian function, the peak positions of the CT state emission are determined at 1.27 eV and 1.37 eV for the SubNc/C_{60} and SubNc/Cl_6-SubPc-Cl heterojunction, respectively. A linear relation between this CT emission peak position and V_{OC} have been reported previously.[62,65] The V_{OC} increase for the non-fullerene acceptor is thus partly related to the interface energetics. Other factors influencing the V_{OC} are the molecular reorganization energy upon CT state formation and the recombination rate at the donor-acceptor interface.

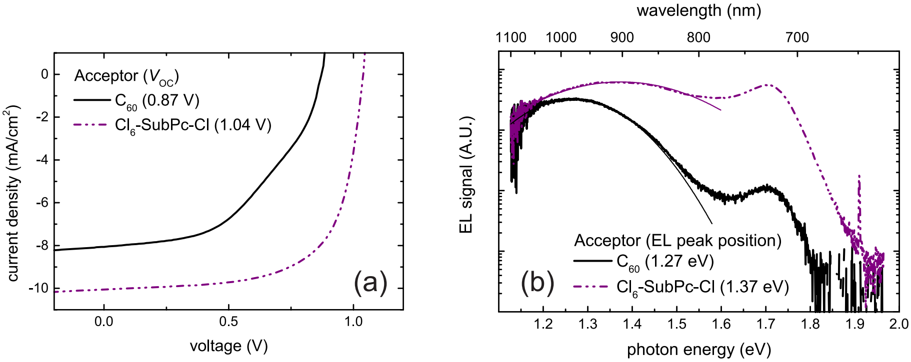

Figure 3.6: (a) Current density-voltage curves, measured under 100 mW/cm² AM1.5G illumination, and (b) electroluminescence measurements for planar-heterojunction devices based on SubNc/C_{60} and SubNc/Cl_6-SubPc-Cl. The thin solid lines are Gaussian fits of the CT state emission band.

ACKNOWLEDGEMENT
Electroluminescence measurements were performed by Kristofer Tvingstedt at Würzburg University. Kristofer Tvingstedt and Carsten Deibel are also gratefully acknowledged for fruitful discussions.

3.3 Non-substituted subphthalocyanines as acceptor

In this section, SubPc and SubNc are tested as electron acceptors in bilayer heterojunction devices. Without electron-withdrawing substituents, these molecules are commonly used as electron donor material in OPV devices.[20,22,174–176] In combination with fullerene acceptors, power conversion efficiencies of 4% to 5% have been reported.[173,177,178] However, SubPc has also been shown to act as acceptor material, provided that the selected donor material supplies sufficient energy offsets to enable efficient exciton dissociation at the heterojunction. In combination with a tetracene (Tc) donor OPV cells with a 2.9% efficiency were achieved.[179] Here, in addition to Tc, α-sexithiophene (α-6T) is used as donor material in combination with SubPc and SubNc as acceptor (**Figure 3.7**).

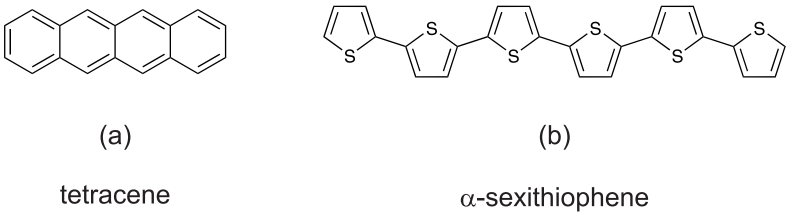

Figure 3.7: Molecular structure of donor materials (a) tetracene and (b) α-sexithiophene.

Oligoacenes and oligothiophenes have long been recognized as promising organic semiconductors due to their excellent charge transport properties resulting from their planar molecular structure and crystalline ordering. Hole mobilities exceeding 1 $cm^2/(V{\cdot}s)$ have been reported for field-effect transistors based on thin films of pentacene and tetracene.[180] In addition, their high exciton diffusion lengths make these materials excellent candidates as donor material in organic photovoltaic devices. However, their relatively high ionization energy results in low V_{OC} in combination with fullerene acceptors. Devices based on bilayer heterojunctions of α-6T and C_{60} resulted in PCE below 1% with a V_{OC} of 0.35 V.[181] The use of Tc as donor increases the V_{OC} to 0.58 V and PCE to 2.3%.[182] Organic solar cells based on these crystalline donor materials therefore require non-fullerene acceptors to obtain higher V_{OC} values, and consequently realize higher power conversion efficiencies.

In addition to enabling efficient exciton dissociation by forming an active heterojunction with the selected donor material, the SubPc or SubNc acceptor layer also need to allow efficient electron transport to the cathode. To determine the electron mobilities of SubPc and SubNc the *J-V* curves of electron-only devices were measured (**Figure 3.8**). These devices consisted of a 100 nm thick organic layer inserted between two Yb-doped BCP layers as the electron-injecting contacts. The *J-V* curves were fitted by a space-charge-limited-current model described by

$$J = \frac{9}{8}\varepsilon\varepsilon_0\mu_0 \cdot \exp\left(0.89\,\gamma\sqrt{\frac{V}{L}}\right) \cdot \frac{V^2}{L^3} \tag{3.1}$$

where ε_0 is the permittivity of free space, and $\varepsilon = 4$ is assumed for the relative permittivity of the organic layer. The electron mobility is assumed to follow a field-dependent Poole-Frenkel behavior. The zero-field mobility μ_0 and the field activation parameter γ are used as fitting parameters, while V and L are the applied voltage and the thickness of the organic layer, respectively. The obtained SubPc electron mobility (4.9×10^{-6} cm^2/(V·s)) corresponds closely to literature values. Moreover, this value is in the same order of magnitude as the hexachlorinated SubPc acceptor used in **Section 3.2**.[183] Although the electron mobility of SubNc is even lower (4.2×10^{-9} cm^2/(V·s)), the use of SubNc as electron acceptor still results in efficient OPV devices. Due to the high absorption coefficients of SubPc and SubNc only thin acceptor layers are required in these devices. Consequently, the photogenerated electrons are still efficiently collected at the cathode despite the low electron mobility of the acceptor.

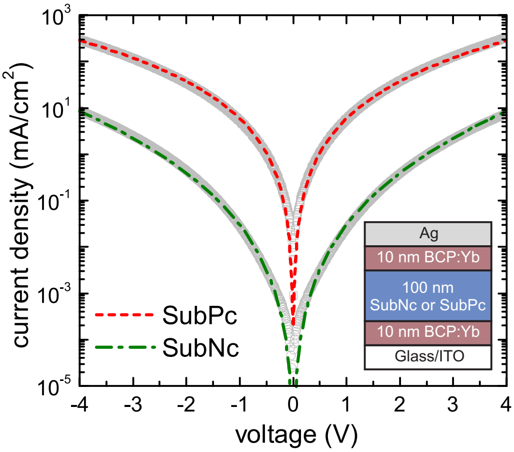

Figure 3.8: Electron mobility measurements for SubPc and SubNc. The measured *J-V* curves (grey open symbols) are fitted using a space-charge-limited-current model (dashed lines). The extracted zero-field mobilities (μ_0) and field-activation parameters (γ) are $\mu_0 = 4.89 \times 10^{-6}$ cm^2/(V·s) and $\gamma = 3.93$ cm$^{1/2}$/MV$^{1/2}$ for SubPc, and $\mu_0 = 4.21 \times 10^{-9}$ cm^2/(V·s) and $\gamma = 1.02 \times 10^{-2}$ cm$^{1/2}$/MV$^{1/2}$ for SubNc. The structure of the electron-only devices is depicted in the inset.

Bilayer devices were fabricated on ITO-coated glass substrates with the following layer structure: PEDOT:PSS/*Donor*/*Acceptor*/BCP/Ag, where the *Donor* is either Tc or α-6T, and the *Acceptor* layer consists of C_{60}, SubPc, or SubNc.[184,185] Due to the tendency of Tc and α-6T to form crystalline aggregates instead of a closed layer, a spin-coated PEDOT:PSS layer is needed to prevent device shunting. Besides serving as hole-selective contact, the smooth PEDOT:PSS surface also results in a reduced roughness of the crystalline donor layer grown on top. In addition, the Tc donor layer was deposited at an elevated rate of 3 Å/s. The nominal thickness of the donor layer was fixed at 60 nm, considering it does not significantly influence the device performance within a certain thickness range.[181] For the Tc-based devices the thickness of the acceptor layer was 30 nm, and a 10-nm BCP layer was added to prevent exciton quenching at the cathode. A 5-nm MoO_3 layer was also inserted at the anode, and the Ag cathode was replaced by Al to reduce charge injection barriers. For the α-6T based devices, the thickness of the acceptor layer and the BCP layer were optimized to maximize the PCE for each device structure. The thickness of the BCP exciton-blocking layer has a large influence on the device performance because BCP might impede electron extraction from the non-fullerene acceptors.[113] This results in a different optimal thickness of the BCP layer for each acceptor material. Current density-voltage measurements were measured under 100 mW/cm^2 AM1.5G illumination (**Figure 3.9**), and the corresponding performance parameters are summarized in **Table 3.3**.

A PCE of 1.92% was obtained for the Tc/C_{60} device. Efficiencies of 2.3% have been reported in the literature, where the high J_{SC} of 7.0 mA/cm^2 could have sourced from a larger donor-acceptor interface area due to the high surface roughness of the Tc layer.[182] Here, the high deposition rate of Tc and the planarizing PEDOT:PSS layer result in a smoother Tc surface with RMS roughness of 6.9 nm, measured by AFM (**Figure 3.10(a)**). In contrast, the α-6T/C_{60} device achieves higher V_{OC} and J_{SC} values compared with the literature,[181] resulting in a PCE just above 1%. The fullerene-free devices all obtain enhanced efficiencies owing to their high V_{OC} values. The Tc/SubPc device achieves the highest V_{OC} of 1.2 V. Both V_{OC} and J_{SC} for this device are comparable with previously reported devices,[179] but the higher FF yields a PCE above 3%. The other fullerene-free devices additionally achieve an enhanced J_{SC} compared with the C_{60}-based devices, resulting in PCE values up to 6%.

The substantially higher V_{OC} of the fullerene-free devices results from improved energy level alignment between the frontier molecular orbitals at the donor-acceptor interface. As demonstrated in the previous section, the V_{OC} of organic heterojunction devices is primarily determined by the interface gap E_{DA}.[79] A LUMO energy of -2.9 eV for SubPc and -3.1 eV for SubNc were measured by IPES. With the HOMO of α-6T around -5.0 eV,[31] an interface gap of about 2.1 eV and 1.9 eV exists for the α-6T/SubPc and α-6T/SubNc heterojunctions, respectively. In contrast, the interface gap of the α-6T/C_{60} heterojunction is estimated at only 1.1 eV. As these interface energy gaps are likely correlated with the CT state energy, a large part of the excitation energy is lost in CT state formation at the fullerene interface. The high V_{OC} values for the fullerene-free devices are hence a consequence of reduced energetic losses upon CT state formation compared with the fullerene-based devices. Likewise, the lower HOMO energy of Tc explains the further increase in V_{OC} for the Tc/SubPc and Tc/SubNc devices.

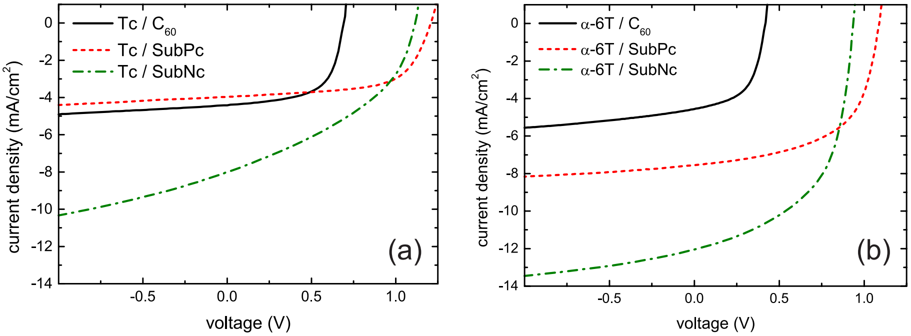

Figure 3.9: Compared with the C_{60} acceptor, non-fullerene acceptors SubPc and SubNc increase the V_{OC} and J_{SC} of bilayer devices with (a) Tc and (b) α-6T as donor.

Table 3.3: Solar cell performance parameters, measured under 100 mW/cm^2 AM1.5G illumination, for fullerene-free bilayer devices with a Tc or α-6T donor, compared with the respective C_{60}-based devices.

Device structure	V_{OC} **(V)**	J_{SC} **(mA/cm^2)**	**FF (%)**	**PCE (%)**
Tc (60 nm)/C_{60} (30 nm)/BCP (10 nm)	0.70	4.47	61.3	1.92
MoO_3 (5 nm)/Tc (60 nm)/SubPc (30 nm)/BCP (10 nm)	1.20	4.01	64.9	3.12
MoO_3 (5 nm)/Tc (60 nm)/SubNc (30 nm)/BCP (10 nm)	1.12	7.88	40.0	3.53
α-6T (60 nm)/C_{60} (20 nm)/BCP (15 nm)	0.42	4.56	54.6	1.03
α-6T (60 nm)/SubPc (15 nm)/BCP (5 nm)	1.09	7.46	57.9	4.69
α-6T (60 nm)/SubNc (20 nm)/BCP (15 nm)	0.94	12.04	53.9	6.02

The high photocurrent generation in the fullerene-free devices is in the first place attributed to the strong absorption of visible light by SubPc and SubNc. Both materials have an absorption coefficient of 3.5×10^5 cm^{-1} at their peak wavelength. Furthermore, the absorption spectra of these materials complement the Tc and α-6T donors (**Figure 3.11**). External quantum efficiency measurements reveal the relative contributions of the donor and acceptor materials to the photocurrent generation.

Although the absorption spectra of Tc and C_{60} partially overlap, both materials clearly contribute to the photocurrent generation in the Tc/C_{60} device. The three peaks in the EQE spectrum at wavelengths of 445 nm, 475 nm and 505 nm indicate the contribution of Tc absorption to the photocurrent, while the small tail extending to 650 nm can only arise from absorption by C_{60} (**Figure 3.11(a)**). In contrast, for devices with a SubPc or SubNc acceptor the Tc signal in both EQE spectra is severely reduced. A possible explanation for this lack of photocurrent generation by the Tc donor is the formation of triplet excitons by rapid singlet exciton fission:[38,186] the spontaneous conversion of a singlet exciton into two triplets. The triplet excitons have a smaller energy and cannot dissociate at the interface with the non-fullerene acceptors due to the higher CT state energy at these heterojunctions. As a consequence, most excitons generated in the Tc layer do not lead to charge generation in the fullerene-free devices. Nevertheless, the strong absorption in the SubPc and SubNc acceptor layers still results in high photocurrent generation. Also for α-6T/C_{60} based devices the spectral features of the donor absorption are recognized in the EQE spectrum (**Figure 3.11(b)**). However, since no fast triplet formation is expected for α-6T, the photocurrent contribution from the donor remains high in the fullerene-free devices. The IQE was estimated by dividing the EQE spectrum by the absorptance (derived from reflectance measurements, including parasitic absorption, and thus serving as a lower bound for IQE). For the α-6T-based devices, high IQE values of 70% for the SubPc acceptor and 85% for the SubNc acceptor are obtained. This is facilitated by the high surface roughness of the underlying α-6T donor layer, with RMS roughness of 15.9 nm and a 37% increase in surface area compared with the projected area (**Figure 3.10(b)**). Most excitons generated in the acceptor layer can therefore easily reach the donor-acceptor interface and dissociate, resulting in high IQE values.

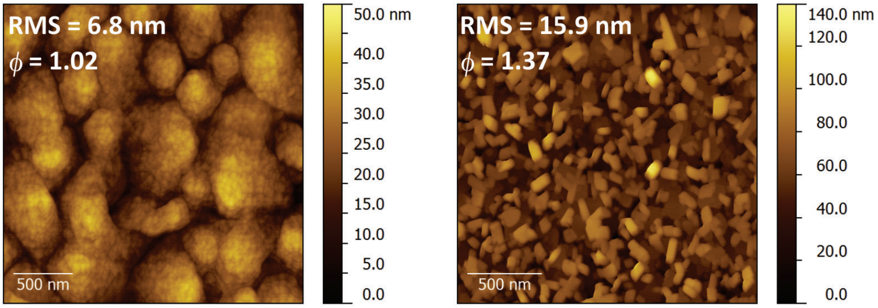

(a) Tc (60 nm) (b) α-6T (70 nm)

Figure 3.10: Atomic force microscopy images of (a) 60-nm Tc and (b) 70-nm α-6T films deposited on Si/SiO_2 substrates spin-coated with PEDOT:PSS. The surface RMS roughness and folding ratio (ϕ) are indicated in the inset of each image.

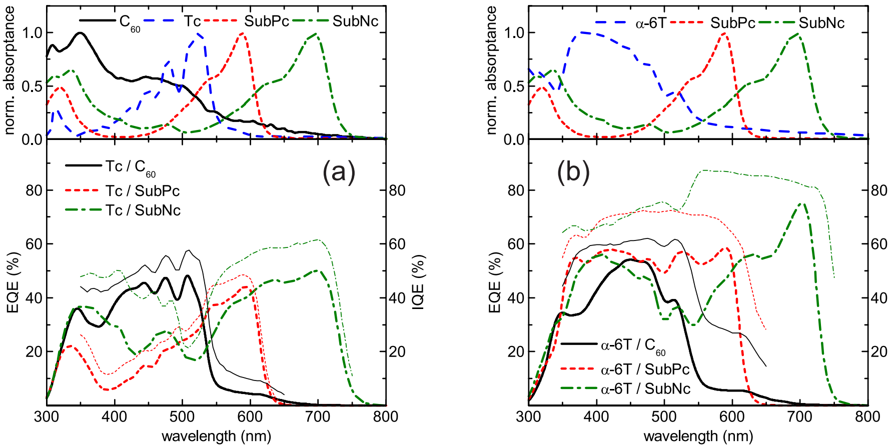

Figure 3.11: External (thick lines) and internal quantum efficiency (thin lines) of bilayer devices with (a) Tc and (b) α-6T as donor. The absorption spectra (top panel) of the non–fullerene acceptors complement both donor materials, enabling a broad absorption of visible light.

The devices employing a SubNc acceptor show a strong decrease in FF when the thickness of the SubNc acceptor layer is increased, an aspect that can often be attributed to difficult extraction of the generated charges. Despite the low electron mobility of the SubNc acceptor, no increase in series resistance was observed in the dark *J-V* curves of bilayer devices with thick SubNc layers. This observation indicates that the low FF in these devices is not related to a limited charge extraction through the acceptor layer. The decrease in FF is rather related to a voltage-dependent photocurrent in the fourth quadrant of the *J-V* curve. Similar observations were made for devices employing SubNc as donor material, attributing the low FF to a strong voltage dependence of the charge transfer processes at the donor-acceptor interface.[162] Comparable effects thus seem to play a role when SubNc is used as acceptor. In devices with a SubPc acceptor this effect is absent, and the FF does not significantly decrease for SubPc thicknesses below 20 nm.

3.4 Chapter highlights

- By altering the peripheral substituents, the electron affinity of SubPc molecules is varied over 0.3 eV without changing their absorption. Incorporation of these non-fullerene acceptors in OPV devices enables easy tuning of the heterojunction energetics.

- In a systematic study the performance of planar-heterojunction devices is correlated with their heterojunction energetics. Due to a trade-off between V_{OC} and photocurrent, optimization of the interface energy gap is necessary to achieve maximal efficiencies. The highest PCE is obtained for the combination of a SubNc donor and a Cl_6-SubPc-Cl acceptor. The device performance is further improved by inserting an exciton-blocking DIP layer at the anode, resulting in a planar-heterojunction OPV device with an efficiency of 6.9% and a V_{OC} above 1 V. Moreover, it is shown that non-fullerene acceptors require adjusted electron transport layers with aligned energy levels to enable efficient electron extraction.

- Also non-substituted subphthalocyanines are demonstrated to function as effective electron acceptors. In discrete-heterojunction devices with an α-6T donor PCE values of 4.7% and 6% are obtained with respectively SubPc or SubNc as acceptor, both exceeding the C_{60}-based counterpart. The combination of strong absorption in the non-fullerene acceptors and a large donor-acceptor interface area results in high quantum efficiencies. Additionally, high V_{OC} values are realized due to the enhanced energy level alignment between donor and acceptor.

4. Cascade architectures

In the previous chapter, the use of non-fullerene acceptors resulted in enhanced light absorption in the visible range of the solar spectrum, resulting in an increased photocurrent generation. The main performance improvement however stems from the ability to achieve significantly higher V_{OC} compared with fullerene acceptors. To further increase the power conversion efficiency of organic solar cells, their absorption spectrum should be broadened while maintaining a high photovoltage and efficient exciton harvesting. This is often accomplished using tandem device architectures, which incorporate two or more complementary-absorbing subcells in a multijunction structure.[46,93,94] Insertion of an interconnecting recombination layer allows electrons and holes from adjacent subcells to recombine. Due to this serial connection the open-circuit voltages of the subcells are added, and the tandem device can supply a high photovoltage.[187] Contrarily, the short-circuit current is limited by the lowest-photocurrent-producing subcell. Hence, careful optimization of optical interference effects is necessary to achieve optimal performance in tandem structures. Despite their complex device structure, small-molecule and polymer tandem solar cells with efficiencies above 10% have been realized.[86,87] An alternative approach to enhance absorption in organic solar cells is the incorporation of multiple absorbers in bulk heterojunctions to create ternary or quaternary blends.[188–190] The presence of additional absorbers can increase photocurrent generation by parallel or cascaded charge transfer pathways,[191,192] or by exploiting intermolecular exciton energy transfer.[193] Such multicomponent blends avoid the complexity of tandem architectures, but also create other concerns related to phase separation, energy level alignment and charge transport.

In this chapter, two multilayer cascade architectures with discrete heterojunctions are investigated, with the purpose to broaden the absorption spectrum and increase the photocurrent generation in organic solar cells. **Section 4.1** describes a *charge transfer cascade* device in which the cascade-energy-level alignment of three active layers create two charge-generating heterojunctions (**Figure 4.1(a)**). Next, in **Section 4.2**, interlayer exciton energy transfer is exploited to enable a two-step exciton dissociation process in *energy transfer cascade* devices. In this device architecture, excitons generated in a remote wide-bandgap absorber first transfer to a smaller-bandgap material by a long-range exciton transfer mechanism, and subsequently dissociate at the donor-acceptor interface (**Figure 4.1(b)**). Finally, the best-performing energy transfer cascade device is evaluated for application-relevant conditions in **Section 4.3**, and the assets of the presented multilayer cascade devices are compared with tandem architectures in **Section 4.4**.

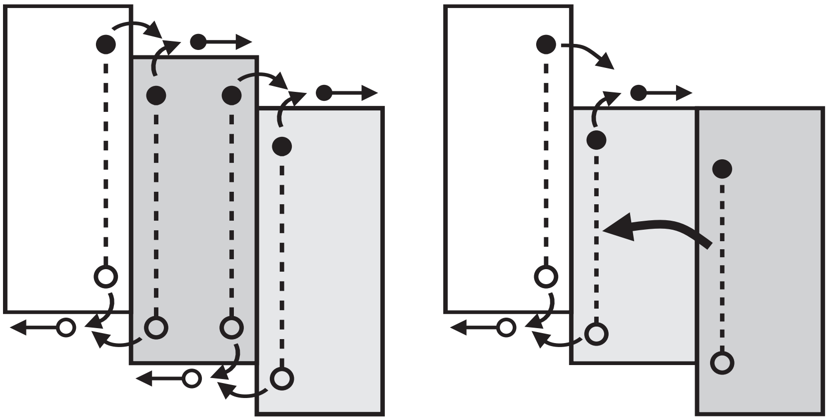

(a)
Charge Transfer Cascade

(b)
Energy Transfer Cascade

Figure 4.1: Schematic illustration of the active layer energy levels and operation principle of cascade organic solar cells.

4.1 Charge transfer cascade

In a charge transfer cascade organic solar cell an ambipolar layer is inserted at the donor-acceptor interface in a planar-heterojunction device, enabling charge generation at multiple active interfaces in a single cell.[115,184,194] In order to ensure efficient exciton dissociation and charge transport to the electrodes, the HOMO and LUMO energy levels of the interfacial layer must be intermediate to those of the donor and the acceptor, creating a cascade energy band structure (**Figure 4.1(a)**). In such a three-layer stack with cascade-energy-level alignment, the additional absorption in the ambipolar interlayer broadens the optical bandwidth and increases the photocurrent generation in the device.[172,184] Furthermore, such cascade architectures have been reported to increase V_{OC} by reduction of interfacial recombination losses.[195,196]

In this section, SubPc is used as an interlayer between a tetracene (Tc) donor and a C_{60} acceptor. Heterojunctions with a SubPc donor and a C_{60} acceptor are known to form relatively efficient OPV devices with high V_{OC} (≈ 1.0 V).[22,174] Moreover, SubPc was demonstrated to act as acceptor in combination with a Tc donor in **Section 3.3**. In the three-layer cascade device, the Tc/SubPc and SubPc/C_{60} interfaces are therefore both able to contribute to the photocurrent, which should consequently yield an enhanced short-circuit current compared with the constituent bilayer devices. The energy level diagram of the Tc/SubPc/C_{60} charge transfer cascade is illustrated in **Figure 4.2(a)**.

Devices were fabricated on patterned ITO-coated glass substrates spin-coated with PEDOT:PSS (**Figure 4.2(b)**). After vacuum evaporation of the active layers a 10-nm BCP exciton blocking layer and a 120-nm Al top contact were deposited. The thickness of the Tc donor layer and the C_{60} acceptor layer were fixed at respectively 60 nm and 30 nm. In an effort to optimize the three-layer charge transfer cascade structure, a series of cells with varying SubPc thickness were fabricated. The *J-V* curve of the optimized three-layer device is compared with the constituent bilayer devices, Tc/SubPc and SubPc/C_{60}, and the reference Tc/C_{60} device in **Figure 4.2(c)**. The corresponding performance parameters are given in **Table 4.1**.[184]

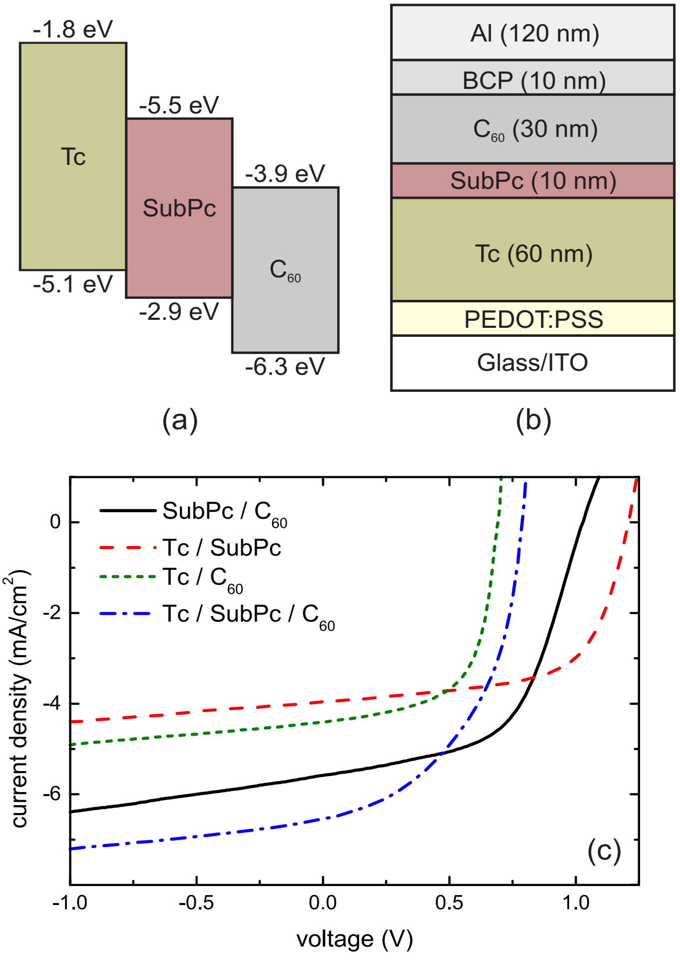

Figure 4.2: Schematic illustration of (a) the energy level diagram and (b) the device structure of the Tc/SubPc/C_{60} charge transfer cascade device. (c) Current density-voltage curves, measured under 100 mW/cm^2 AM1.5G illumination, of the optimized charge transfer cascade device compared with the constituent bilayer devices.[184]

Table 4.1: Solar cell performance parameters, measured under 100 mW/cm^2 AM1.5G illumination, of the charge transfer cascade device compared with the constituent bilayer devices.

Device structure	V_{OC} (V)	J_{SC} (mA/cm^2)	FF (%)	PCE (%)
[a] SubPc (14 nm)/C_{60} (35 nm)	1.03	5.78	55.7	3.31
MoO_3 (5 nm)/Tc (60 nm)/SubPc (30 nm)	1.20	4.01	64.9	3.12
Tc (60 nm)/C_{60} (30 nm)	0.70	4.47	61.3	1.92
Tc (60 nm)/SubPc (10 nm)/C_{60} (30 nm)	0.80	6.44	50.2	2.58

[a] This device was fabricated without PEDOT:PSS hole transport layer, and with a 150 nm thick Ag cathode.

The performance of the reference Tc/C_{60} device strongly depends on the crystallization of the Tc layer during deposition.[197] The planarizing PEDOT:PSS layer and high evaporation rate of Tc result in a relatively smooth Tc surface with RMS roughness of 6.9 nm. The AFM images in **Figure 4.3** show that the 60 nm thick Tc layer consists of several grains, 250 nm to 500 nm in size, which completely cover the underlying substrate surface. Subsequent depositions of 5 nm SubPc and 5 nm C_{60} form closed conformal layers on top of the Tc surface. This confirms that the SubPc interlayer completely covers the Tc surface in the three-layer Tc/SubPc/C_{60} device, preventing parallel heterojunctions of Tc/C_{60} and SubPc/C_{60} to introduce ambiguity to the device comparison and interpretation.

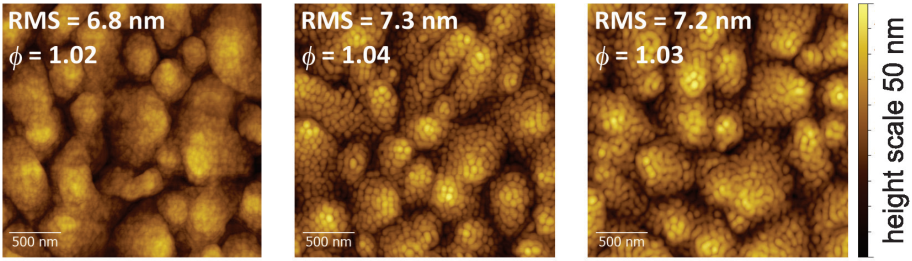

(a) 60 nm Tc (b) + 5 nm SubPc (c) + 5 nm C_{60}

Figure 4.3: Atomic force microscopy images (2.5 µm × 2.5 µm) of (a) ITO/PEDOT:PSS/Tc (60 nm); (b) ITO/PEDOT:PSS/Tc (60 nm)/SubPc (5 nm); and (c) ITO/PEDOT:PSS/Tc (60 nm)/SubPc (10 nm)/C_{60} (5 nm). The surface RMS roughness and folding ratio (ϕ) are indicated in the inset of each panel.[184]

The Tc/C_{60} reference device, without a SubPc interlayer, has a PCE of 1.92%. The addition of a 10 nm thick SubPc interlayer increases J_{SC} to 6.44 mA/cm^2, representing a 12% increase over the SubPc/C_{60} device, which is the next-highest-photocurrent-producing donor-acceptor interface. Furthermore, V_{OC} is increased to 0.80 V compared with 0.70 V for the Tc/C_{60} cell. Unfortunately, the FF is reduced below 50% in the three-layer device structure, which limits the PCE to 2.58%.

To examine the origin of the increased photocurrent in the three-layer cascade structure, the EQE spectrum is compared with the constituent bilayer devices (**Figure 4.4**). In order to disentangle the contributions of the three active layers, the absorption spectra of Tc, SubPc and C_{60} films are added in **Figure 4.4(a)**. Three absorption peaks of Tc at wavelengths of 445 nm, 475 nm and 505 nm are clearly visible in the EQE curve of the Tc/SubPc/C_{60} cell. The prominent EQE peak at 590 nm, reaching a value of almost 70%, corresponds to SubPc absorption. The photocurrent signal of C_{60} is mostly convoluted with the Tc signal, except for the small tail at wavelengths exceeding 625 nm, which can only originate from C_{60} absorption. The observation that all three active layers contribute to the photocurrent supports the suggested device operation mechanism, illustrated in **Figure 4.1(a)**. The Tc/SubPc and SubPc/C_{60} interfaces are both photoactive and the SubPc interlayer functions simultaneously as an acceptor for Tc and as a donor for C_{60}. Excitons generated in the SubPc layer itself can diffuse towards either interface, and dissociate. This results in an EQE value close to 70% for the peak absorption wavelength of SubPc, a value that is not observed for SubPc/C_{60} devices. Although the heterojunctions are mechanically stacked in series, they operate electrically in parallel; i.e. the total photocurrent produced in the cascade device is the addition of the photocurrent generated at each heterojunction. Free electrons generated at the Tc/SubPc interface travel through the SubPc interlayer to the C_{60} layer, while holes travel in the other direction: from the SubPc/C_{60} interface, via SubPc, towards the Tc donor layer.

Due to the high photocurrent contribution of the SubPc interlayer in the three-layer cascade device, the total photocurrent generation is higher compared with the constituent bilayer devices. However, for wavelengths below 480 nm the EQE of the cascade device is reduced compared with the reference Tc/C_{60} device without SubPc interlayer. In this wavelength region Tc and C_{60} both absorb, while SubPc absorption is negligible. The reduction of the Tc signal is also observed in the bilayer Tc/SubPc device and could be related to rapid singlet exciton fission for excitons generated in Tc (see **Section 3.3**).[38,186] However, the C_{60} contribution to the photocurrent is also reduced (around 400 nm C_{60} is the main absorber). After exclusion of optical interference effects via reflection measurements, two possible explanations for this drop in quantum efficiency remain: (1) less efficient exciton dissociation at the interface with the SubPc interlayer for Tc excitons as well as C_{60} excitons, and (2) bimolecular recombination of free charges in the bulk of the SubPc interlayer.

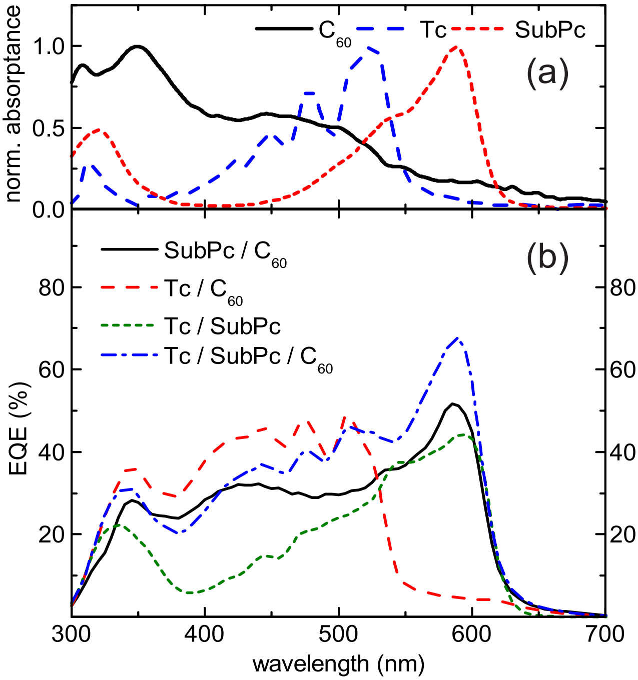

Figure 4.4: (a) Normalized absorption spectra of thin films of C_{60}, Tc, and SubPc, and (b) EQE spectra of the Tc/SubPc/C_{60} charge transfer cascade device compared with the constituent bilayer devices.

To unravel where this loss of photocurrent occurs, the evolution of the EQE signal with SubPc thickness was examined at specified wavelengths of 400 nm, 475 nm and 590 nm, representing the primary photocurrent contributions of respectively C_{60}, Tc, and SubPc (**Figure 4.5(a)**). The EQE at 590 nm increases as a result of increasing absorption in a thicker SubPc layer. The EQE signal at 475 nm, corresponding to the Tc contribution, shows an initial drop of almost 10%, but the EQE reduction slows down at higher SubPc thickness. The C_{60} contribution at 400 nm shows a similar trend. The initial 10% drop is likely due to a reduced exciton dissociation rate at the interface with SubPc, compared with the Tc/C_{60} interface. A 5 nm thick SubPc layer completely covers the Tc surface and hence decreases the contribution of both Tc and C_{60} to the photocurrent. The small decrease at higher SubPc thickness is mainly a consequence of optical effects, as confirmed by reflection measurements. If bulk recombination of free charge carriers was prevailing, a larger decrease of the overall EQE signal at high SubPc thickness would be expected. As a result, the J_{SC} of the cascade cell is highest for thick SubPc interlayers (**Figure 4.5(b)**). The initial increase of J_{SC} with SubPc thickness is related to the additional absorption in the strongly absorbing SubPc layer. The maximal J_{SC} value of 6.51 mA/cm^2 is reached at 12 nm SubPc, beyond which J_{SC} slightly decreases again due to the reduced contribution of Tc and C_{60}.

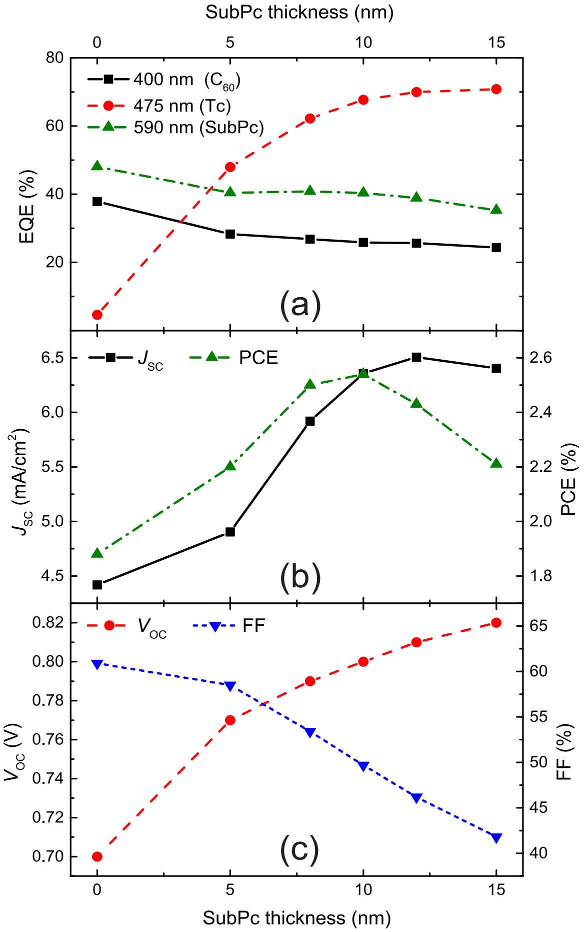

Figure 4.5: Dependence of (a) the EQE signal at wavelengths of 400 nm, 475 nm, and 590 nm - representing the photocurrent contribution of respectively C_{60}, Tc, and SubPc - and (b)-(c) the solar cell performance parameters on SubPc interlayer thickness in the Tc/SubPc/C_{60} charge transfer cascade device.[184]

Also the V_{OC} increases with SubPc interlayer thickness, from 0.70 V for the reference Tc/C_{60} device to 0.82 V in the three-layer charge transfer cascade with a 15 nm thick interlayer (**Figure 4.5(c)**). According to the general diode equation for organic heterojunctions (**equation (1.2)**), the V_{OC} is determined by the interface energy gap and the recombination of free charge carriers at this interface.[74] In the three-layer charge transfer cascade, recombination can occur at both active heterojunctions, because both electrons and holes are present in the ambipolar interlayer. In this case, the V_{OC} is limited by the HOMO of the donor and the LUMO of the acceptor. Insertion of a 5 nm SubPc interlayer blocks recombination of electrons in C_{60}

with holes in Tc, and consequently reduces the forward dark current (**Figure 4.6**). This recombination current further decreases with increasing SubPc thickness. Similar to bilayer heterojunctions, increasing layer thickness reduces the internal electric field and shifts the onset of forward dark current to higher applied voltages. The saturation current density ($J_{0,n}$), fitted from the J-V measurements in dark, hence decreases from 2.23 nA/cm^2 for the Tc/C$_{60}$ bilayer to 0.06 nA/cm^2 for the three-layer device with a 15-nm SubPc interlayer. This decrease of $J_{0,n}$ corresponds to the observed increase of V_{OC} under illumination, according to **equation (1.4)**. A similar V_{OC} increase and reduced recombination losses were reported in other cascade structures by Heidel et al.[195] Nevertheless, due to the cascade-energy-level alignment, the V_{OC} of the three-layer charge transfer cascade remains far below the V_{OC} of the constituent bilayer devices Tc/SubPc and SubPc/C$_{60}$.

In contrast to V_{OC}, the FF is negatively affected by the insertion of the SubPc interlayer: the 61% FF for the Tc/C$_{60}$ bilayer device decreases to 42% upon addition of 15 nm SubPc (**Figure 4.5(c)**). This FF decrease results from a reduced photocurrent in the fourth quadrant of the J-V curves, possibly related to a voltage-dependent charge transfer process at the active heterojunctions. An increase of the SubPc thickness decreases the internal electric field at these heterojunctions, which can reduce the dissociation rate. Another effect that can cause low FF is related to the charge extraction in devices with an energy-level-cascade structure. The donor and acceptor layer form injection barriers with respect to the ambipolar interlayer. Such injection barriers are known to cause charge buildup and field inversion in planar-heterojunction devices, resulting in S-kinks in the J-V curve.[71] The charge transfer cascade architecture was extensively studied by Barito et al., using a wide range of transparent donor materials and either SubNc or SubPc as interlayer.[115] This study indicated field inversion as the main reason for the low FF of these devices. However, since the photocurrent generation at the donor-interlayer interface is limited in these devices, the charge distribution in the device can considerably differ from the Tc-based device, and numerical drift-diffusion simulations are needed to clarify the effect of charge transfer and charge transport on the FF and V_{OC} of such multilayer charge transfer cascade devices.

In summary, the evolution of J_{SC}, V_{OC} and FF results in an optimal SubPc interlayer thickness of 10 nm, maximizing the efficiency of the charge transfer cascade device at 2.54%. With respect to the Tc/C$_{60}$ device, insertion of the ambipolar interlayer indeed increases photocurrent generation and device efficiency. However, the three-layer cascade device does not exceed the efficiency of the Tc/SubPc and SubPc/C$_{60}$ bilayer devices. The enhanced photocurrent does not compensate the losses in V_{OC} and FF. Although the FF loss might be avoided, the V_{OC} loss is intrinsic to the cascade-energy-level alignment of the device structure. As a result, the selection of appropriate material combinations is crucial to further improve the efficiency of charge transfer cascade devices.

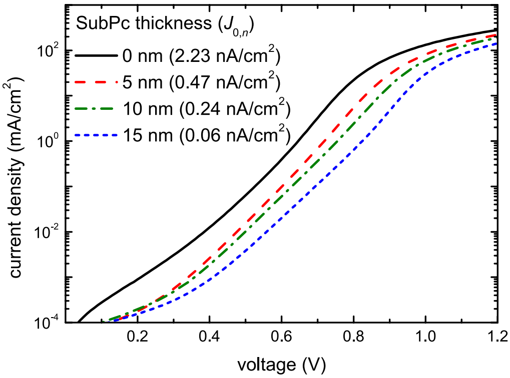

Figure 4.6: Dark *J*-*V* curves, measured in forward bias, for different SubPc interlayer thicknesses in the three-layer charge transfer cascade device. The saturation current density ($J_{0,n}$) is extracted by fitting the curves with the generalized diode equation.

4.2 Energy transfer cascade

An energy transfer cascade organic solar cell relies on interlayer exciton transfer to harvest excitons from multiple absorbing layers (**Figure 4.1(b)**).[185,198-200] Two mechanisms are known to enable efficient intermolecular transfer of exciton energy. Dexter energy transfer is the direct exchange of electrons between neighboring molecules.[51] As this mechanism requires the overlap of molecular orbitals, excitons can only be transferred over short distances, typically below 1 nm. On the other hand, Förster energy transfer enables exciton transfer over longer distances due to a non-radiative dipole-dipole coupling between two chromophores.[50] This mechanism is also known as fluorescence resonance energy transfer or FRET. Although it's a non-radiative process, exciton transfer by FRET requires that the emission spectrum of the donor molecule overlaps with the absorption spectrum of the acceptor molecule. Because excitons can be transferred over tens of nanometers, the FRET mechanism enables efficient exciton harvesting from multiple absorbing layers in a single-junction device structure.

This section describes the development of energy transfer cascade devices based on exciton energy transfer from SubPc to SubNc. First, the intermolecular FRET efficiency is investigated by photoluminescence quenching experiments. Next, the SubPc/SubNc energy relay system is incorporated in multilayer devices, both at the donor and acceptor side of the active heterojunction.

4.2.1 Exciton energy transfer from SubPc to SubNc

The Förster transfer rate (k_f) for transitions between an energy donor and an energy acceptor is:

$$k_\mathrm{f} = \frac{1}{\tau} \cdot \left(\frac{R_0}{r}\right)^6 \tag{4.1}$$

where τ is the natural exciton lifetime on the energy donor, and r the separation distance between the dipoles.[50] The Förster radius R_0 indicates the distance at which half of the excitons are transferred by Förster energy transfer before they decay through other radiative or non-radiative mechanisms. This Förster radius is related to the spectral overlap of the donor emission $(F_\mathrm{D}(\lambda))$ and acceptor absorption cross-section $(\sigma_\mathrm{A}(\lambda))$:

$$R_0^6 = \frac{9\,\eta_\mathrm{PL} \cdot \kappa^2}{128\,\pi^5 \cdot n^4} \int \lambda^4 \cdot F_\mathrm{D}(\lambda) \cdot \sigma_\mathrm{A}(\lambda)\,\mathrm{d}\lambda \tag{4.2}$$

with η_PL the photoluminescence (PL) quantum yield of the energy donor, κ the dipole orientation factor (approximately $\sqrt{2/3}$ for randomly oriented dipoles), n the refractive index, and λ the wavelength. A Förster radius of 1 nm to 5 nm is typically obtained for small-molecule organic semiconductors.[201]

Due to the r^{-6} dependence of k_f the exciton energy transfer through FRET seems limited to nanometer-scale distances. However, in planar-heterojunction structures the energy transfer is significantly enhanced because an excited energy donor molecule can transfer its energy to any molecule in the energy acceptor layer. It has been shown that the energy transfer rate follows a r^{-3} dependence in case of thick quenching films. The Förster transfer rate can be modified for exciton transfer from an emissive donor molecule to a layer of acceptor molecules with the molecular density ρ_A:[202]

$$k_\mathrm{f} = \frac{\rho_\mathrm{A}}{\tau} \cdot \frac{\pi\,R_0^6}{6\,d^3} \tag{4.3}$$

where d is the distance of the emitting molecule normal to the energy acceptor layer.

Due to its strong PL signal SubPc is a good candidate as the energy donor material in an energy relay cascade. The extended conjugated ring structure in SubNc causes a bathochromic shift of the molecular absorption. As a result, the absorption spectrum of SubNc largely overlaps with the emission spectrum of SubPc (**Figure 4.7**). These molecular homologues thus fulfill the requirements for efficient Förster energy transfer. Hence, the interlayer energy transfer efficiency between thin films of SubPc and SubNc is experimentally examined in the following paragraphs.[185]

According to the work of Luhman and Holmes,[201] the Förster transfer rate between organic semiconducting layers can be quantified by a combination of PL quenching experiments and numerical exciton density simulations. A three-layer structure is used to spatially separate the energy donor from the energy acceptor. An inserted

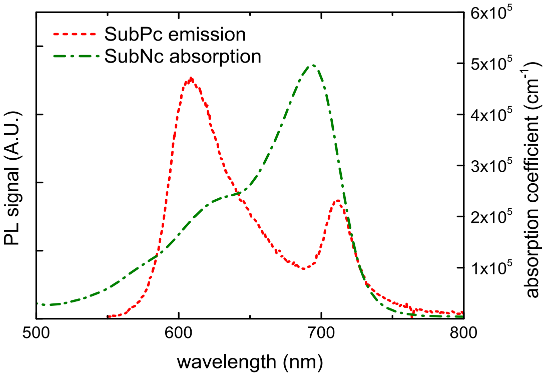

Figure 4.7: The emission spectrum of SubPc largely overlaps with the absorption spectrum of SubNc.

wide-bandgap spacer layer suppresses exciton quenching by direct charge transfer at the interface, while long-range energy transfer across the transparent spacer layer is still possible. The interlayer energy transfer efficiency is then evaluated from the PL quenching for different spacer thicknesses. Finally, by fitting the experimental results, using exciton density simulations, the Förster radius R_0 can be calculated.

Here, quartz substrates were coated with a 20 nm thick SubPc layer and a 10 nm thick SubNc quenching layer, separated by a 4,4'-bis(N-carbazolyl)-1,1'-biphenyl (CBP) spacer layer with varying thickness. Samples with C_{60} as quenching layer were used as control structures, because negligible energy transfer is expected due to the limited overlap of C_{60} absorption and SubPc emission. The PL intensity of these samples is calculated by integrating the measured emission spectra (**Figure 4.8**). For each CBP thickness, the PL ratio is then obtained as the ratio of the PL intensity for a sample with quenching layer and a reference sample without quenching layer. The emission spectrum of SubPc consists of two distinct peaks centered at 620 nm and 710 nm.[203] Because these peaks show different quenching behavior, the PL ratios were only calculated for the peak at 710 nm. As this peak partially overlaps with emission of SubNc, the measured PL signal was first deconvoluted using a peak-fitting algorithm. After subtraction of the background signal of the peak at lower wavelength, the measured PL signal was fitted with two Gaussian-shaped curves centered around the wavelength of maximum emission of SubPc and SubNc thin films, at 710 nm and 720 nm respectively. The PL intensity was obtained by integrating the fitted curve corresponding to SubPc emission between 685 nm and 745 nm. This method was used to analyze all organic layer stacks containing a SubNc quenching layer. For control samples with a C_{60} quenching layer or reference samples without quenching layer, a single Gaussian curve was used to fit the experimental PL signal and calculate the integrated intensity. Errors for the PL intensities and PL ratios mainly result from the root-mean-square difference between the experimental data and the analytical model resulting from the peak-fitting algorithm.

The obtained PL ratios reveal that SubNc quenches the SubPc PL signal substantially compared with a C_{60} quenching layer (**Figure 4.8(d)**). This indicates that FRET from SubPc to SubNc is very efficient and long-range interlayer exciton transfer is possible. In fact, the PL signal is still effectively quenched by SubNc when CBP spacer layers up to 35 nm are inserted.

Assuming the PL intensity is directly proportional to the exciton density $n(x)$ in the emissive donor layer, numerically simulated exciton density profiles are used to fit the experimental PL ratios. Simulated exciton density profiles are obtained by solving the steady-state one-dimensional exciton diffusion equation, modified to incorporate interlayer energy transfer:[202]

$$D\frac{\mathrm{d}^2 n(x)}{\mathrm{d}x^2} - \frac{n(x)}{\tau} + Q(x) - n(x)\cdot k_{\mathrm{f}}(d) = 0 \qquad (4.4)$$

where D is the exciton diffusion coefficient, and $k_{\mathrm{f}}(d)$ is given by **equation (4.3)**. Here, the molecular separation distance d depends on the position x in the emissive layer. A value of 1.5 nm^{-3} is used for the molecular density of the energy acceptor ρ_{A}. The exciton generation rate $Q(x)$ is taken from the optical absorption profile calculated from a transfer matrix method,[48] using optical constants measured by spectroscopic ellipsometry.

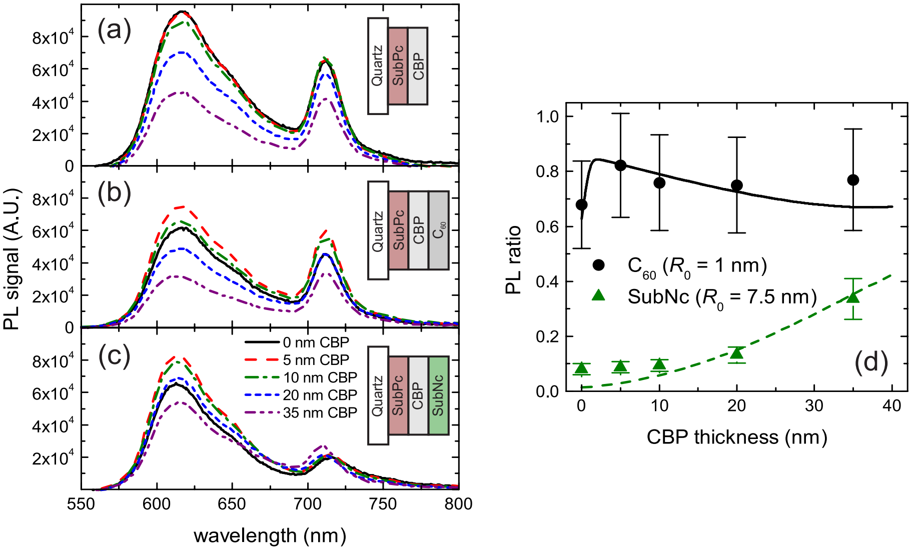

Figure 4.8: Emission spectra of organic layer stacks with varying spacer layer thicknesses (t_{S}): (a) SubPc (20 nm)/CBP (t_{S} nm), (b) SubPc (20 nm)/CBP (t_{S} nm)/C_{60} (10 nm), and (c) SubPc (20 nm)/CBP (t_{S} nm)/SubNc (10 nm). (d) The obtained PL ratios indicate effective quenching of the SubPc PL signal by energy transfer to the SubNc quenching layer. The Förster radius of energy transfer R_0 is extracted by fitting the PL ratios using numerical exciton density simulations (solid and dashed lines).[185]

Using a least-mean-squares fitting algorithm, numerical solutions of **equation (4.4)** are used to fit experimental PL data with either the SubPc exciton diffusion length ($L_D = \sqrt{D\tau}$) or the Förster energy transfer radius (R_0) as fitting parameter. First, the SubPc exciton diffusion length is extracted from thickness-dependent PL quenching experiments, using a C_{60} quenching layer (**Figure 4.9**). Assuming energy transfer from SubPc to C_{60} is negligible, an exciton diffusion length of 6 nm is obtained. This value is subsequently used in simulations for organic layer stacks including a spacer layer, where R_0 is used as fitting parameter. The CBP spacer layer and the quartz substrate were both assumed to form non-quenching interfaces. The simulation results nicely fit the experimental PL ratios, considering the slight deviation at low spacer layer thickness is likely caused by an underestimation of the SubNc contribution to the measured PL signal. A value of 7.5 nm for R_0 is extracted for exciton energy transfer from SubPc to SubNc, while no significant energy transfer is observed with a C_{60} quenching layer ($R_0 < 1$ nm). Even though more measurement points at small spacer thicknesses are necessary to determine R_0 more accurately, the small R_0 extracted with C_{60} as quenching layer confirms the negligible influence of energy transfer in this system. On the contrary, energy transfer to a SubNc quenching layer is so efficient that fits for R_0 are relatively insensitive to the values of L_D and ρ_A.

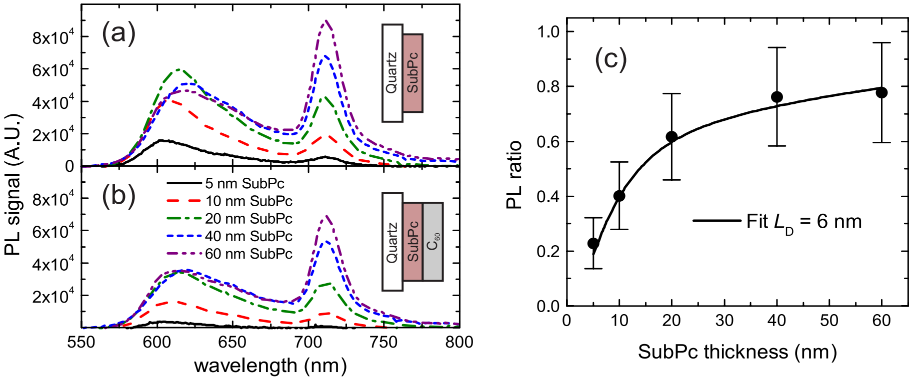

Figure 4.9: Thickness-dependent PL spectra for SubPc layers deposited on quartz substrates: (a) non-quenched spectra, and (b) quenched spectra using an additional 10-nm C_{60} quenching layer. (c) The SubPc exciton diffusion length (L_D) is extracted by fitting the experimental PL ratios using numerical exciton density simulations (solid line).

The efficient exciton energy transfer from SubPc to SubNc is mainly a consequence of their complementary optical properties: there is a good spectral overlap between the emission of SubPc and the absorption of SubNc. In general, the Stokes shift of the energy donor should match the difference between the optical bandgap of the energy donor and the energy acceptor. However, when such an energy relay system is used to enhance photocurrent of a photovoltaic device, this Stokes shift should not be too large as this corresponds to the energy loss accompanying the interlayer energy transfer process. Besides these requirements, other material properties that determine the FRET efficiency were not considered for the SubPc/SubNc energy relay system. For example, the molecular orientation in the amorphous SubPc and SubNc layers is assumed to be isotropic, and the transition dipole moments are not aligned for the energy transfer process. Therefore, control of the molecular orientation, for instance by introducing templating layers, could be considered in the search for alternative material systems with an efficient interlayer exciton energy transfer process.

4.2.2 Energy cascade devices

Previous reports have studied energy relay cascades on the donor side of OPV devices, mostly using various combinations of phthalocyanine-, tetracene-, and perylene-derivatives.[199,204–206] Also in polymer solar cells the use of FRET has been studied by addition of a squaraine dye to the blend.[193] The advantage of these device architectures over charge transfer cascades is that a broad part of the solar spectrum can be covered by combining materials with complementary optical properties, while a decrease in V_{OC} and FF can be avoided by aligning the HOMO energy levels of the multiple donor materials. However, most reports have not fully exploited these advantages, resulting in minimal efficiency enhancement in energy cascade OPV devices.

Here, a SubPc/SubNc bilayer is exploited to enhance exciton harvesting in organic photovoltaic devices. This energy relay cascade system can be used at both the donor and acceptor side of the active heterojunction. First, C_{60} will be employed as acceptor in a *donor cascade* device (**Figure 4.10(a)**). Next, α-6T will function as donor material in an *acceptor cascade* device (**Figure 4.10(b)**).

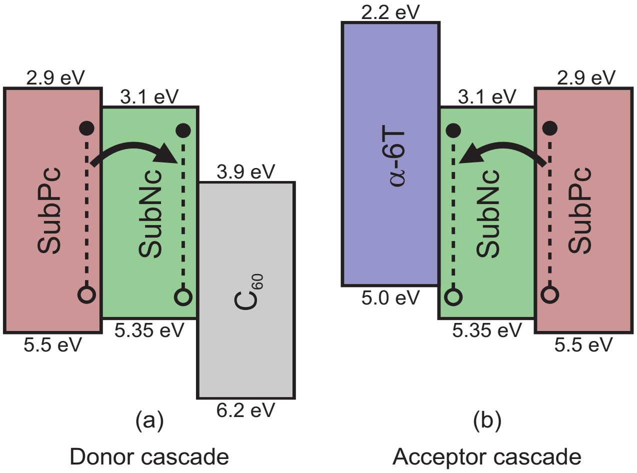

Figure 4.10: Schematic representation of the active layer energy levels of the studied (a) donor cascade and (b) acceptor cascade organic solar cells.

Donor cascade

The donor cascade device studied here consists of the SubPc/SubNc energy relay bilayer as donor, and C_{60} as acceptor. First, the layer thickness of SubNc and C_{60} was optimized in a bilayer device structure (ITO/SubNc/C_{60}/BCP/Ag), as these materials form the active heterojunction of the donor cascade device. The optimal thickness of SubNc and C_{60} were 8 nm and 40 nm, respectively, similar to reported values in the literature.[162] This reference device achieves a J_{SC} of 5.4 mA/cm^2 and a PCE of 2.5%. Insertion of a 4 nm thick SubPc layer between the ITO contact and the SubNc donor increased the J_{SC} to 8.0 mA/cm^2 (**Figure 4.11**). Although thicker SubPc layers results in higher photocurrent generation, the FF of the cascade devices severely decreases due to the formation of S-kinks in the *J*-*V* curve. The reduced FF indicates hindered extraction of free charge carriers, possibly because the small HOMO level mismatch between SubPc and SubNc creates a hole extraction barrier (**Figure 4.10(a)**). Cascade devices including a SubPc layer of 4 nm to 8 nm obtain a PCE around 4.2%. The slightly increased V_{OC} results from a reduction in the forward dark current when the SubPc layer is inserted.

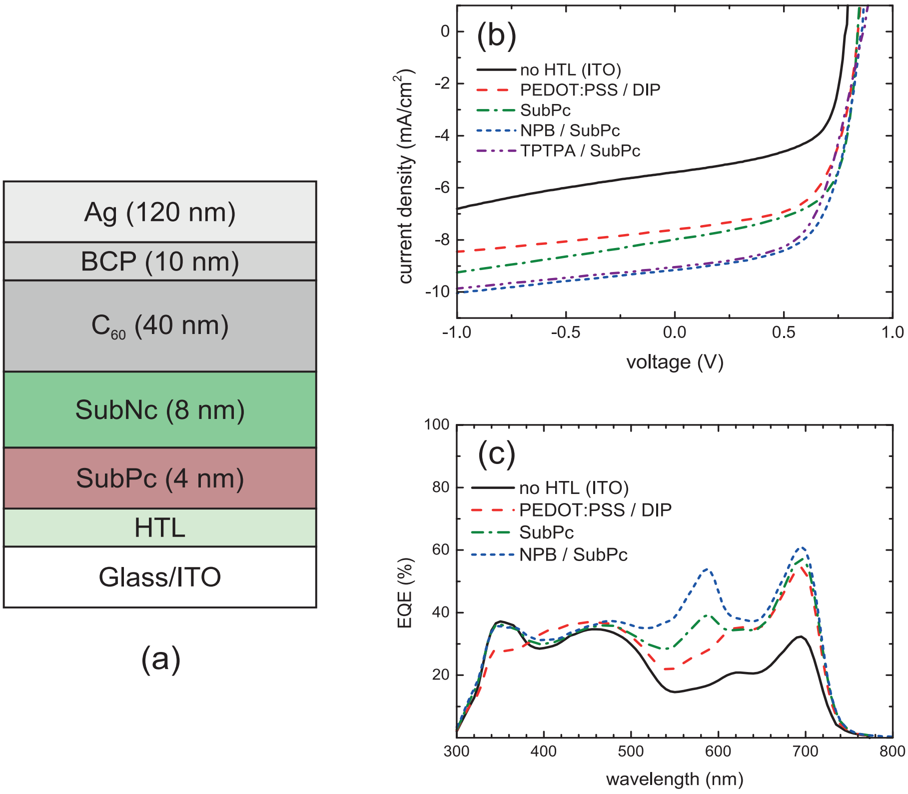

Figure 4.11: (a) Device structure, (b) *J*-*V* curves measured under 100 mW/cm^2 AM1.5G illumination, and (c) EQE spectra for devices based on a SubNc/C_{60} heterojunction with different exciton-blocking layers and/or exciton-donating SubPc layer.

Table 4.2: Solar cell performance parameters, measured under 100 mW/cm^2 AM1.5G illumination, for devices based on a SubNc/C$_{60}$ heterojunction with different exciton-blocking layers and/or exciton-donating SubPc layer.

Hole transport layer	V_{OC} (V)	J_{SC} (mA/cm^2)	FF (%)	PCE (%)
No HTL (ITO)	0.78	5.40	61.9	2.52
PEDOT:PSS/DIP (5 nm)	0.84	7.61	62.0	3.82
SubPc (4 nm)	0.84	7.99	64.1	4.16
NPB (2 nm)/SubPc (4 nm)	0.86	9.16	61.5	4.69
TPTPA (5 nm)/SubPc (4 nm)	0.87	9.04	58.2	4.42

The EQE spectrum of the donor cascade device (**Figure 4.11(c)**) clearly shows that SubPc is contributing to the photocurrent generation. This contribution results from a two-step exciton dissociation mechanism. Excitons generated in the SubPc layer are first transferred to the intermediate SubNc layer. These excitons subsequently diffuse to the C$_{60}$ interface where they finally dissociate. Due to the high Förster radius the first interlayer exciton transfer step is highly efficient, allowing SubPc to actively contribute to the photocurrent. However, the SubPc contribution only partly explains the J_{SC} increase in the cascade device. Also the SubNc contribution to the photocurrent is enhanced because the SubPc layer functions as exciton-blocking layer, similar to the DIP layer used in **Section 3.2.4**. Without SubPc or DIP layer, excitons in SubNc are quenched at the ITO interface and the IQE doesn't exceed 50%. Insertion of higher-bandgap materials such as DIP or SubPc prevents exciton quenching at the ITO interface, and increases the IQE up to 80% in the SubNc absorption region. Due to its weak absorption and emission, DIP does not contribute to the photocurrent generation, while SubPc actively contributes to the photocurrent by transferring its excitons to SubNc by FRET. The SubPc thus functions both as energy donor as well as exciton-blocking layer in the three-layer cascade device, resulting in a nearly 50% increase of the photocurrent generation.

Because SubPc excitons also are quenched by the ITO interface, the performance of the cascade device can be further improved by inserting another high-bandgap exciton-blocking layer at the anode. Thin layers of hole-transporting materials N,N'-di(1-naphthyl)-N,N'-diphenyl-(1,1'-biphenyl)-4,4'-diamine (NPB) and tris[4-(5-phenylthiophen-2-yl)phenyl]amine (TPTPA) indeed increase J_{SC} by an additional 14%, yielding PCE values up to 4.7%. The EQE spectra of these devices confirm that the additional photocurrent results from excitons generated in the SubPc layer.

A similar donor cascade architecture was studied by Menke et al.,[40] in which a SubPc:SubNc blend was used as the energy relay structure instead of a bilayer configuration. This study shows that the dilution of SubNc in the blend increases the SubNc exciton diffusion length. The SubPc excitons that are transferred to SubNc consequently diffuse more easily to the donor acceptor interface. The low SubNc concentration in the blend however results in a reduced absorption. Furthermore, the intermolecular energy transfer in this system is not necessarily directed towards the active heterojunction. The use of a blended energy relay system consequently results in lower photocurrent generation compared with the discrete SubPc/SubNc heterojunction.

The C_{60} acceptor layer in the donor cascade device can be replaced by a Cl_6-SubPc-Cl acceptor (**Figure 4.12(a)**). In bilayer devices the use of this non-fullerene acceptor resulted in higher V_{OC}, J_{SC} and FF (see **Section 3.2.5**). However, the addition of a SubPc exciton-donating layer to this device structure does not result in a significant photocurrent increase. Because SubPc and Cl_6-SubPc-Cl both absorb in the same spectral region, only a 5% increase of the photocurrent is observed compared with the device comprising an exciton-blocking DIP layer (**Figure 4.12(b)**). As a result, the PCE of the energy cascade device only marginally improves in case Cl_6-SubPc-Cl is used as acceptor.

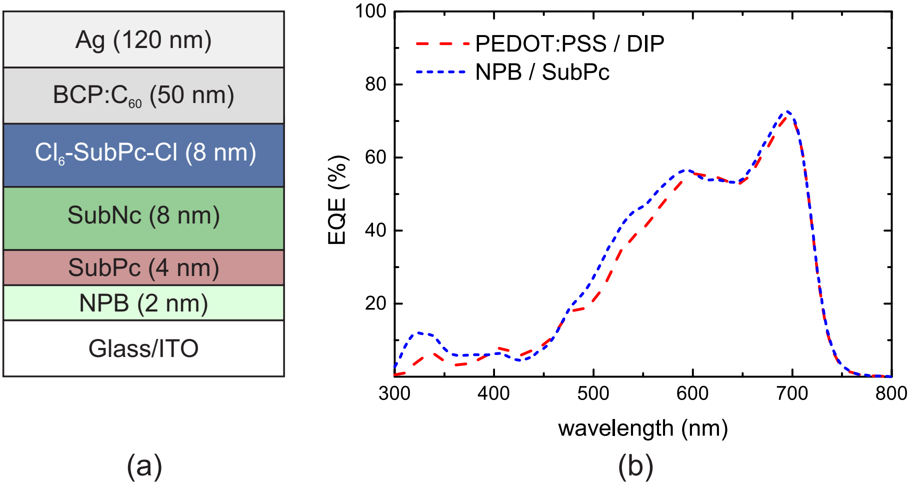

Figure 4.12: (a) Device structure, and (b) EQE spectra for devices based on a SubNc/Cl_6-SubPc-Cl heterojunction with an exciton-blocking layer (PEDOT:PSS/DIP) or an exciton-donating layer (NPB/SubPc).

Acceptor cascade

Similar to an energy relay cascade structure with multiple donor materials, SubPc and SubNc can be combined as acceptors in a three-layer device structure. An α-6T layer is selected as the electron donor, as this already resulted in high PCE values for fullerene-free bilayer devices (see **Section 3.3**).[185] The SubNc layer, positioned in the middle of the three-layer stack, can function both as electron acceptor and energy acceptor for excitons generated in α-6T and SubPc, respectively. Such a three-layer device structure was fabricated by sequentially depositing SubNc and SubPc on top of the α-6T donor layer (**Figure 4.13(a)**). The thickness of both acceptor layers and the BCP exciton-blocking layer were adjusted to optimize the *J-V* characteristics (**Figure 4.13(b)** and **Table 4.3**). The optimal thickness of the SubNc layer (12 nm) is reduced with respect to the bilayer α-6T/SubNc device. The additional SubPc layer eliminates the need for a thick SubNc layer by altering the optical interference pattern in the organic layers, ensuring strong absorption even in a thin SubNc layer. Similar to the bilayer devices, the thin SubNc layer results in a high FF (61%). Furthermore, an increase in J_{SC} is observed in the three-layer cascade device (14.6 mA/cm^2), while V_{OC} is similar to the α-6T/SubNc device (0.96 V). Because SubNc and SubPc have similar LUMO energy levels, a decrease in V_{OC} is circumvented, contrary to charge transfer cascade structure. The optimized energy cascade device obtains a PCE of 8.4%, a record efficiency for fullerene-free organic solar cells which even surpasses many state-of-the-art fullerene-based evaporated single-junction OPV devices.[207,208] For certification purposes, devices with a 1-cm^2 active area were fabricated and measured in-house with a PCE of 7.93%. This device was certified at Newport Corporation PV Lab with a PCE of 7.77% (± 0.16%) (**Figure 4.14**).

Table 4.3: Solar cell performance parameters, measured under 100 mW/cm^2 AM1.5G illumination, for the three-layer energy transfer cascade device compared with the fullerene-free bilayer devices.

Device structure	V_{OC} (V)	J_{SC} (mA/cm^2)	FF (%)	PCE (%)
α-6T (60 nm)/SubPc (15 nm)/BCP (5 nm)	1.09	7.46	57.9	4.69
α-6T (60 nm)/SubNc (20 nm)/BCP (15 nm)	0.94	12.04	53.9	6.02
α-6T (60 nm)/SubNc (12 nm)/SubPc (18 nm)/BCP (7 nm)	0.96	14.55	61.0	8.40

ACKNOWLEDGEMENT

Processing, encapsulation, and wire bonding of the 1-cm^2 devices was supported by Erwin Vandenplas, Griet Uytterhoeven, and Jef Haemhouts Moraga. Device certification was performed by Matthew O'Donnel at Newport Corporation.

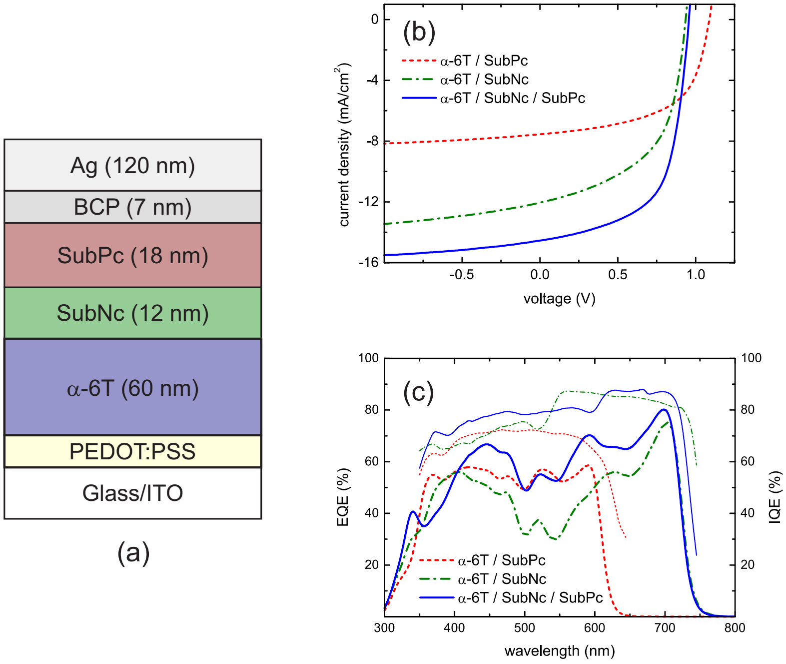

Figure 4.13: (a) Device structure, (b) *J*-*V* curves measured under 100 mW/cm^2 AM1.5G illumination, and (b) EQE (thick lines) and IQE spectra (thin lines) of the three-layer α-6T/SubNc/SubPc acceptor cascade device, compared with the α-6T/SubPc and α-6T/SubNc bilayer devices.[185]

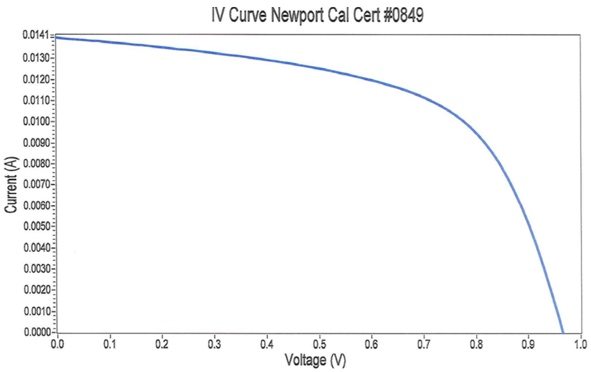

Figure 4.14: Certified current-voltage curve with PCE of 7.77% ± 0.16%, V_{OC} of 965.8 mV ± 9.6 mV, I_{SC} of 13.68 mA ± 0.25 mA, and FF of 58.6% ± 1.2%. The active area of the device was measured at 0.9970 cm^2 ± 0.0020 cm^2.

Compared with the bilayer α-6T/SubNc device, the EQE spectrum of the three-layer device shows an additional peak at 590 nm, corresponding to the absorption peak of SubPc (**Figure 4.13(c)**). This again confirms that the additional SubPc layer is actively contributing to the photocurrent, and not merely acting as an improved electron transport or exciton-blocking layer. Similar to the donor cascade device, a two-step exciton dissociation mechanism is active in the three-layer α-6T/SubNc/SubPc device, comprising exciton transfer from SubPc to SubNc, and subsequent charge transfer at the α-6T interface. The resulting IQE surpasses 75% in a broad wavelength range from 400 nm to 720 nm.

Considering the Förster radius R_0 was extracted for organic layer stacks with planar interfaces, the efficiency of the energy transfer process is expected to further increase in the acceptor cascade device structure due to the high interface roughness induced by the α-6T donor layer (**Figure 4.15**). Because the underlying α-6T layer contains several tall grains, direct contact between SubPc and α-6T might occur due to incomplete coverage of these tall grains by the intermediate SubNc layer. This would result in an additional dissociation mechanism for SubPc excitons. Due to the short exciton diffusion length, however, only the excitons in a limited volume of the SubPc layer are prone to this charge generation pathway. Exciton diffusion in SubPc is most likely based on self-Förster energy transfer, with an estimated self-Förster radius of 1.5 nm.[40] However, with the interlayer Förster radius of 7.5 nm, SubPc excitons are more likely transferred to SubNc by FRET compared with diffusion toward possible α-6T/SubPc interfaces. The suggested two-step exciton dissociation process including energy transfer is consequently the dominant charge generation mechanism.

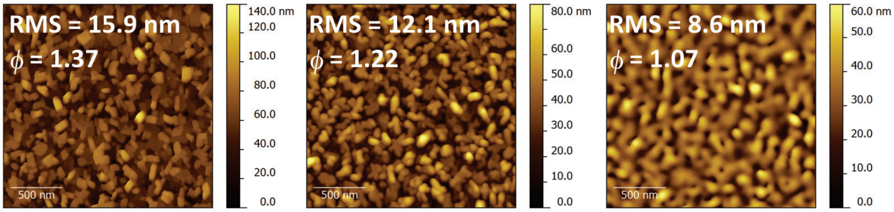

(a) 70 nm α-6T (b) + 20 nm SubNc (c) + 20 nm SubPc

Figure 4.15: Atomic force microscopy images (2 µm × 2 µm) of organic layer stacks deposited on Si/SiO$_2$ substrates spin-coated with PEDOT:PSS. (a) α-6T (70 nm), (b) α-6T (70 nm)/SubNc (20 nm), and (c) α-6T (70 nm)/SubNc (20 nm)/SubPc (20 nm). The surface RMS roughness and folding ratio (ϕ) are indicated in the inset of each panel.

ACKNOWLEDGEMENT

Photoluminescence excitation measurements were performed by Alyssa Brigeman at Pennsylvania State University. Alyssa Brigeman and Chris Giebink are also gratefully acknowledged for fruitful discussions.

To discriminate the two-step energy transfer mechanism from possible direct charge transfer processes the photoluminescence excitation (PLE) spectrum of the acceptor cascade device is measured (**Figure 4.16**). The PLE spectrum is obtained by integrating the SubNc emission ($\lambda_{em} > 700$ nm) for different excitation wavelengths (λ_{ex}) and normalizing these PL intensities for excitation at 695 nm. At this wavelength SubNc is the only absorber, and the PL signal therefore results from direct excitation of SubNc and subsequent emission. The α-6T/SubNc/SubPc three-layer device shows an increased PL intensity in the SubPc absorption region (550 nm to 600 nm) compared with the α-6T/SubNc bilayer device. If SubPc would contribute to the photocurrent generation only by a direct charge transfer process, the PL signal would result only from direct excitation of SubNc. The enhanced PL intensity, coinciding with the SubPc-related EQE peak, therefore forms direct evidence of exciton energy transfer in these cascade devices. The PLE spectrum was also measured for a device containing a co-deposited SubNc:SubPc

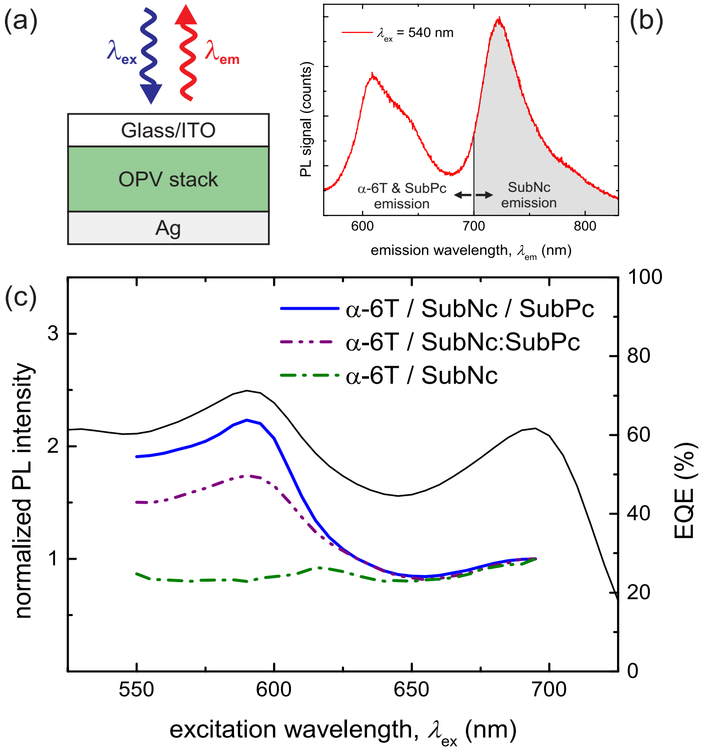

Figure 4.16: (a) Schematic illustration of PLE measurements. (b) Emission spectrum of the α-6T/SubNc/SubPc cascade device, where the shaded area indicates the wavelength range used to calculate the SubNc PL intensity. (c) The PLE spectrum of the α-6T/SubNc/SubPc cascade device is compared with the α-6T/SubNc bilayer, and a device with a SubNc:SubPc blend as acceptor. The thin solid line is the EQE spectrum of the cascade device.

blend as acceptor, instead of a discrete SubNc/SubPc junction. This device also showed an increased PL intensity in the SubPc absorption region. Although more efficient exciton transfer is expected from the close intermixing of SubPc and SubNc molecules, a lower PL intensity is observed compared with the discrete three-layer cascade. This is likely related to quenching of SubPc excitons at the α-6T interface, leaving fewer excitons available for energy transfer to SubNc. The PLE measurements of these energy cascade devices therefore confirm the dominance of the two-step exciton dissociation mechanism.

4.3 Applications

Although the performance of organic photovoltaics does not (yet) surpass conventional technologies, the unique material properties of organic semiconductors allow the development of niche applications. Efficient low-light-intensity operation, light weight, semi-transparency and esthetics are among the often cited, but rarely demonstrated unique selling points of this technology. Furthermore, organic photovoltaic devices show potential for low-cost solar energy conversion due to their ease of processing and compatibility with large-area, flexible substrates.

In this section, the performance of the α-6T/SubNc/SubPc cascade architecture is assessed for application-relevant conditions. First, the device efficiency is evaluated under varying indoor lighting conditions, relevant for energy harvesting by sensors and electronic labels. Next, semi-transparent devices are assessed for application as building-integrated photovoltaics. Finally, the upscaling possibilities of organic photovoltaics are demonstrated by developing large-area modules.

ACKNOWLEDGEMENT
Device data under indoor illumination were collected by Carl Hart de Ruijter and Ridwan Vinck, under supervision of Eszter Vörösházi. Module design, processing, patterning and characterization was carried out by Robert Gehlhaar and Erwin Vandenplas.

4.3.1 Indoor performance

The energy cascade device structure offers a simple approach to incorporate multiple absorbing materials in an organic solar cells, an advantage over the complex device structure of tandem devices. Although tandem cells can achieve efficiencies over 10% under outdoor lighting conditions, they are likely to lose performance under indoor lighting conditions as the current matching requirement of the subcells is then unsatisfied.[47] In contrast to the serial photocurrent generation in tandem devices, the active materials in energy cascade devices contribute in parallel to the photocurrent. As a consequence of this alternative exciton harvesting principle, cascade cells are insensitive to the incident light spectrum and no performance loss is expected under indoor lighting. Therefore, the performance of the three-layer α-6T/SubNc/SubPc energy cascade device was examined under indoor lighting conditions.[209]

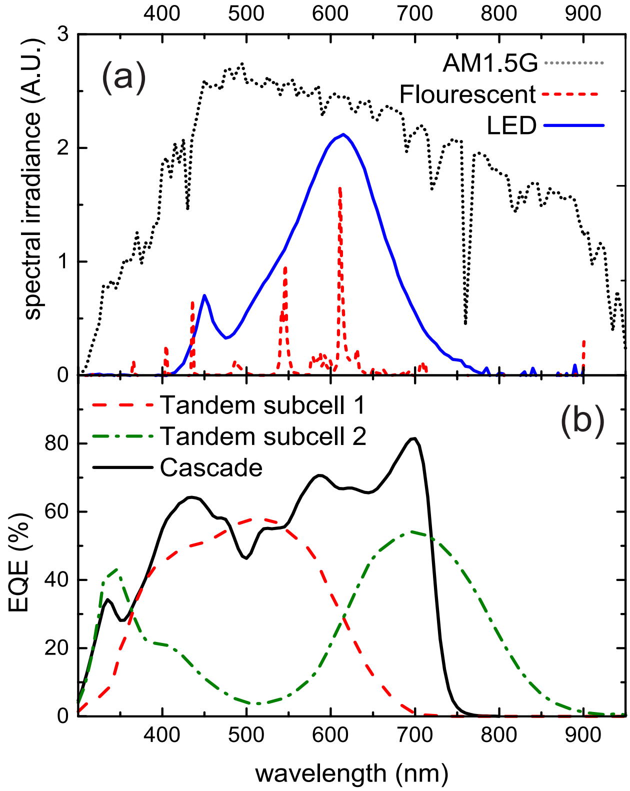

Figure 4.17: (a) Emission spectrum of indoor light sources and the AM1.5G solar illumination, and (b) EQE spectrum of the cascade cell compared with the subcells in a tandem device.

The spectrum and intensity of commercial LED and fluorescent lamps were recorded with an Avantes Starline spectroradiometer. These indoor light sources have hundred times lower intensity than the reference AM1.5G light, and their emission spectrum is mostly restricted to wavelengths between 400 nm and 800 nm (**Figure 4.17(a)**). The light intensity was varied by changing the distance between the indoor light sources and the solar cell, or by applying neutral density filters to dim the light of the solar simulator. This procedure enables evaluation of the device performance under different light intensities (P_{in}) and illumination spectra (**Figure 4.18**). Under AM1.5G illumination, the PCE of the cascade cell increases from 8.4% at 100 mW/cm^2 to over

10% at 10 mW/cm^2, a relevant and common light intensity for outdoor. Using a white LED illumination of 1.45 mW/cm^2, the PCE increases further to 20.4%. Although V_{OC} decreases to 0.86 V under these lighting conditions, the FF and responsivity ($R=J_{SC}/P_{in}$) increase to 71% and 0.33 mA/mW. This performance enhancement stems from the overlapping absorption of the photo-active materials with the LED emission spectrum and reduced resistance losses at low light intensity.

According to **equation (1.3)** and **(1.8)**, J_{SC} increases with the incident light intensity P_{in}. However, **Figure 4.18(a)** shows that the J_{SC} increase slightly deviates from linearity because the responsivity R depends on illumination conditions. The responsivity firstly depends on the spectral overlap of the incident light with the EQE of the solar cell. The responsivity is limited to 0.15 mA/mW under 100 mW/cm^2 AM1.5G illumination because a large part of the infrared spectrum of solar light is not absorbed by the cascade device. Indoor light sources, on the other hand, only emit strongly in the visible range, and the responsivity of the cascade device exceeds 0.3 mA/mW under LED and fluorescent lighting (**Figure 4.19**). The further increase of responsivity towards low light intensities is likely related to reduced recombination losses at low charge carrier densities. These small changes of R with illumination conditions cause the slight sublinear increase of J_{SC} with P_{in}. According to **equation (1.4)**, the V_{OC} logarithmically increases with J_{SC}, as seen in **Figure 4.18(b)**.

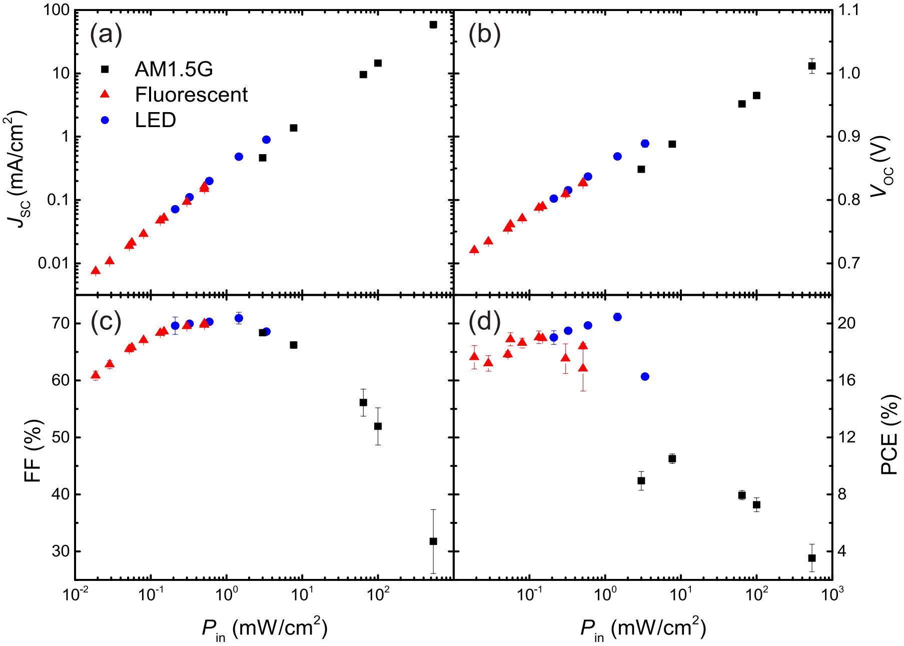

Figure 4.18: Solar cel performance parameters of the cascade device under different intensities (P_{in}) of AM1.5G, LED and fluorescent illumination.[209]

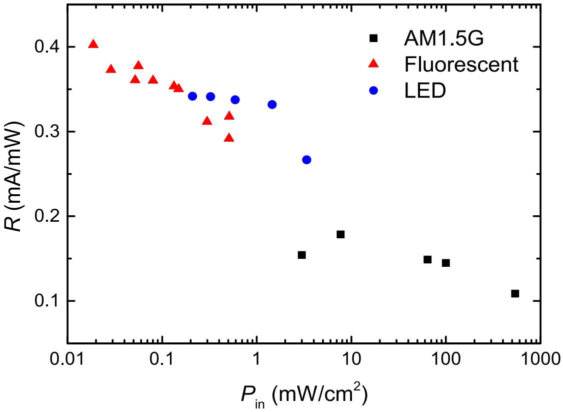

Figure 4.19: Responsivity ($R=J_{SC}/P_{in}$) of the cascade device under different light intensities (P_{in}) and spectra.[209]

The evolution of FF with light intensity (**Figure 4.18(c)**) is explained by the influence of series and shunt resistances on the *J*-*V* curve. By fitting the dark current density with the generalized diode equation (**equation (1.6)**), series and shunt resistances of respectively 22.1 Ω·cm^2 and 3.34 × 10^6 Ω·cm^2 are determined for the α-6T/SubNc/SubPc cascade device. At high light intensities, the series resistance limits the extraction of free charge carriers, and consequently reduces the FF. The shunt resistance, on the other hand, limits the FF at low light intensities because the photocurrent then matches the leakage current through the device. Similar behavior is observed for other devices independent of the photo-active materials, in agreement with previous reports.[210]

Also tandem OPV cells were characterized under indoor light conditions. The observed intensity dependence is similar to the single-junction devices. However, the responsivity of tandem devices is greatly affected by the light spectrum. For a tandem cell with two subcells, comprising either DTDCTB* or C_{70} as the main absorber, the PCE increases from 6.2% under 100 mW/cm^2 AM1.5G irradiation to 9.2% for low-intensity LED illumination, but decreases to 3.7% for fluorescent lighting (**Figure 4.20**). In case of LED lighting, the broad irradiance spectrum still generates sufficient photocurrent in both subcells, and a reduction of responsivity is avoided. In contrast, the fluorescent lamp mainly illuminates the high-bandgap subcell, and the current mismatch reduces the responsivity and efficiency of the tandem cell. This spectral sensitivity demonstrates the advantage of cascade device structures over tandem architectures.

---

* 2-{[7-(5-N,N-ditolylaminothiophen-2-yl)-2,1,3-benzothiadiazol-4-yl]methylene}malononitrile [86]

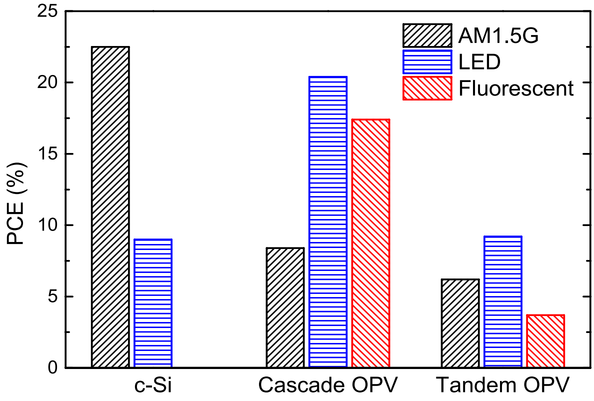

Figure 4.20: Power conversion efficiency for cascade and tandem OPV devices under different light spectra, compared with a crystalline silicon (c-Si) solar cell.[214]

In conclusion, the energy cascade device structure enables efficient low-light-intensity operation of organic photovoltaics. Moreover, the cascade OPV cell outperforms many other PV technologies under indoor light conditions.[211] For example, the PCE of crystalline Si solar cells is typically reduced below 10%, resulting from their spectral mismatch with indoor light sources and low shunt resistances (**Figure 4.20**).[212,213] Contrarily, the broad absorption of visible light coupled with low leakage current makes energy cascade OPV devices highly suitable for energy harvesting under indoor lighting.

4.3.2 Semi-transparent solar cells

Integration of (semi-)transparent photovoltaics in windows and building facades, known as building-integrated photovoltaics (BIPV), could offer low-cost power generation for self-sustaining buildings without compromising architectural designs. In this respect, the ability to make semi-transparent solar cells is a distinctive advantage of organic photovoltaics over conventional inorganic technologies. Various semi-transparent electrodes have been employed in OPV cells; including ITO,[215] Ag grids,[216] Ag nanowires,[217,218] PEDOT:PSS,[219] graphene,[220,221] and carbon nanotubes.[222,223] Here, a thin Ag film is used as semi-transparent top contact in the acceptor cascade architecture.

Semi-transparent devices with the acceptor cascade architecture (ITO/PEDOT:PSS/α-6T/SubNc/SubPc/BCP/Ag) were fabricated by varying the thickness of the Ag top contact from 10 nm to 16 nm. The wavelength-dependent transmittance of these devices was measured using a monochromator and an optical integrating sphere (see **Section 2.3.2**). The *J-V* curves were measured under 100 mW/cm^2 AM1.5G illumination, and compared with the standard (non-transparent) devices comprising a 120 nm thick Ag contact.

Reducing the Ag thickness to a few tens of nanometers allows partial transmission of visible light through the cascade device. The average visible transmittance (AVT), defined as the average of transmittance in the visible wavelength range (370 nm to 740 nm), decreases from 34% to 23% when the Ag thickness is increased from 10 nm to 16 nm (**Figure 4.21(a)**). An AVT of 25% is generally considered the benchmark for window applications.[224]

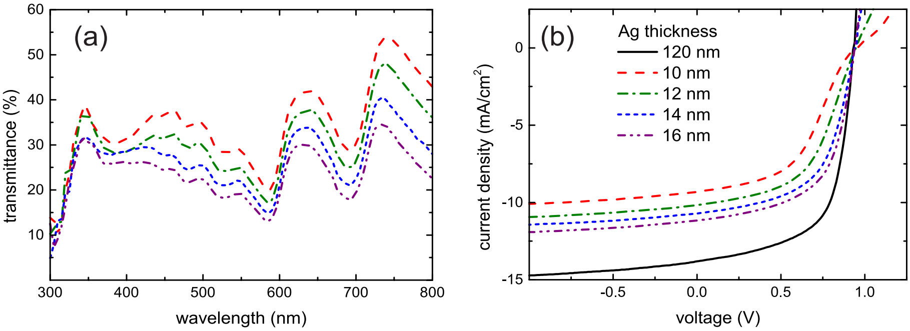

Figure 4.21: (a) Transmittance in the visible spectrum and (b) *J-V* curves, measured under 100 mW/cm^2 AM1.5G illumination, of semi-transparent acceptor cascade devices with varying Ag thickness.

Although the use of transparent electrodes inevitably reduces the light absorption and photocurrent generation in a solar cell, the semi-transparent devices still achieve high J_{SC} values. For devices with a 16 nm thick Ag contact a J_{SC} of 11.2 mA/cm^2 is obtained, corresponding to a reduction of less than 20% compared with the non-transparent device comprising a 120 nm thick Ag contact. Further reduction of the Ag thickness decreases the photocurrent as less light is absorbed, but also the FF decreases as an S-kink occurs in the *J-V* curve (**Figure 4.21(b)**). This FF decrease is possibly related to the increase of sheet resistance in thin Ag films,[224] or to an incomplete coverage of the underlying organic layers hindering efficient charge extraction. As a consequence, the PCE of the semi-transparent devices is largest for the 16 nm thick Ag contact. The PCE of 5.8% is comparable with other semi-transparent devices: in the literature efficiencies of 6.2% and 7.3% have been reported for single-junction devices and tandem devices with AVT of 20% to 30%.[224,225]

4.3.3 Modules

Upscaling of organic solar cells is required to achieve low-cost production of OPV modules. The acceptor cascade architecture was used in large-area (156 cm^2) modules in order to demonstrate the upscaling prospects of organic photovoltaics.

An ITO-coated 15-cm-by-15-cm glass substrate was used to fabricate OPV modules consisting of 24 serially connected subcells, with a total active area of 156 cm^2.

Each subcell covers a rectangular area of 0.5 cm by 13 cm, and is connected to the next subcell by a series of patterning steps (**Figure 4.22**). The patterning of the ITO film (P1) is done by wet-etch lithography, whereas the patterning of the organic layers (P2) and the metal top contact (P3) is done by mechanical scribing. Each patterning stripe is approximately 50 μm wide, and the total width of the 'dead area' amounts 200 μm to 300 μm for each subcell, or about 5% of the active area.

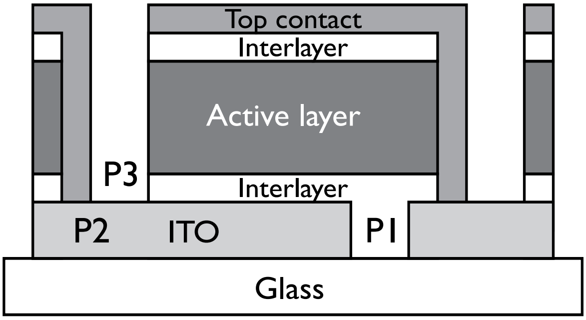

Figure 4.22: Schematic illustration of the module design. P1, P2, and P3 indicate the patterning of the ITO contact, the organic layers, and the top contact, respectively.

The active layers and charge transport layers of the modules were similar to the device structure of the optimized acceptor cascade in **Section 4.2.2**. Both opaque and semi-transparent modules were fabricated, with a 120 nm and 15 nm thick Ag top contact, respectively. Current-voltage curves were measured under 100 mW/cm^2 AM1.5G illumination (**Figure 4.23(a)** and **Table 4.4**). The opaque module achieves a PCE of 5.3%, while the semi-transparent module reaches a PCE of 4.3% despite the reduced J_{SC} and FF. The V_{OC} of both modules exceeds 20 V, corresponding to a V_{OC} of 0.87 V and 0.95 V per subcell. These values closely approach the V_{OC} of a single, small-area cell. The J_{SC} produced by each subcell and the FF of the module are lower compared with the single-cell characteristics. The photocurrent loss can be caused by local imperfections associated with the large-area processing, while the low FF is caused by contact resistance of the Ag/ITO junction forming the serial connection between the subcells. The resulting power output of the opaque and semi-transparent modules reaches 784 mW and 664 mW, respectively (**Figure 4.23(b)**). Further performance enhancement can be achieved by optimization of the patterning procedure, minimizing the series resistance losses and the dead area of the module.

Table 4.4: Solar cell performance parameters for opaque and semi-transparent modules with 24 serially connected subcells, measured under 100 mW/cm^2 AM1.5G illumination.

	V_{OC} (V)	$V_{OC}/24$ (V)	I_{SC} (mA)	J_{SC} (mA/cm^2)	$J_{SC} \cdot 24$ (mA/cm^2)	FF (%)	PCE (%)	Active area (cm^2)	Power (mW)
opaque	20.9	0.87	73.3	0.47	11.3	51	5.3	156	784
semi-transparent	22.8	0.95	62.4	0.40	9.6	47	4.3	156	664

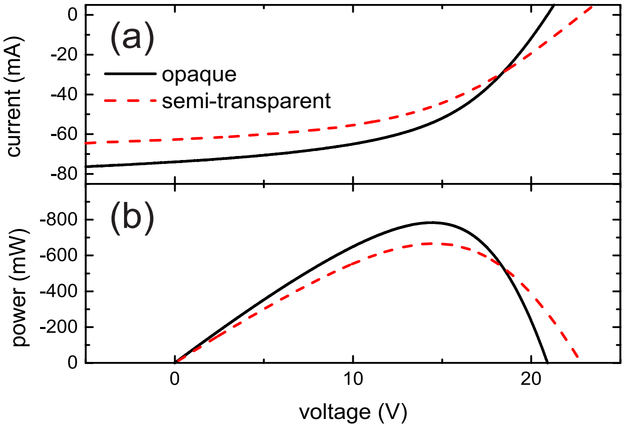

Figure 4.23: (a) Current-voltage curves and (b) power output for opaque and semi-transparent modules, measured under simulated AM1.5G solar illumination.

4.4 Comparison of multilayer architectures

Cascade architectures were introduced as alternatives for tandem devices, increasing the absorption efficiency of organic solar cells by incorporating multiple, complementary-absorbing materials in the active layer. This section compares the benefits and shortcomings of the charge transfer cascade, energy transfer cascade and tandem device architectures, as summarized in **Table 4.5**.

The main difference between the presented cascade architectures and tandem devices is that the optical complementarity of the active materials is used to enhance the photocurrent generation instead of the photovoltage output. In tandem devices the PCE is enhanced by addition of the V_{OC} of the individual subcells. All subcells ideally produce an equally high photocurrent, and the lossless recombination zone avoids reduction of V_{OC} and J_{SC}. In cascade devices, on the other hand, the presence of additional absorbers in the device structure increases the photocurrent generation instead of V_{OC}. Charge transfer cascade devices however yield low PCE despite this J_{SC} increase. The cascade-energy-level alignment in this device structure limits the V_{OC} and FF, and careful optimization of the energetic offsets is crucial to obtain efficient charge transfer cascade devices. In contrast, energy transfer cascade devices avoid such V_{OC} and FF losses, and the photocurrent increase results in a significant PCE enhancement.

As a result of the apparent benefits over the charge transfer cascade, the energy transfer cascade architecture is identified as the most viable alternative for tandem devices. As demonstrated - in this chapter and in the literature - both approaches can yield highly efficient organic solar cells. However, the different operation principles have an impact on the performance of the final application. Firstly, the high spectral sensitivity of tandem devices can limit the power output under non-standard lighting conditions. In contrast, the responsivity of cascade devices is insensitive to illumination conditions due to the parallel photocurrent generation mechanism. Their PCE even increases under low light intensities as a result of reduced resistance and recombination losses. The higher current density in cascade devices however results in high resistive losses under standard operating conditions. Therefore tandem devices are preferred for integration in large-area modules: the power losses resulting from the contact resistance between the subcells of the module are lowered by the relatively low J_{SC} of tandem cells, while their high V_{OC} ensures a high power output of the module. Further improvement in module patterning and electrode materials could however reduce these resistive losses for all OPV device structures. In conclusion, tandem device architectures are suitable for large-area, outdoor applications with little variation of the irradiation spectrum, for example in building-integrated photovoltaics, while cascade architectures are relevant for indoor applications such as low-power sensors and electronic labels which operate under varying lighting conditions.

Table 4.5: Comparison of the benefits and shortcomings of different multilayer architectures for organic solar cells.

	V_{OC}	J_{SC}	FF	Spectral sensitivity	Resistive losses in modules
Tandem	+	O	O	-	O
Charge transfer cascade	-	+	-	+	-
Energy transfer cascade	O	+	O	+	-

4.5 Chapter highlights

- A three-layer charge transfer cascade device was developed, in which SubPc acts as an ambipolar interlayer between a Tc donor and a C_{60} acceptor. Due to charge generation at both heterojunctions, the photocurrent in the cascade device is enhanced compared with the constituent bilayer devices. However, the low V_{OC} and FF related to the cascade-energy-level alignment limit the power conversion efficiency of this multilayer device.

- Efficient exciton energy transfer from SubPc to SubNc was demonstrated by photoluminescence quenching experiments. With a Förster radius of 7.5 nm, this long-range interlayer exciton transfer can be exploited to enhance exciton harvesting in multilayer energy cascade solar cells.

- The SubPc/SubNc energy relay structure was employed both at the donor and the acceptor side of an active heterojunction, enabling a two-step exciton dissociation mechanism. The developed energy cascade devices achieve high photocurrent generation without sacrificing V_{OC} and FF, resulting in device efficiencies up to 8.4%.

- The performance of the optimized energy cascade architecture is assessed for application-relevant conditions, including indoor power harvesting, semi-transparent solar cells and 156-cm^2 modules.

5. Near-infrared organic photodetectors

Besides solar power generation, organic photodiodes can be applied as photodetectors. Depending on the spectral sensitivity, such organic photodetectors can be used for a wide range of applications, such as large-area imagers, biomedical imaging, remote sensors, and telecommunication. Specifically photodetection of near-infrared (NIR) light is interesting because of the large number of industrial, medical and scientific applications in this spectral region.* Examples of applications requiring NIR detection include optical communication, night vision, process monitoring, emerging biomedical imaging techniques, chemical and biological sensors, environmental monitoring, and spectroscopic instruments.[226–229]

As the responsivity of Si photodetectors ends at wavelengths above 1100 nm, III-V compound semiconductors such as InGaAs are often used as NIR photodetectors.[230,231] Alternative approaches include epitaxially grown quantum dots or quantum well multilayer structures.[232,233] However, integration of these materials in Si readout circuits increases cost and complexity. Hence, the main benefit of organic photodetectors (OPDs) is their low cost and facile processing, enabling convenient integration with Si circuits. Furthermore, OPDs also facilitate the development of applications requiring large-area imaging or mechanical flexibility. Nevertheless, successful application of organic photodiodes as NIR detectors will require high spectral responsivity and high detectivity. For comparison, the highest-performance Si and InGaAs photodetectors achieve a specific detectivity D^* in the range of 10^{12} (cm·Hz$^{-1/2}$)/W.

This chapter discusses NIR photodetectors employing Pb phthalocyanine (PbPc) as the main absorber. The optoelectronic properties of thin PbPc films and OPD devices are described in **Section 5.1**. Because high D^* can only be achieved when the dark current through the device is low, **Section 5.2** will investigate the origin of the dark current in the PbPc-based NIR OPDs.

---

* The NIR spectrum is considered here to span wavelengths from approximately 750 nm to 2000 nm, although wavelengths above 1400 nm are sometimes designated as short-wave infrared (SWIR) light.

5.1 PbPc-based photodetectors

Thin films of metallophthalocyanines are known to exist in different crystal structures (see **Section 1.2.1**). The prevalence of a certain crystal structure depends on the thin-film deposition conditions, the interaction with the substrate, and post-deposition annealing treatments. Because the packing motif influences the molecular interactions, the crystal structure of thin Pc films influences their optical and electrical properties.

Unlike most phthalocyanines, PbPc is a non-planar molecule. Because the central Pb atom is forced outside the planar phthalocyanine ring due its large atomic radius, PbPc molecules assume a cone-shaped structure. As a result of this non-planarity, two prevalent crystal structures exist in thin PbPc films. In the *monoclinic* crystal structure the molecules are stacked linearly, forming molecular columns parallel to the c-axis (the axis perpendicular to the Pc ring).[234] In the *triclinic* crystal structure the molecules stack along the a-axis orienting their convex and concave sides alternately. The increased π-π interaction in this triclinic phase broadens the absorption spectrum and shifts the peak absorption towards NIR wavelengths. This NIR sensitivity has been exploited to broaden the absorption spectrum and enhance the photocurrent generation of organic solar cells.[17,18] However, the small optical bandgap of PbPc results in low V_{OC} values. The PCE of PbPc-based OPV cells in consequently limited to 3%.

In this section, the triclinic PbPc film is used in the active layer of NIR-sensitive photodetectors. First, the optical and morphological properties of thin PbPc films are shortly reviewed. Next, the performance of PbPc-based OPDs is evaluated.

5.1.1 Thin-film properties

Deposition of a thin PbPc film typically results in an asymmetric layer structure. Close to the substrate surface, the PbPc film assumes an amorphous or monoclinic phase. The crystal structure however evolves to a predominantly triclinic phase in the upper part of the film.[18] Modification of the crystal structure in a thin PbPc film can be achieved by adjusting the deposition rate and substrate temperature, or by using templating layers.[17,18]

Here, a thin film of copper iodide (CuI) is used to induce the triclinic phase in thin PbPc films. Insertion of such a CuI templating layer has been shown to alter the molecular orientation in thin films of ZnPc and CuPc.[14,112] Resulting from the increased interaction with the substrate, the Pc molecules in these film are oriented parallel with the substrate surface. Also in PbPc films the addition of CuI alters the molecular orientation, and the triclinic phase is dominant throughout the entire film.[17]

A 1-nm CuI film and a 40-nm PbPc film were consecutively deposited on glass substrates, both at 0.2 Å/s. The absorption spectrum of the CuI/PbPc film shows an additional peak around 900 nm compared with the non-templated PbPc film. The absorption extends to wavelengths beyond 1000 nm (**Figure 5.1**). The enhanced NIR absorption results from the dominant triclinic phase in this film, induced by the CuI templating layer.

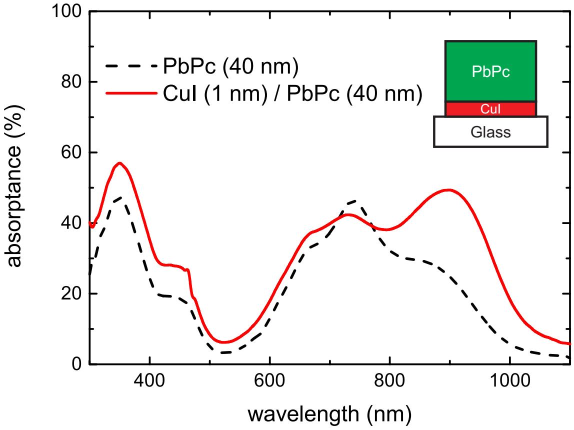

Figure 5.1: Absorption spectra of thin PbPc films. The insertion of a 1-nm CuI templating layer enhances the absorption at NIR wavelengths.

The morphology of the PbPc films was investigated by AFM (**Figure 5.2**). The non-templated PbPc film consists of crystallites with a diameter of approximately 70 nm. The height of the tallest grains is approximately 50 nm, which results in a RMS surface roughness of 9.8 nm. For the sample including the CuI templating layer, the size of the crystallites is reduced to 40 nm. Also the height difference is reduced, resulting in a lower RMS surface roughness and folding ratio.

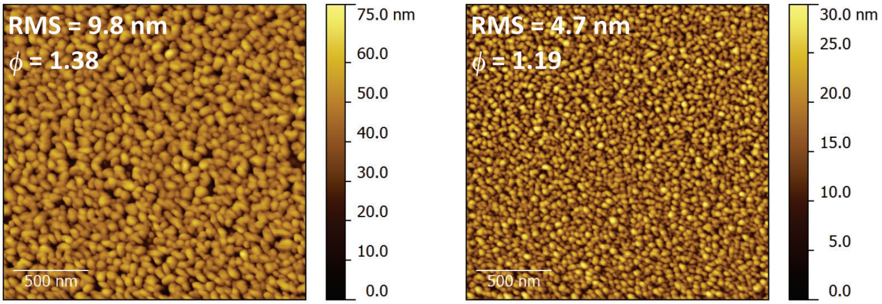

(a) PbPc (40 nm)

(b) CuI (1 nm)/PbPc (40 nm)

Figure 5.2: Atomic force microscopy images (2 µm x 2 µm) of thin films of (a) PbPc (40 nm), and (b) CuI (1 nm)/PbPc (40 nm) deposited on Si/SiO_2 substrates. The surface RMS roughness and folding ratio (ϕ) are indicated in the inset of each image.

5.1.2 Device performance

Thin PbPc films were used as the donor layer in planar-heterojunction organic photodiodes, with the following device structure: ITO/PbPc (40 nm)/C_{60} (40 nm)/BCP (10 nm)/Ag. The deposition rate of PbPc was fixed at 0.2 Å/s in order to improve reproducibility of the thin-film growth. The low deposition rate promotes formation of the triclinic phase in the PbPc donor layer, which already results in a significant NIR signal in the EQE spectrum (**Figure 5.3**). When a 1-nm CuI film is introduced at the ITO interface, the J_{SC} increases from 9.2 mA/cm^2 to 11.1 mA/cm^2 (**Figure 5.4(a)**). This enhanced photocurrent generation mainly results from a further increase of the NIR responsivity, confirming the prevalence of the triclinic PbPc phase induced by the CuI templating layer.

The dark current density flowing through the photodiode exceeds 1 mA/cm^2 at a reverse voltage of -2 V (**Figure 5.4(b)**). The reverse dark current further increases upon insertion of the CuI templating layer. As a consequence of this high leakage current, the NIR-sensitive PbPc-based OPDs have a specific detectivity below 10^9 (cm·Hz$^{-1/2}$)/W. Hence, a decrease of the dark current density by at least 5 orders of magnitude is required to achieve a detectivity comparable with inorganic OPDs.

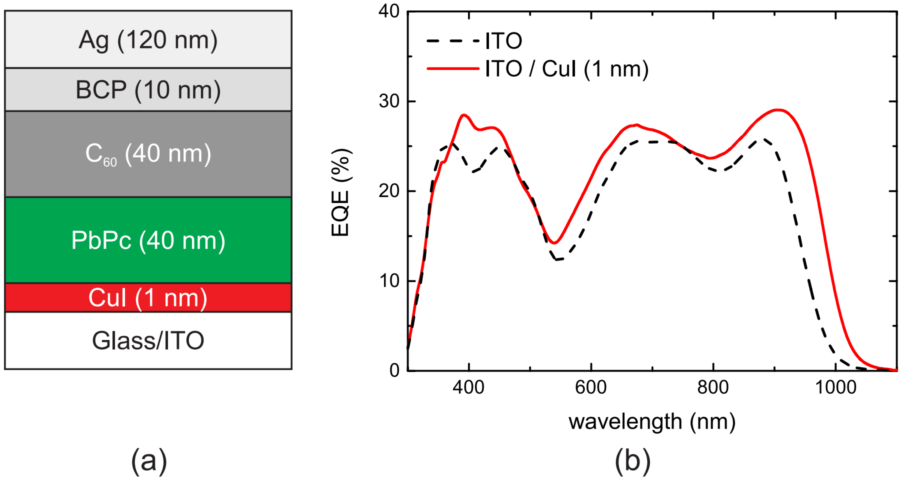

Figure 5.3: (a) Device structure, and (b) EQE spectra of PbPc-based OPD devices with NIR sensitivity. The addition of a CuI templating layer enhances the photocurrent generation in the NIR region.

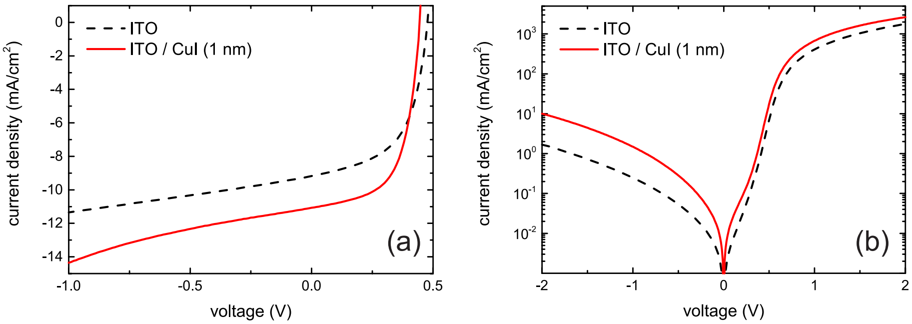

Figure 5.4: Current density-voltage curves of PbPc-based OPD devices measured (a) under 100 mW/cm^2 AM1.5G illumination, and (b) in dark.

5.2 On the origin of dark current

In order to effectively address suppression of the electronic noise in PbPc-based OPDs, the origin of the dark current has to be identified. The reverse dark current through an OPD device can originate from different mechanisms.

- **Thermal generation.** Free charge carriers can be thermally excited either in the bulk or at the donor-acceptor interface. The current resulting from thermally generated carriers scales exponentially with the activation energy. In case of bulk thermal generation, this activation energy is proportional to the bandgap of the material. At the donor-acceptor heterojunction, thermal generation of carriers can occur by excitation from the ground state to the charge transfer state. In this case the dark current varies exponentially with temperature and the interface energy gap E_{DA}. The dark current density is then given by the generalized diode equation (**equation (1.6)**), with $J_{0,n} \propto \exp(-E_{\mathrm{DA}}/2nkT)$.[79,97]

- **Reverse charge injection.** Since OPDs operate under a reverse applied voltage, charge injection from the electrodes in the active layers can occur, which comprises either hole injection from the metal cathode in the acceptor layer, or electron injection from the ITO anode in the donor layer. The injected holes or electrons can subsequently travel through the entire OPD structure and constitute a leakage current. Although secondary effects such as energetic disorder or interfacial dipoles can strongly influence the efficiency of this reverse injection process,[235] the carrier injection rate mainly depends on the injection barrier height (ϕ_{b}). The resulting injection current varies with temperature and the electric field (E): $J_{\mathrm{inj}} \propto f(E,T)\cdot\exp(-\phi_{\mathrm{b}}/kT)$, where f is a function to include electric field effects at the interface such as Schottky barrier lowering.[236] The introduction of selective charge-blocking layers should effectively suppress reverse charge injection. An electron-blocking layer ideally has a high LUMO level to increase ϕ_{b}, but a HOMO energy similar to the donor such that the collection of photogenerated charge carriers is not hindered. Likewise, a hole-blocking layer should have a low HOMO level, but LUMO energy similar to the acceptor.

- **Shunt pathways.** The presence of pinholes or other junction defects in the OPD device structure can create low-resistance pathways between the electrodes, which consequently cause a leakage current through the device. Control of the thin-film morphology and roughness is crucial to avoid such shunt defects.

- **Lateral conduction.** The active area of an OPD device is generally defined by the overlap of the anode and the cathode. However, if the active layers are unpatterned, the presence of highly conductive materials might enable current collection form the periphery of the active area. Lateral conduction can hence increase the current density through an OPD device. Nevertheless, a significant increase of the current density is only expected for small-area devices.

This section investigates the origin of the dark current in NIR-sensitive PbPc-based OPDs by temperature-dependent *J-V* measurements, and by changing the active layer and transport layers in the device structure.

5.2.1 Experimental results

It is known that the ITO workfunction significantly varies depending on the preceding surface treatment.[105] Moreover, there is a sample-to-sample variation of the ITO surface roughness. Therefore, a PEDOT:PSS layer was spin-coated on the ITO anode, improving the reproducibility of the dark-current measurements. In this study the following device structure will therefore be used as reference: ITO/PEDOT:PSS/CuI (1 nm)/PbPc (40 nm)/C_{60} (40 nm)/BCP (10 nm)/Ag. It is noted that the addition of the PEDOT:PSS buffer layer reduces the reverse dark current, resulting in a current density between 0.3 mA/cm^2 and 1 mA/cm^2 at an applied voltage of -2 V.

The temperature dependence of the *J-V* curves was studied by cooling the sample substrate to 100 K during the measurements (**Figure 5.5**). At low temperatures, the onset of forward bias shifts to higher voltages. According to the generalized diode equation (**equation (1.6)**), this shift corresponds to a decrease of the saturation current density $J_{0,n}$. Fitting of the forward current density with **equation (1.6)** shows that $J_{0,n}$ decreases exponentially with temperature, from 1.4×10^{-7} mA/cm^2 at room temperature to 1.7×10^{-10} mA/cm^2 at 108 K. This behavior results from the temperature dependence of the charge carrier recombination at the donor-acceptor heterojunction. In absence of shunts or other leakage currents, the current density at reverse bias should be dominated by thermal generation of free charge carriers at this interface, and is therefore expected to follow a similar exponential variation with temperature. However, the reverse current density of the PbPc-based OPD shows a much slower decrease at low temperature, indicating that other mechanisms are causing the high reverse dark current through the device.

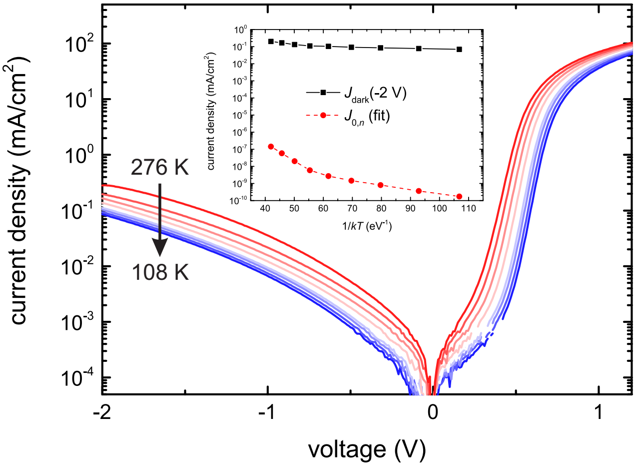

Figure 5.5: Temperature-dependent *J-V* curves of the reference PbPc-based OPD device, with the following device structure: ITO/PEDOT:PSS/CuI (1 nm)/PbPc (40 nm)/C_{60} (40 nm)/BCP (10 nm)/Ag. The inset shows the dark current density at reverse bias of -2 V, and the fitted saturation current density as function of the inverse thermal energy.

The origin of the dark current is further investigated by changing the structure of the OPD device. Firstly, adjusting the thickness of the active layers, PbPc and C_{60}, shows very little effect on the reverse dark current. Increasing the thickness of each layer to 100 nm results only in a minor decrease of the leakage current. Interestingly, the reverse dark current also decreases when the PbPc donor layer is completely removed from the device structure (**Figure 5.6(a)**). In contrast, removal of the C_{60} layer barely influences the reverse dark current. When also the 10-nm BCP layer is removed, however, the device is short-circuited, resulting from shunt pathways through the PbPc layer.

Next, the influence of the acceptor material on the dark current is studied. Replacing the C_{60} acceptor with fullerene C_{70} does not significantly alter the dark current (**Figure 5.6(b)**). In contrast, using Cl_6-SubPc-Cl as acceptor lowers the reverse dark current density by almost two orders of magnitude. This reduction in dark current could be related to the lower charge mobility of the non-fullerene acceptor.[183] The low conductivity through the acceptor layer then limits the total current flowing through the device. The fullerene-based acceptors, on the other hand, have a higher mobility, and the dark current density is limited by other layers of the device structure.

However, both hole and electron mobility are smaller in thin SubPc films compared with fullerenes.[124] Hence, this observation does not directly indicate which type of charge carriers constitutes the leakage current through the acceptor.

The charge injection in the organic layers was investigated by changing the charge transport layers of the device structure. When the thickness of the BCP electron transport layer (ETL) increases to 40 nm, the reverse dark current decreases by a factor of 50 (**Figure 5.6(c)**). In this case also the forward dark current decreases, resulting from the high series resistance of the pure BCP layer. Doping the BCP layer with low concentrations of Yb increases the conductivity, and enables the use of thicker ETLs. Only a slight increase in series resistance is observed when a 300 nm thick BCP:Yb ETL is used. Surprisingly, this doped ETL increases the reverse dark current compared with the reference device. Also when BCP is replaced by 1,4,5,8-napthalene-tetracarboxylic-dianhydride (NTCDA) the reverse dark current increases. Because NTCDA has a low HOMO level around -8 eV, hole injection from the metal cathode should be reduced compared with the BCP ETL.[122] The fact that the reverse dark current does not decrease therefore suggests that reverse hole injection is not the dominant mechanism constituting the leakage current. Instead, the reverse dark current increases when BCP:Yb or NTCDA are employed as ETL, which could result from an enhanced electron extraction through these layers.

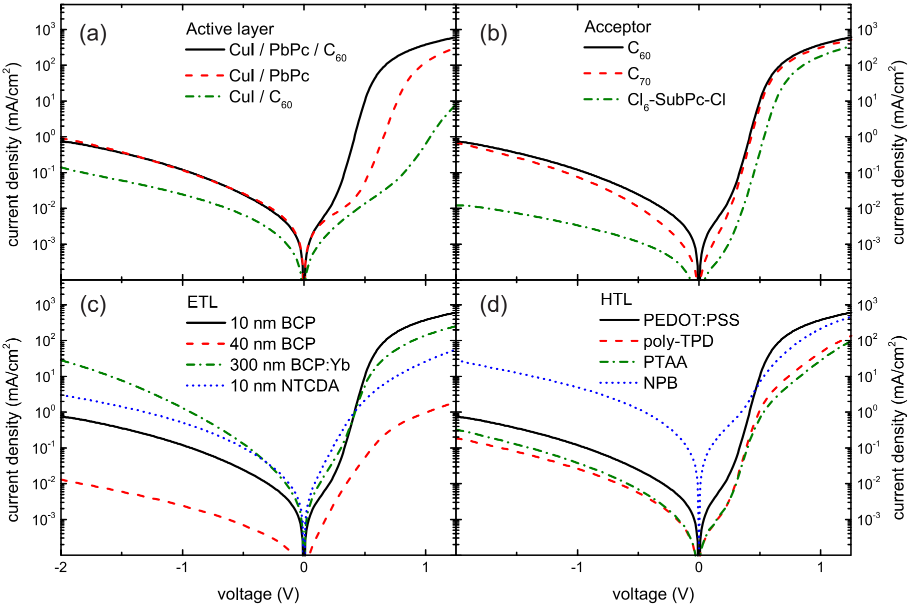

Figure 5.6: Dark *J-V* curves of PbPc-based OPD devices (a) compared with a donor-only and an acceptor-only device, (b) with different acceptor materials, (c) with different electron transport layers, and (d) with different hole transport materials.

In the reference device PEDOT:PSS was used as hole transport layer (HTL). However, PEDOT:PSS is not a perfect electron-blocking material. As a consequence, PEDOT:PSS might allow electron injection from the ITO anode in the PbPc donor layer. Therefore, the PEDOT:PSS HTL was replaced by the electron-blocking polymers poly[N,N'-bis(4-butylphenyl)-N,N'-bis(phenyl)benzidine] (poly-TPD) and poly(triarylamine) PTAA. However, the use of these polymers as HTL results only in a small decrease of the reverse dark current (**Figure 5.6(d)**). When the PEDOT:PSS HTL is replaced by a 20-nm layer of N,N'-di(1-naphthyl)-N,N'-diphenyl-(1,1'-biphenyl)-4,4'-diamine (NPB), the dark current even increases. The high LUMO level of the poly-TPD, PTAA and NPB HTLs is expected to block electron injection from the ITO anode. The fact that the reverse dark current does not significantly decreases therefore indicates that electron injection from the ITO anode is not the main source of the leakage current through the PbPc-based OPD.

5.2.2 Discussion

Based on the experimental results, several mechanisms can be ruled out as the main origin of the leakage current through the PbPc-based OPD device. Firstly, the decrease of reverse dark current at low temperatures corresponds to an activation energy of approximately 0.2 eV, which is considerably smaller than the bandgap of the triclinic PbPc phase (≈ 1.7 eV) or the interface energy gap (≈ 1.1 eV). The temperature-dependent *J-V* measurements (**Figure 5.5**) therefore indicate that the reverse dark current is not related to thermal generation of free charge carriers in the bulk PbPc layer, or at the donor-acceptor interface.

Furthermore, leakage current through shunts pathways can be excluded. Firstly, shunt paths existing in the PbPc-only device are effectively removed by addition of a 10-nm BCP layer (**Figure 5.6(a)**). Possible remaining shunts due to the rough PbPc layer morphology should therefore be completely eliminated by addition of the 300-nm BCP:Yb layer. However, the addition of this thick ETL does not result in a further decrease of the leakage current (**Figure 5.6(c)**). Addition of a 10-nm ETL thus seems sufficient to block the shunt leakage current through the device structure. Furthermore, the non-templated PbPc film actually has a higher surface roughness compared with the CuI-templated film (**Figure 5.2**). The latter however causes a higher leakage current in the OPD device (**Figure 5.4**), which is inconsistent with roughness-induced shunt pathways. Alternatively, shunt pathways could occur if the C_{60} acceptor layer contacts the anode through pinholes in the PbPc donor layer. Direct injection of electrons to C_{60} could then establish a leakage current. However, when the PbPc donor layer is completely removed from the device structure, the reverse dark current actually decreases (**Figure 5.4(a)**). Hence, direct contact between the C_{60} acceptor and the anode clearly does not cause a significant contribution to the leakage current.

Also the effect of lateral conduction in the OPD stack is shown to be minimal. The presence of highly conductive materials, such as PEDOT:PSS and C_{60}, could enhance the measured current density. Removal of the C_{60} layer however does not alter the reverse dark current in the PbPc-only device (**Figure 5.6(a)**). The presence of PEDOT:PSS even decreases the dark current. These observations confirm that lateral conduction through the PEDOT:PSS or C_{60} layer has a negligible effect on the dark current density.

With thermal generation, shunt pathways, and lateral conduction unlikely to cause a significant contribution to the reverse dark current, reverse charge injection remains as the main suspect to constitute the leakage current through the PbPc-based OPD devices. Due to the small bandgap of PbPc, a relatively low electron injection barrier exists at the ITO anode, and reverse electron injection could cause a leakage current to flow through the device. Likewise, a leakage current could result from reverse hole injection from the metal cathode to the BCP ETL. Such reverse injection processes could in principle be avoided by selective charge-blocking layers. The insertion of poly-TPD, PTAA, or NPB at the anode, and NTCDA at the cathode however does not result in a significant decrease of the leakage current (**Figure 5.6(c)** and **Figure 5.6(d)**). This observation suggests that also reverse charge injection should be ruled out as the main origin of the leakage current. However, strong interface effects, such as dipole formation and band bending, can cloud the interpretation of the results. Therefore, a further detailed study of the energy level alignment throughout the device structure is necessary to determine the precise origin of the reverse dark current. For example, a strong dipole formation is expected at the CuI/PbPc interface.[110] Furthermore, the PbPc energy levels bend upwards towards the CuI interface.[235] These effects could considerably reduce the energy difference between the CuI HOMO level and the PbPc LUMO level, and facilitate electron injection at the CuI/PbPc interface (**Figure 5.7**). The generated electron-hole pair is subsequently separated by the high electric field at reverse voltage bias. Such a charge injection process is consistent with most experimental observations of the OPD dark current.

- Because the charge injection process only occurs at the CuI/PbPc interface, the insertion of the electron-blocking HTLs (poly-TPD, PTAA, NPB) does not result in a reduction of the leakage current.

- The charge injection mechanism is temperature-independent as electrons can tunnel from the HOMO of CuI to the LUMO of PbPc, similar to the temperature-independent charge generation process at the interface between doped organic semiconductors, or at metal oxide interfaces.[109,237] The observed temperature-dependence of the reverse dark current in the PbPc-based OPD is related to the temperature-activated hopping transport of charge carriers though the organic layers.[238]

- The leakage current is only significantly suppressed when thick layers of undoped BCP or Cl_6-SubPc-Cl are introduced. The low conductivity of these materials limits the electron transport though the device. In contrast, when doped BCP:Yb or NTCDA are used as ETL, the electron extraction is enhanced, and the leakage current increases.

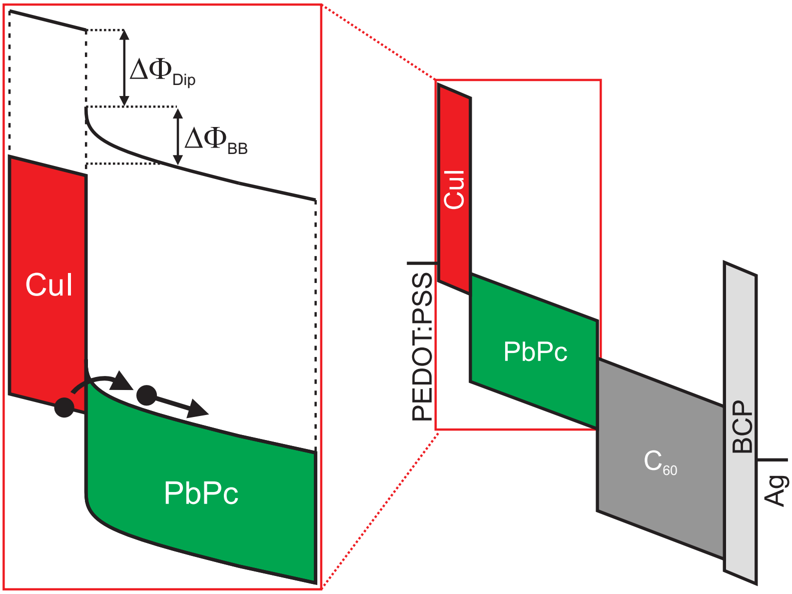

Figure 5.7: Schematic energy level diagram of a PbPc-based OPD device at reverse voltage bias. The enlargement illustrates the dipole formation, band bending and reverse charge injection at the CuI/PbPc interface.

5.3 Chapter highlights

- The incorporation of PbPc in organic photodiodes enables the development of organic photodiodes with NIR sensitivity.
- A dominant triclinic phase is induced in the PbPc donor layer by insertion of a 1-nm CuI layer at the anode. This crystal structure templating enhances the NIR responsivity of the OPD device.
- The origin of the dark current in PbPc-based OPD devices is investigated by temperature-dependent *J-V* measurements and by modification of the OPD device architecture. The high leakage current through the device is most likely caused by electron injection in the low-bandgap PbPc layer. Such charge injection can be facilitated by the formation of interface dipoles, band bending of the organic layers, and the strong electric field at reverse voltage bias.

6. Conclusions and outlook

This dissertation focused on the integration of phthalocyanines and subphthalocyanines in organic photodiodes. The unique optoelectronic properties of these small-molecule semiconductors enables the development of organic solar cells with enhanced power conversion efficiency. Furthermore, the NIR responsivity of PbPc encouraged the exploration of photodetectors with new functionalities. This chapter first summarizes the main conclusions of this work. Next, several directions for future research are discussed.

6.1 Conclusions

In **Chapter 3** subphthalocyanines were explored as alternatives for the dominant fullerene acceptors in organic solar cells. First, the correlation of heterojunction energetics and device performance was systematically investigated by employing SubPc derivatives as acceptor. The addition of peripheral substituent groups to the SubPc molecule enables tuning of the acceptor LUMO by 0.3 eV. In combination with various donor molecules, the V_{OC} of planar-heterojunction devices varies from 0.3 V to 1.1 V, corresponding to the variation of the interface energy gap E_{DA}. In contrast, a reduction in photocurrent generation is generally observed when E_{DA} increases, resulting in a trade-off between V_{OC} and photocurrent. This observation illustrates the importance of energy level alignment at the donor-acceptor heterojunction to obtain highly efficient OPV devices. In this respect, the facile energy level tuning of the SubPc acceptors represents an important advantage over fullerene acceptors, since the acceptor LUMO level forms an additional parameter to optimize OPV efficiency. For example, in case the poor energy level alignment of a donor material with fullerene acceptors results in inferior PCE values, the selection of an appropriate non-fullerene acceptor could yield an improved PCE. Furthermore, this study explored the role of charge transport layers in the device structure. The low fill factors, resulting from injection or extraction barriers at the interface with the BCP:C_{60} ETL, demonstrate that non-fullerene acceptors require adjusted buffer layers with aligned electron transport levels to enable efficient charge extraction. Also, the use of non-exciton-quenching transport layers can significantly enhance the photocurrent generation. This effect was illustrated by replacing the MoO_3 HTL by a PEDOT:PSS/DIP bilayer HTL. The optimization of donor-acceptor energetics, in combination with the selection of appropriate charge transport layers, resulted in a planar-heterojunction OPV device with a PCE of 6.9% and a V_{OC} above 1 V.

In addition to SubPc derivatives, the typical donor materials SubPc and SubNc were employed as acceptor in bilayer devices with Tc or α-6T as donor. These fullerene-free devices achieve efficiencies up to 6%. The high V_{OC} values, up to 1.2 V, result from the large interface energy gap, while the combination of strong absorption in the non-fullerene acceptors and a large donor-acceptor interface area results in high quantum efficiencies. Hence, the results presented in this chapter demonstrate that the use of non-fullerene acceptors is a promising route towards OPV efficiency improvement.

In **Chapter 4** the unique optoelectronic properties of subphthalocyanines were further exploited in multilayer device architectures. First, the ambipolar character of SubPc was exploited to develop a charge transfer cascade device. In this three-layer device structure the SubPc interlayer functions simultaneously as acceptor for the Tc donor, as well as donor for the C_{60} acceptor. The enhanced exciton harvesting in the SubPc interlayer yields a higher short-circuit current compared with the constituent bilayer devices. Although the V_{OC} increases with respect to the reference Tc/C_{60} bilayer, resulting from reduced interfacial recombination, the cascade-energy-level alignment results in an intrinsic V_{OC} loss. Moreover, the FF of the charge transfer cascade device substantially decreases when thick SubPc interlayers are used.

An alternative multilayer architecture avoids V_{OC} and FF losses by aligning the HOMO (LUMO) levels of multiple donor (acceptor) layers. Exciton harvesting from the additional active material then requires efficient interlayer exciton transfer. The molecular homologues SubPc and SubNc constitute such an energy relay system, with a Förster transfer radius of 7.5 nm demonstrated by PL quenching experiments. This long-range interlayer exciton transfer can consequently be exploited in energy transfer cascade devices, where excitons generated in the SubPc layer first transfer to the SubNc layer and subsequently dissociate at the donor-acceptor interface. This SubPc/SubNc energy relay system was incorporated both at the donor as well as the acceptor side of an active heterojunction, increasing the photocurrent generation without sacrificing V_{OC} or FF. In combination with a C_{60} acceptor, the photocurrent generation increases by nearly 50%. In combination with an α-6T donor, the quantum efficiency exceeds 75% for wavelengths between 400 nm and 720 nm. With a V_{OC} close to 1 V, this leads to a remarkable PCE of 8.4% for fullerene-free OPV devices.

Due to their high efficiency and relatively simple device structure, these multilayer cascade architectures form a promising alternative for tandem devices. The performance of these cascade devices was therefore evaluated in application-relevant conditions. Under low-light-intensity indoor illumination, the PCE of the cascade cells exceeds 20%, resulting from an increase in FF and responsivity. Furthermore, upscaling to 156-cm^2 modules yields efficiencies of 5.3% under standard solar illumination. Using a semi-transparent metal top contact, PCE values of 5.8% are obtained for single cells, and 4.3% for modules.

In **Chapter 5** near-infrared organic photodetectors were explored by applying the non-planar PbPc molecule as the active absorber. The NIR-sensitive triclinic PbPc crystal structure is induced by insertion of a thin CuI templating layer at the anode. Despite the high NIR responsivity of these OPD devices, the specific detectivity is low due to the high reverse dark current density. The origin of this leakage current is most likely caused by a temperature-independent electron injection process, facilitated by the formation of interface dipoles, band bending of the organic layers, and the strong electric field at reverse voltage bias.

6.2 Outlook

In organic electronics, performance enhancement of optoelectronic devices results both from the development of new active materials, as well as the optimization of device structure. Rational design of organic materials and device architectures is however not possible without a good understanding of the fundamental physical processes occurring in optoelectronic devices. The rapid progress in this field therefore relies on the close interplay between organic chemistry, device physics, and materials engineering. This dissertation aimed to enhance the performance of organic solar cells and photodetectors by deliberate modifications of the device structure. Highly efficient OPV cells were obtained by the introduction of non-fullerene acceptors and the development of multilayer cascade architectures. Also the detectivity of organic photodetectors was shown to crucially depend on the device structure. These results were obtained by employing phthalocyanines and subphthalocyanines as the active absorbers. The well-known optoelectronic properties of these molecules allow identification of the material and device characteristics that are crucial for further performance improvement. The results and conclusions of the device structure optimization in this work can therefore serve as guidelines in the development of new active materials or charge transport materials. In addition, further exploration of the relevant optoelectronic and solid-state properties of organic thin films and devices is imperative to drive the performance progress of organic photodiode applications.

Chapter 3 highlighted the influence of heterojunction energetics on OPV efficiency. However, a detailed investigation of charge transfer energetics and recombination kinetics can further clarify the observed differences between fullerene and non-fullerene acceptors. The deliberate design of acceptor materials could then overcome some of the shortcomings of fullerene acceptors, without sacrificing good exciton dissociation and electrons transport capabilities.[137] Furthermore, the chemical versatility of available acceptor materials could further enhance OPV efficiency by facilitating the optimization of donor-acceptor energetics. Besides this energetic tuning of the charge transfer state, alternative approaches are explored to reduce the energetic losses related to charge generation. For example, the reduction of the donor-acceptor interface area was shown to reduce the interfacial recombination processes limiting V_{OC}.[98] In this respect, planar-heterojunction devices offer an often overlooked advantage over the commonly used bulk heterojunctions, provided that the exciton diffusion step does not limit the photocurrent generation process. The design of organic materials with large exciton diffusion lengths is therefore still a promising route towards OPV efficiency enhancement. Also the control of the active layer morphology is an equivalently important approach, as evidenced by the development of organic microcrystalline films with exciton diffusion length exceeding 100 nm.[55]

This work also indicated the selection of appropriate charge transport layers as a key aspect in the design of organic photodiodes. In OPV devices, charge injection and extraction barriers should be avoided by energy level alignment of the active layer and transport layers. The expansion of the acceptor materials beyond fullerenes therefore requires an equivalent development of electron transport layers. Both hole and electron transport layers should moreover be highly conductive, optically transparent, and block exciton quenching at their interface. A combination of these properties was recently achieved in blended transport layers, where fullerenes are mixed with large-bandgap host materials.[114,239] Future research of this concept could target the development of graded blends: the gradual transition of an active layer in an exciton blocking layer. The dilution of an active material in a host was already shown to increase the exciton diffusion length in some cases.[40,56] The presence of a concentration gradient could furthermore direct the diffusion of excitons towards the active heterojunction. In addition, a graded blend of the active and transport materials avoids discrete heterojunctions which could form energetic barriers that cause charge accumulation. In OPD devices, the selection of electron and hole transport layers should mainly aim to effectively block reverse charge carrier injection. This work indicated that besides the energetic characteristics of the individual materials, also knowledge of the energy level alignment throughout the actual device structure is necessary to identify the leakage current generation mechanism. The presence of interface dipoles and strong band bending could facilitate the charge injection process, especially in low-bandgap materials such as PbPc. Knowledge and control of the energetics and molecular interactions at charge transport interfaces will therefore be crucial in the development of OPD devices with low leakage current.

In **Chapter 4** multilayer cascade architectures were presented as alternative for tandem devices. Despite the relatively simple device architecture and processing, the successful development of high-efficiency cascade devices requires the complementarity of both optical and energetic properties of the active materials. Regarding charge transfer cascade devices, the comparison of numerical drift-diffusion simulations with the experimental results could clarify which device properties limit the V_{OC} and FF. For example, improved ambipolar charge transport in the interlayer could yield improved PCE values beyond the constituent bilayer devices. Exploration of energy transfer cascade devices however revealed particularly promising prospects of multilayer cascade architectures. Identification of additional energy relay systems, either employed as donor or acceptor cascades, would enable multilayer devices with more than three active absorbers, further broadening the absorption spectrum and exciton harvesting in organic solar cells. Also the control of molecular dipole alignment could further improve the energy transfer exciton harvesting mechanism.

The ultimate goal of organic electronics research is of course the integration of this technology in innovative products and applications. Besides high efficiency, the lifetime and low-cost production of OPV devices are at least equally important to achieve commercial viability. Organic solar cells moreover compete with other thin-film PV technologies, including dye-sensitized, copper-indium-gallium-selenide, or perovskite solar cells. Market introduction of OPV cells is therefore expected by the development of niche applications that exploit the unique properties of organic semiconductors, such as semi-transparency, color-tuning, esthetics, light weight, and mechanical flexibility. Integration in portable power generation systems, indoor energy harvesters, textiles, windows, and building facades are examples of such niche applications. However, performance evaluation in application-relevant conditions, in addition to characterization under standard solar illumination, remain scarce in the field of OPV. Expansion of device characterization in such non-standard testing conditions will therefore encourage further development of OPV technology. Considering organic photodetectors, detection of near-infrared light could enable a wide range of innovative applications (as discussed in the introduction of **Chapter 5**). However, the NIR sensitivity should ideally extend beyond wavelengths of 1100 nm (the absorption cut-off of Si) to truly exploit the benefits of OPD devices. Such spectral response can be achieved by extension of the conjugated system of organic semiconductors,[240,241] introduction of inorganic quantum dots,[242,243] or single-walled carbon nanotubes.[244] Efficient charge generation and reduction of the leakage current will be the main challenges in the development of these NIR OPD applications.

Appendix: Synthesis and characterization of SubPc derivatives

All chemicals were purchased from Sigma-Aldrich Co., TCI Europe N.V. and Alfa Aesar and used without further purification. Solvents were purchased from Carlo Erba Reagents and Scharlab. Dry dimethylformamide was prepared using molecular sieves (irradiated with microwaves and dried under vacuum). 4-iodophthalonitrile[245,246] and 4,5-dichlorophthalonitrile[165] were prepared using a described procedure. Column chromatography was carried out on silica gel Merck-60 and TLC was carried out on aluminium sheets percolated with silica gel 60 F254 (Merck). ^{1}H NMR and ^{13}C NMR spectra were obtained using a Bruker Avance 300 spectrometer or a Bruker DRX-500 spectrometer. Matrix-assisted laser desorption/ionization time of flight (MALDI-TOF) MS and high-resolution mass spectrometry (HRMS) spectra were recorded with a Bruker Reflex III spectrometer. Absorption spectra in the UV-visible range were recorded with a Jasco V-660 instrument. Electrochemical measurements were performed with an Autolab PGStat 30 system using a three-electrode configuration system. The measurements were carried out using tetrahydrofuran (THF) solutions containing 0.1 M tetrabutylammonium hexafluorophosphate (TBAPF$_6$). A glassy carbon electrode (3 mm diameter) was used as the working electrode, and a platinum wire and a Ag/AgNO$_3$ (in CH$_3$CN) electrode were employed as the counter and reference electrodes, respectively. Ferrocene (Fc) was added as an internal reference, and all of the potentials are given relative to the Fc/Fc$^+$ couple. The scan rate was 100 mV/s.

Synthesis

Cl$_6$-SubPc-Cl: this compound was synthesized according to the procedure previously described.[162]

F$_{12}$-SubPc-Cl: this compound was synthesized according to the procedure previously described.[164]

Cl_4-SubPc-Cl:

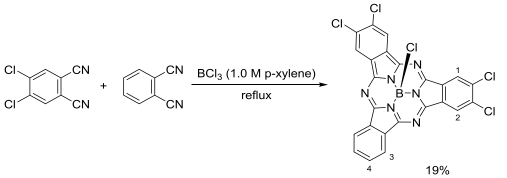

In a 25-mL two-necked round-bottomed flask, equipped with a condenser, magnetic stirrer and rubber seal, BCl_3 (5 mL, 1 M solution in p-xylene) was added to 4,5-dichlorophthalonitrile (788 mg, 4.0 mmol) and phthalonitrile (256 mg, 2.0 mmol) under argon atmosphere. The reaction mixture was stirred under vigorous reflux for 2 h. The purple solution was allowed to cool to room temperature and flushed with argon. The solvent was removed by vacuum distillation and the resulting dark solid was subjected to column chromatography on silica gel using toluene/heptane (3:1) as an eluent. By washing with heptane, **Cl_4-SubPc-Cl** was further purified, obtaining a purple solid (216 mg, 19%). mp> 250 °C; ^{1}H NMR (300 MHz, $CDCl_3$, δ): 8.98 (s, 2H; H-2), 8.94 (s, 2H; H-1), 8.92-8.83 (dd, 2H; H-3), 8.05-7.96 (dd, 2H; H-4); UV–vis ($CHCl_3$): λ_{max} (log ε) = 573 (4.5), 539 (sh), 520 (sh), 315 (4.2), 274 nm (4.2); MALDI-TOF MS m/z (%): 568.0 (100) [M^+]; HRMS (MALDI-TOF) m/z : $[M]^+$ calcd for $C_{24}H_8BCl_5N_6$, 567.9317; found, 567.9345.

$(CN)_3$-SubPc-F:

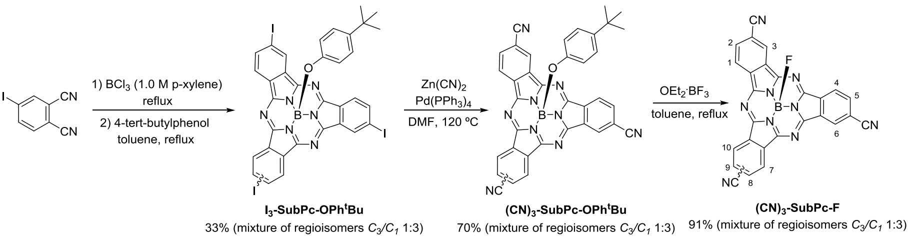

Compound **I_3-SubPc-OPh^{t}Bu** was synthesized according to the procedure previously described.[166,247]

Then, in a 25-mL two-necked round-bottomed flask, equipped with a condenser, magnetic stirrer and rubber seal, a solution of **I_3-SubPc-OPh^{t}Bu** (mixture of regioisomers C_3/C_1 1:3) (460 mg, 0.50 mmol) in dry DMF (10 mL)), $Zn(CN)_2$ (94 mg, 0.80 mmol) and tetrakis(triphenylphosphine)palladium(0) (87 mg, 0.075 mmol) were added under argon atmosphere. The reaction mixture was heated at 120 °C for 1.5 h. Water (30 mL) was added and the product was extracted with dichloromethane (3 × 25 mL). The combined organic extracts were dried over $MgSO_4$ and the solvent was removed by rotary evaporation. The solid residue was purified by column chromatography on silica gel using toluene/THF (150:1) as an eluent, yielding product **$(CN)_3$-SubPc-OPh^{t}Bu** as a purple solid (mixture of regioisomers C_3/C_1 1:3) (218 mg, 70%).

$(CN)_3$-SubPc-F was synthesized by adapting the method of Fulford et al.[167,248] In a 25-mL two-necked round-bottomed flask, equipped with a condenser, magnetic stirrer and rubber seal, **$(CN)_3$-SubPc-OPh^{t}Bu** (mixture of regioisomers C_3/C_1 1:3) (218 mg, 0.35 mmol) is dissolved in dry toluene (4 mL) under argon atmosphere. Boron trifluoride diethyl etherate ($Et_2O{\cdot}BF_3$, 1.1 mL, 25 molar equiv) was added dropwise. The reaction mixture was stirred under reflux for 5 h. The purple solution was allowed to cool to room temperature and pyridine was added dropwise until the color of the reaction to a characteristic SubPc pink color. The flask was placed in an ice bath for one hour, and the precipitate subsequently isolated by vacuum filtration. The filter cake was rinsed with methanol followed by ether to give a purple solid (156 mg, 91%). mp> 250 °C; ^{1}H NMR (300 MHz, THF-d8 , δ): 9.30 (s, 3H; H-3, H-6, H-7/H-10), 9.01 (d, $J = 8.3$ Hz, 3H; H-1, H-4, H-7/H-10), 8.36-8.27 (m, 3H; H-2, H-5, H-8/H-9); ^{19}F NMR (300 MHz, THF-d8 , δ): -159.52 (q, $J = 27.8$ Hz); UV–vis (THF): λ_{max} (log ε) = 572 (4.7), 554 (sh), 537 (sh), 521 (sh), 314 nm (4.3); MALDI-TOF MS m/z (%): 489.2 (100) [M$^+$]; HRMS (MALDI-TOF) m/z : [M]$^+$ calcd for $C_{27}H_9BFN_9$, 489.1057; found, 489.1052.

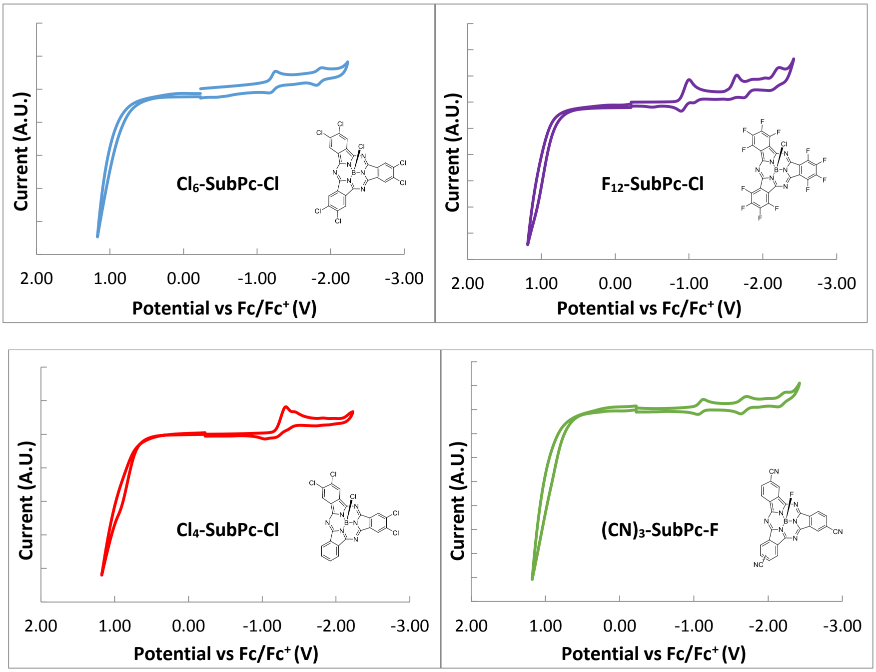

Figure A.1: Cyclic voltammograms of compounds Cl_6-SubPc-Cl, F_{12}-SubPc-Cl, Cl_4-SubPc-Cl and $(CN)_3$-SubPc-F (referred to Fc/Fc$^+$) in THF.

References

1. Forrest, S. R. The path to ubiquitous and low-cost organic electronic appliances on plastic. *Nature* **428,** 911–918 (2004).

2. Klauk, H. Organic thin-film transistors. *Chem. Soc. Rev.* **39,** 2643–2466 (2010).

3. Peumans, P., Yakimov, A. & Forrest, S. R. Small molecular weight organic thin-film photodetectors and solar cells. *J. Appl. Phys.* **93,** 3693-3723 (2003).

4. Rand, B. P., Genoe, J., Heremans, P. & Poortmans, J. Solar Cells Utilizing Small Molecular Weight Organic Semiconductors. *Prog. Photovolt: Res. Appl.* **15,** 659–676 (2007).

5. Forrest, S. R. The road to high efficiency organic light emitting devices. *Org. Electron.* **4,** 45–48 (2003).

6. Facchetti, A. Semiconductors for organic transistors. *Mater. Today* **10,** 28–37 (2007).

7. Mazzio, K. A. & Luscombe, C. K. The future of organic photovoltaics. *Chem. Soc. Rev.* **44,** 78–90 (2015).

8. Claessens, C. G., Hahn, U. & Torres, T. Phthalocyanines: From outstanding electronic properties to emerging applications. *Chem. Rec.* **8,** 75–97 (2008).

9. De la Torre, G., Claessens, C. G. & Torres, T. Phthalocyanines: old dyes, new materials. Putting color in nanotechnology. *Chem. Commun.* **20,** 2000–2015 (2007).

10. Gould, R. D. Structure and electrical conduction properties of phthalocyanine thin films. *Coord. Chem. Rev.* **156,** 237–274 (1996).

11. Linstead, R. P. Phthalocyanines. Part I. A new type of synthetic colouring matters. *J. Chem. Soc.* 1016–1017 (1934).

12. Jiang, H. et al. Fluorination of metal phthalocyanines: single-crystal growth, efficient N-channel organic field-effect transistors, and structure-property relationships. *Sci. Rep.* **4,** 7573 (2014).

13. Hohnholz, D., Steinbrecher, S. & Hanack, M. Applications of phthalocyanines in organic light emitting devices. *J. Mol. Struct.* **521,** 231–237 (2000).

14. Rand, B. P. et al. The Impact of Molecular Orientation on the Photovoltaic Properties of a Phthalocyanine/Fullerene Heterojunction. *Adv. Funct. Mater.* **22,** 2987–2995 (2012).

15. Bonnett, R. Photosensitizers of the porphyrin and phthalocyanine series for photodynamic therapy. *Chem. Soc. Rev.* **24,** 19-33 (1995).

16. Warner, M. et al. Potential for spin-based information processing in a thin-film molecular semiconductor. *Nature* **503,** 504–508 (2013).

17. Vasseur, K. et al. Controlling the Texture and Crystallinity of Evaporated Lead Phthalocyanine Thin Films for Near-Infrared Sensitive Solar Cells. *ACS Appl. Mater. Interfaces* **5,** 8505–8515 (2013).

18. Vasseur, K., Rand, B. P., Cheyns, D., Froyen, L. & Heremans, P. Structural Evolution of Evaporated Lead Phthalocyanine Thin Films for Near-Infrared Sensitive Solar Cells. *Chem. Mater.* **23,** 886–895 (2011).

19. Vasseur, K. et al. Correlating the Polymorphism of Titanyl Phthalocyanine Thin Films with Solar Cell Performance. *J. Phys. Chem. Lett.* **3**, 2395–2400 (2012).

20. Morse, G. E. & Bender, T. P. Boron Subphthalocyanines as Organic Electronic Materials. *ACS Appl. Mater. Interfaces* **4,** 5055–5068 (2012).

21. Claessens, C. G., González-Rodríguez, D. & Torres, T. Subphthalocyanines: singular nonplanar aromatic compounds-synthesis, reactivity, and physical properties. *Chem. Rev.* **102,** 835–853 (2002).

22. Mutolo, K. L., Mayo, E. I., Rand, B. P., Forrest, S. R. & Thompson, M. E. Enhanced open-circuit voltage in subphthalocyanine/C_{60} organic photovoltaic cells. *J. Am. Chem. Soc.* **128,** 8108–8109 (2006).

23. Nonell, S., Rubio, N., del Rey, B. & Torres, T. Synthesis, optical absorption and photophysical properties of cone-shaped subnaphthalocyanine. *J. Chem. Soc. Perkin Trans. 2* **6,** 1091–1094 (2000).

24. Brédas, J. L., Calbert, J. P., da Silva Filho, D. A. & Cornil, J. Organic semiconductors: a theoretical characterization of the basic parameters governing charge transport. *Proc. Natl. Acad. Sci. U. S. A.* **99,** 5804–5809 (2002).

25. Brütting, W. Physics of Organic Semiconductors. *Wiley-VCH* (2005).

26. Bässler, H. & Köhler, A. Charge transport in organic semiconductors. *Top. Curr. Chem.* **312,** 1–65 (2012).

27. Silinsh, E. A. Organic Molecular Crystals. *Springer-Verlag* (1980).

28. Price, S. L. Predicting crystal structures of organic compounds. *Chem. Soc. Rev.* **43,** 2098–2111 (2014).

29. Morse, G. E., Gong, I., Kawar, Y., Lough, A. J. & Bender, T. P. Crystal and Solid-State Arrangement Trends of Halogenated Boron Subphthalocyanines. *Cryst. Growth Des.* **14,** 2138–2147 (2014).

30. Bredas, J.-L. Mind the gap! *Mater. Horiz.* **1,** 17–19 (2014).

31. Kahn, A., Koch, N. & Gao, W. Electronic Structure and Electrical Properties of Interfaces between Metals and π-Conjugated Molecular Films. *J. Polym. Sci. Part B: Polym. Phys.* **41,** 2529–2548 (2003).

32. Djurovich, P. I., Mayo, E. I., Forrest, S. R. & Thompson, M. E. Measurement of the lowest unoccupied molecular orbital energies of molecular organic semiconductors. *Org. Electron.* **10,** 515–520 (2009).

33. Hill, I., Kahn, A., Soos, Z. G. & Pascal, R. A. Charge-separation energy in films of π-conjugated organic molecules. *Chem. Phys. Lett.* **327,** 181–188 (2000).

34. Rand, B. P. et al. Organic solar cells with sensitized phosphorescent absorbing layers. *Org. Electron.* **10,** 1015–1019 (2009).

35. Xu, Z., Hu, B. & Howe, J. Improvement of photovoltaic response based on enhancement of spin-orbital coupling and triplet states in organic solar cells. *J. Appl. Phys.* **103,** 043909 (2008).

36. Arbogast, J. W. et al. Photophysical properties of sixty atom carbon molecule (C_{60}). *J. Phys. Chem.* **95,** 11–12 (1991).

37. Terazima, M., Hirota, N., Shinohara, H. & Saito, Y. Photothermal investigation of the triplet state of carbon molecule (C_{60}). *J. Phys. Chem.* **95,** 9080–9085 (1991).

38. Burdett, J. J., Müller, A. M., Gosztola, D. & Bardeen, C. J. Excited state dynamics in solid and monomeric tetracene: The roles of superradiance and exciton fission. *J. Chem. Phys.* **133,** 144506 (2010).

39. Lunt, R. R., Giebink, N. C., Belak, A. A., Benziger, J. B. & Forrest, S. R. Exciton diffusion lengths of organic semiconductor thin films measured by spectrally resolved photoluminescence quenching. *J. Appl. Phys.* **105,** 053711 (2009).

40. Menke, S. M. & Holmes, R. J. Energy-Cascade Organic Photovoltaic Devices Incorporating a Host-Guest Architecture. *ACS Appl. Mater. Interfaces* **7,** 2912–2918 (2015).

41. Silinsh, E. A., Klimkāns, A., Larsson, S. & Čápek, V. Molecular polaron states in polyacene crystals. Formation and transfer processes. *Chem. Phys.* **198,** 311–331 (1995).

42. Li, L., Meller, G. & Kosina, H. Temperature and field-dependence of hopping conduction in organic semiconductors. *Microelectron. J.* **38,** 47–51 (2007).

43. Rand, B. P., Xue, J., Uchida, S. & Forrest, S. R. Mixed donor-acceptor molecular heterojunctions for photovoltaic applications. I. Material properties. *J. Appl. Phys.* **98,** 124902 (2005).

44. Tress, W. et al. Correlation of Absorption Profile and Fill Factor in Organic Solar Cells: The Role of Mobility Imbalance. *Adv. Energy Mater.* **3,** 631–638 (2013).

45. Cheyns, D., Kim, M., Verreet, B. & Rand, B. P. Accurate spectral response measurements of a complementary absorbing organic tandem cell with fill factor exceeding the subcells. *Appl. Phys. Lett.* **104,** 093302 (2014).

46. Dennler, G. et al. Enhanced spectral coverage in tandem organic solar cells. *Appl. Phys. Lett.* **89,** 073502 (2006).

47. Riede, M. K. et al. Efficient Organic Tandem Solar Cells based on Small Molecules. *Adv. Funct. Mater.* **21,** 3019–3028 (2011).

48. Pettersson, L. A. A., Roman, L. S. & Inganäs, O. Modeling photocurrent action spectra of photovoltaic devices based on organic thin films. *J. Appl. Phys.* **86,** 487-496 (1999).

49. Menke, S. M. & Holmes, R. J. Exciton diffusion in organic photovoltaic cells. *Energy Environ. Sci.* **7,** 499-512 (2014).

50. Förster, T. Zwischenmolekulare Energiewanderung und Fluoreszenz. *Ann. Phys.* **437,** 55–75 (1948).

51. Dexter, D. L. A Theory of Sensitized Luminescence in Solids. *J. Chem. Phys.* **21,** 836-850 (1951).

52. Bergemann, K. J. & Forrest, S. R. Measurement of exciton diffusion lengths in optically thin organic films. *Appl. Phys. Lett.* **99,** 243303 (2011).

53. Peumans, P., Uchida, S. & Forrest, S. R. Efficient bulk heterojunction photovoltaic cells using small-molecular-weight organic thin films. *Nature* **425,** 158–162 (2003).

54. Dennler, G., Scharber, M. C. & Brabec, C. J. Polymer-Fullerene Bulk-Heterojunction Solar Cells. *Adv. Mater.* **21,** 1323–1338 (2009).

55. Verreet, B., Heremans, P., Stesmans, A. & Rand, B. P. Microcrystalline organic thin-film solar cells. *Adv. Mater.* **25,** 5504–5507 (2013).

56. Menke, S. M., Luhman, W. A. & Holmes, R. J. Tailored exciton diffusion in organic photovoltaic cells for enhanced power conversion efficiency. *Nat. Mater.* **12,** 152–157 (2013).

57. Luhman, W. A. & Holmes, R. J. Enhanced exciton diffusion in an organic photovoltaic cell by energy transfer using a phosphorescent sensitizer. *Appl. Phys. Lett.* **94,** 153304 (2009).

58. Gommans, H. et al. On the Role of Bathocuproine in Organic Photovoltaic Cells. *Adv. Funct. Mater.* **18,** 3686–3691 (2008).

59. Hirade, M. & Adachi, C. Small molecular organic photovoltaic cells with exciton blocking layer at anode interface for improved device performance. *Appl. Phys. Lett.* **99,** 153302 (2011).

60. Clarke, T. M. & Durrant, J. R. Charge photogeneration in organic solar cells. *Chem. Rev.* **110,** 6736–6767 (2010).

61. Deibel, C., Strobel, T. & Dyakonov, V. Role of the charge transfer state in organic donor-acceptor solar cells. *Adv. Mater.* **22,** 4097–4111 (2010).

62. Tvingstedt, K., Vandewal, K., Gadisa, A. & Zhang, F. Electroluminescence from Charge Transfer States in Polymer Solar Cells. *J. Am. Chem. Soc.* **131,** 11819–11824 (2009).

63. Vandewal, K. et al. Fourier-Transform Photocurrent Spectroscopy for a fast and highly sensitive spectral characterization of organic and hybrid solar cells. *Thin Solid Films* **516,** 7135–7138 (2008).

64. Hoke, E. T. et al. Recombination in Polymer:Fullerene Solar Cells with Open-Circuit Voltages Approaching and Exceeding 1.0 V. *Adv. Energy Mater.* **3,** 220–230 (2012).

65. Veldman, D., Meskers, S. C. J. & Janssen, R. A. J. The Energy of Charge-Transfer States in Electron Donor-Acceptor Blends: Insight into the Energy Losses in Organic Solar Cells. *Adv. Funct. Mater.* **19,** 1939–1948 (2009).

66. Marcus, R. A. On the Theory of Oxidation-Reduction Reactions Involving Electron Transfer. I. *J. Chem. Phys.* **24,** 966-978 (1956).

67. Lemaur, V., Steel, M., Beljonne, D., Brédas, J. L. & Cornil, J. Photoinduced charge generation and recombination dynamics in model donor/acceptor pairs for organic solar cell applications: A full quantum-chemical treatment. *J. Am. Chem. Soc.* **127,** 6077–6086 (2005).

68. Braun, C. L. Electric field assisted dissociation of charge transfer states as a mechanism of photocarrier production. *J. Chem. Phys.* **80,** 4157-4161 (1984).

69. Pasveer, W. F. et al. Unified Description of Charge-Carrier Mobilities in Disordered Semiconducting Polymers. *Phys. Rev. Lett.* **94,** 206601 (2005).

70. Pivrikas, A., Sariciftci, N. S., Juška, G. & Österbacka, R. A review of charge transport and recombination in polymer/fullerene organic solar cells. *Prog. Photovolt: Res. Appl.* **15,** 677–696 (2007).

71. Tress, W., Leo, K. & Riede, M. K. Influence of Hole-Transport Layers and Donor Materials on Open-Circuit Voltage and Shape of I-V Curves of Organic Solar Cells. *Adv. Funct. Mater.* **21,** 2140–2149 (2011).

72. Mityashin, A., Cheyns, D., Rand, B. P. & Heremans, P. Understanding metal doping for organic electron transport layers. *Appl. Phys. Lett.* **100,** 053305 (2012).

73. Shockley, W. & Queisser, H. J. Detailed Balance Limit of Efficiency of p-n Junction Solar Cells. *J. Appl. Phys.* **32,** 510-519 (1961).

74. Giebink, N. C., Wiederrecht, G. P., Wasielewski, M. R. & Forrest, S. R. Ideal diode equation for organic heterojunctions. I. Derivation and application. *Phys. Rev. B* **82,** 155305 (2010).

75. Rau, U. Reciprocity relation between photovoltaic quantum efficiency and electroluminescent emission of solar cells. *Phys. Rev. B* **76,** 085303 (2007).

76. Vandewal, K., Tvingstedt, K., Gadisa, A., Inganäs, O. & Manca, J. V. On the origin of the open-circuit voltage of polymer-fullerene solar cells. *Nat. Mater.* **8,** 904–909 (2009).

77. Vandewal, K., Tvingstedt, K., Gadisa, A., Inganäs, O. & Manca, J. V. Relating the open-circuit voltage to interface molecular properties of donor:acceptor bulk heterojunction solar cells. *Phys. Rev. B* **81,** 125204 (2010).

78. Potscavage, W. J., Yoo, S. & Kippelen, B. Origin of the open-circuit voltage in multilayer heterojunction organic solar cells. *Appl. Phys. Lett.* **93,** 193308 (2008).

79. Rand, B. P., Burk, D. P. & Forrest, S. R. Offset energies at organic semiconductor heterojunctions and their influence on the open-circuit voltage of thin-film solar cells. *Phys. Rev. B* **75,** 115327 (2007).

80. Wu, L., Zang, H., Hsiao, Y.-C., Zhang, X. & Hu, B. Origin of the fill factor loss in bulk-heterojunction organic solar cells. *Appl. Phys. Lett.* **104,** 153903 (2014).

81. Tang, C. W. Two-layer organic photovoltaic cell. *Appl. Phys. Lett.* **48,** 183–185 (1986).

82. Winder, C. & Sariciftci, N. S. Low bandgap polymers for photon harvesting in bulk heterojunction solar cells. *J. Mater. Chem.* **14,** 1077-1086 (2004).

83. Vandewal, K. et al. Quantification of Quantum Efficiency and Energy Losses in Low Bandgap Polymer:Fullerene Solar Cells with High Open-Circuit Voltage. *Adv. Funct. Mater.* **22,** 3480–3490 (2012).

84. Green, M. A., Emery, K., Hishikawa, Y., Warta, W. & Dunlop, E. D. Solar cell efficiency tables (Version 45). *Prog. Photovolt: Res. Appl.* **23,** 1–9 (2015).

85. Heliatek consolidates its technology leadership by establishing a new world record for organic solar technology with a cell efficiency of 12%. *Heliatek GmbH*, january 16 (2013).

86. Che, X., Xiao, X., Zimmerman, J. D., Fan, D. & Forrest, S. R. High-Efficiency, Vacuum-Deposited, Small-Molecule Organic Tandem and Triple-Junction Photovoltaic Cells. *Adv. Energy Mater.* **4,** 1400568 (2014).

87. You, J. et al. A polymer tandem solar cell with 10.6% power conversion efficiency. *Nat. Commun.* **4,** 1446 (2013).

88. He, Z. et al. Single-junction polymer solar cells with high efficiency and photovoltage. *Nat. Photonics* **9,** 174–179 (2015).

89. Jagadamma, L. K. et al. Polymer Solar Cells with Efficiency >10% Enabled via a Facile Solution-Processed Al-Doped ZnO Electron Transporting Layer. *Adv. Energy Mater.* **5,** 1500204 (2015).

90. Kan, B. et al. A Series of Simple Oligomer-like Small Molecules Based on Oligothiophenes for Solution-Processed Solar Cells with High Efficiency. *J. Am. Chem. Soc.* **137,** 3886–3893 (2015).

91. Park, S. H. et al. Bulk heterojunction solar cells with internal quantum efficiency approaching 100%. *Nat. Photonics* **3,** 297–302 (2009).

92. Zhang, Q. et al. Small-molecule solar cells with efficiency over 9%. *Nat. Photonics* **9,** 35–41 (2014).

93. Cheyns, D., Rand, B. P. & Heremans, P. Organic tandem solar cells with complementary absorbing layers and a high open-circuit voltage. *Appl. Phys. Lett.* **97,** 033301 (2010).

94. Dou, L. et al. Tandem polymer solar cells featuring a spectrally matched low-bandgap polymer. *Nat. Photonics* **6,** 180–185 (2012).

95. Wilke, A. et al. Correlation between interface energetics and open circuit voltage in organic photovoltaic cells. *Appl. Phys. Lett.* **101**, 233301 (2012).

96. Graham, K. R. et al. Re-evaluating the Role of Sterics and Electronic Coupling in Determining the Open-Circuit Voltage of Organic Solar Cells. *Adv. Mater.* **25,** 6076–6082 (2013).

97. Perez, M. D., Borek, C., Forrest, S. R. & Thompson, M. E. Molecular and morphological influences on the open circuit voltages of organic photovoltaic devices. *J. Am. Chem. Soc.* **131,** 9281–9286 (2009).

98. Vandewal, K. et al. Increased open-circuit voltage of organic solar cells by reduced donor-acceptor interface area. *Adv. Mater.* **26,** 3839–3843 (2014).

99. Gong, X. et al. High-detectivity polymer photodetectors with spectral response from 300 nm to 1450 nm. *Science* **325,** 1665–1667 (2009).

100. Baeg, K.-J., Binda, M., Natali, D., Caironi, M. & Noh, Y.-Y. Organic light detectors: photodiodes and phototransistors. *Adv. Mater.* **25,** 4267–4295 (2013).

101. De Michele, M., Leprince, S., Thiébot, J., Raucoules, D. & Binet, R. Direct measurement of ocean waves velocity field from a single SPOT-5 dataset. *Remote Sens. Environ.* **119,** 266–271 (2012).

102. Antognazza, M. R., Musitelli, D., Perissinotto, S. & Lanzani, G. Spectrally selected photodiodes for colorimetric application. *Org. Electron.* **11,** 357–362 (2010).

103. Nalwa, K. S. et al. Polythiophene-fullerene based photodetectors: Tuning of spectral esponse and application in photoluminescence based (Bio)chemical sensors. *Adv. Mater.* **22,** 4157–4161 (2010).

104. Kim, H. et al. Electrical, optical, and structural properties of indium–tin–oxide thin films for organic light-emitting devices. *J. Appl. Phys.* **86,** 6451–6461 (1999).

105. Sugiyama, K., Ishii, H., Ouchi, Y. & Seki, K. Dependence of indium-tin-oxide work function on surface cleaning method as studied by ultraviolet and x-ray photoemission spectroscopies. *J. Appl. Phys.* **87,** 295–298 (2000).

106. Voroshazi, E. et al. Influence of cathode oxidation via the hole extraction layer in polymer:fullerene solar cells. *Org. Electron.* **12,** 736–744 (2011).

107. Sarasqueta, G., Choudhury, K. R., Subbiah, J. & So, F. Organic and inorganic blocking layers for solution-processed colloidal PbSe nanocrystal infrared photodetectors. *Adv. Funct. Mater.* **21,** 167–171 (2011).

108. Schols, S. et al. An Organic Light-Emitting Diode with Field-Effect Electron Transport. *Adv. Funct. Mater.* **18,** 136–144 (2008).

109. Meyer, J. et al. Transition metal oxides for organic electronics: energetics, device physics and applications. *Adv. Mater.* **24,** 5408–5427 (2012).

110. Kim, J. W. et al. High performance organic planar heterojunction solar cells by controlling the molecular orientation. *Curr. Appl. Phys.* **13,** 7–11 (2013).

111. Shao, S. et al. Interface-Induced Crystalline Ordering and Favorable Morphology for Efficient Annealing-Free Poly(3-hexylthiophene): Fullerene Derivative Solar Cells. *ACS Appl. Mater. Interfaces* **4,** 5704–5710 (2012).

112. Cheng, C. H. et al. Organic solar cells with remarkable enhanced efficiency by using a CuI buffer to control the molecular orientation and modify the anode. *Appl. Phys. Lett.* **97**, 083305 (2010).

113. Rand, B. P. et al. Organic Double-Heterostructure Photovoltaic Cells Employing Thick Tris(acetylacetonato)ruthenium(III) Exciton-Blocking Layers. *Adv. Mater.* **17,** 2714–2718 (2005).

114. Bartynski, A. N. et al. A Fullerene-Based Organic Exciton Blocking Layer with High Electron Conductivity. *Nano Lett.* **13,** 3315–3320 (2013).

115. Barito, A. et al. Universal Design Principles for Cascade Heterojunction Solar Cells with High Fill Factors and Internal Quantum Efficiencies Approaching 100%. *Adv. Energy Mater.* **4,** 1400216 (2014).

116. Ikushima, A. J., Kanno, T., Yoshida, S. & Maeda, A. Valence and conduction band edges of metal-phthalocyanines behavior and carrier behavior. *Thin Solid Films* **273,** 35–38 (1996).

117. Pfuetzner, S., Meiss, J., Petrich, A., Riede, M. K. & Leo, K. Improved bulk heterojunction organic solar cells employing C_{70} fullerenes. *Appl. Phys. Lett.* **94,** 223307 (2009).

118. Lassiter, B. E. et al. Organic photovoltaics incorporating electron conducting exciton blocking layers. *Appl. Phys. Lett.* **98,** 243307 (2011).

119. Ohkita, H. et al. Charge Carrier Formation in Polythiophene / Fullerene Blend Films Studied by Transient Absorption Spectroscopy. *J. Am. Chem. Soc.* **130,** 3030–3042 (2008).

120. Shoaee, S. et al. Acceptor Energy Level Control of Charge Photogeneration in Organic Donor / Acceptor Blends. *J. Am. Chem. Soc.* **132,** 12919–12926 (2010).

121. Sariciftci, N. S., Smilowitz, L., Heeger, A. J. & Wudi, F. Photoinduced Electron Transfer from a Conducting Polymer to Buckminsterfullerene. *Science* **258,** 1474–1476 (1992).

122. He, Y. & Li, Y. Fullerene derivative acceptors for high performance polymer solar cells. *Phys. Chem. Chem. Phys.* **13,** 1970–1983 (2011).

123. Li, C.-Z., Yip, H.-L. & Jen, A. K.-Y. Functional fullerenes for organic photovoltaics. *J. Mater. Chem.* **22,** 4161–4177 (2012).

124. Pandey, R., Gunawan, A. A., Mkhoyan, K. A. & Holmes, R. J. Efficient Organic Photovoltaic Cells Based on Nanocrystalline Mixtures of Boron Subphthalocyanine Chloride and C_{60}. *Adv. Funct. Mater.* **22,** 617–624 (2012).

125. Lin, Y., Li, Y. & Zhan, X. Small molecule semiconductors for high-efficiency organic photovoltaics. *Chem. Soc. Rev.* **41,** 4245–4272 (2012).

126. Mishra, A. & Bäuerle, P. Small molecule organic semiconductors on the move: promises for future solar energy technology. *Angew. Chem. Int. Ed. Engl.* **51,** 2020–2067 (2012).

127. Tong, X., Wang, N., Slootsky, M., Yu, J. & Forrest, S. R. Intrinsic burn-in efficiency loss of small-molecule organic photovoltaic cells due to exciton-induced trap formation. *Sol. Energy Mater. Sol. Cells* **118,** 116–123 (2013).

128. Zhang, H. et al. Photochemical Transformations in Fullerene and Molybdenum Oxide Affect the Stability of Bilayer Organic Solar Cells. *Adv. Energy Mater.* **5,** 1400734 (2014).

129. Anctil, A., Babbitt, C. W., Raffaelle, R. P. & Landi, B. J. Material and energy intensity of fullerene production. *Environ. Sci. Technol.* **45,** 2353–2359 (2011).

130. Anctil, A., Babbitt, C. W., Raffaelle, R. P. & Landi, B. J. Cumulative energy demand for small molecule and polymer photovoltaics. *Prog. Photovolt: Res. Appl.* **21,** 1541–1554 (2013).

131. Huang, C., Barlow, S. & Marder, S. R. Perylene-3,4,9,10-tetracarboxylic acid diimides: synthesis, physical properties, and use in organic electronics. *J. Org. Chem.* **76,** 2386–2407 (2011).

132. Shin, W. S. et al. Effects of functional groups at perylene diimide derivatives on organic photovoltaic device application. *J. Mater. Chem.* **16,** 384–390 (2006).

133. Hörmann, U., Wagner, J., Gruber, M., Opitz, A. & Brütting, W. Approaching the ultimate open circuit voltage in thiophene based single junction solar cells by applying diindenoperylene as acceptor. *Phys. Status Solidi RRL* **5,** 241–243 (2011).

134. Mikroyannidis, J. A., Suresh, P. & Sharma, G. D. Synthesis of a perylene bisimide with acetonaphthopyrazine dicarbonitrile terminal moieties for photovoltaic applications. *Synth. Met.* **160,** 932–938 (2010).

135. Anthony, J. E. Small-Molecule, Nonfullerene Acceptors for Polymer Bulk Heterojunction Organic Photovoltaics. *Chem. Mater.* **23,** 583–590 (2011).

136. Sonar, P., Fong Lim, J. P. & Chan, K. L. Organic non-fullerene acceptors for organic photovoltaics. *Energy Environ. Sci.* **4,** 1558–1574 (2011).

137. Lin, Y. & Zhan, X. Non-fullerene acceptors for organic photovoltaics: an emerging horizon. *Mater. Horiz.* **1,** 470–488 (2014).

138. Qu, S. & Tian, H. Diketopyrrolopyrrole (DPP)-based materials for organic photovoltaics. *Chem. Commun.* **48,** 3039-3051 (2012).

139. Nielsen, C. B. et al. Efficient truxenone-based acceptors for organic photovoltaics. *J. Mater. Chem. A* **1,** 73–76 (2013).

140. Nielsen, C. B. et al. Electron-deficient truxenone derivatives and their use in organic photovoltaics. *J. Mater. Chem. A* **2,** 12348–12354 (2014).

141. Barbarella, G., Pudova, O., Arbizzani, C., Mastragostino, M. & Bongini, A. Oligothiophene-S,S-dioxides: a New Class of Thiophene-based Materials. *J. Org. Chem.* **63,** 1742–1745 (1998).

142. Barbarella, G. et al. Oligothiophene S,S-dioxides. Synthesis and electronic properties in relation to the parent oligothiophenes. *J. Org. Chem.* **63,** 5497–5506 (1998).

143. Lim, Y.-F., Shu, Y., Parkin, S. R., Anthony, J. E. & Malliaras, G. G. Soluble n-type pentacene derivatives as novel acceptors for organic solar cells. *J. Mater. Chem.* **19,** 3049 (2009).

144. Halls, J. J. M. et al. Efficient photodiodes from interpenetrating polymer networks. *Nature* **376,** 498–500 (1995).

145. Yu, G., Gao, J., Hummelen, J. C., Wudl, F. & Heeger, A. J. Polymer Photovoltaic Cells: Enhanced Efficiencies via a Network of Internal Donor-Acceptor Heterojunctions. *Science* **270,** 1789–1791 (1995).

146. Zhan, X. et al. A high-mobility electron-transport polymer with broad absorption and its use in field-effect transistors and all-polymer solar cells. *J. Am. Chem. Soc.* **129,** 7246–7247 (2007).

147. Hwang, Y. J., Ren, G., Murari, N. M. & Jenekhe, S. A. n-Type naphthalene diimide-biselenophene copolymer for all-polymer bulk heterojunction solar cells. *Macromolecules* **45,** 9056–9062 (2012).

148. Zang, Y. et al. Integrated molecular, interfacial, and device engineering towards high-performance non-fullerene based organic solar cells. *Adv. Mater.* **26,** 5708–5714 (2014).

149. Zhang, X., Zhan, C. & Yao, J. Non-Fullerene Organic Solar Cells with 6.1% Efficiency through Fine-Tuning Parameters of the Film-Forming Process. *Chem. Mater.* **27,** 166–173 (2015).

150. Zhao, J. et al. High-efficiency non-fullerene organic solar cells enabled by a difluorobenzothiadiazole-based donor polymer combined with a properly matched small molecule acceptor. *Energy Environ. Sci.* **8,** 520–525 (2015).

151. Zhong, Y. et al. Efficient Organic Solar Cells with Helical Perylene Diimide Electron Acceptors. *J. Am. Chem. Soc.* **136,** 15215–15221 (2014).

152. Facchetti, A. Polymer donor-polymer acceptor (all-polymer) solar cells. *Mater. Today* **16,** 123–132 (2013).

153. Lin, Y. et al. An Electron Acceptor Challenging Fullerenes for Efficient Polymer Solar Cells. *Adv. Mater.* **27,** 1170–1174 (2015).

154. Brinkmann, H. et al. Fluorinated phthalocyanines as molecular semiconductor thin films. *Phys. Status Solidi A* **205,** 409–420 (2008).

155. Meiss, J. et al. Fluorinated zinc phthalocyanine as donor for efficient vacuum-deposited organic solar cells. *Adv. Funct. Mater.* **22,** 405–414 (2012).

156. Peisert, H., Knupfer, M. & Fink, J. Electronic structure of partially fluorinated copper phthalocyanine ($CuPCF_4$) and its interface to Au(100). *Surf. Sci.* **515,** 491–498 (2002).

157. Yang, J. L., Schumann, S., Hatton, R. a. & Jones, T. S. Copper hexadecafluorophthalocyanine ($F_{16}CuPc$) as an electron accepting material in bilayer small molecule organic photovoltaic cells. *Org. Electron.* **11,** 1399–1402 (2010).

158. Gommans, H. et al. Perfluorinated Subphthalocyanine as a New Acceptor Material in a Small-Molecule Bilayer Organic Solar Cell. *Adv. Funct. Mater.* **19,** 3435–3439 (2009).

159. Sullivan, P. et al. Halogenated Boron Subphthalocyanines as Light Harvesting Electron Acceptors in Organic Photovoltaics. *Adv. Energy Mater.* **1,** 352–355 (2011).

160. Morse, G. E., Gantz, J. L., Steirer, K. X., Armstrong, N. R. & Bender, T. P. Pentafluorophenoxy Boron Subphthalocyanine ($F_5BsubPc$) as a Multifunctional Material for Organic Photovoltaics. *ACS Appl. Mater. Interfaces* **6,** 1515–1524 (2014).

161. Verreet, B. et al. A 4% Efficient Organic Solar Cell Using a Fluorinated Fused Subphthalocyanine Dimer as an Electron Acceptor. *Adv. Energy Mater.* **1,** 565–568 (2011).

162. Verreet, B. et al. Decreased recombination through the use of a non-fullerene acceptor in a 6.4% efficient organic planar heterojunction solar cell. *Adv. Energy Mater.* **4,** 1301413 (2014).

163. Cnops, K. et al. Energy Level Tuning of Non-fullerene Acceptors in Organic Solar Cells. *J. Am. Chem. Soc.* **137,** 8991–8997 (2015).

164. Claessens, C. G. et al. Highly Efficient Synthesis of Chloro- and Phenoxy-Substituted Subphthalocyanines. *Eur. J. Org. Chem.* **2003**, 2547–2551 (2003).

165. Wöhrle, D., Eskes, M., Shigehara, K. & Yamada, A. A Simple Synthesis of 4,5-Disubstituted 1,2-Dicyanobenzenes and 2,3,9,10,16,17,23,24-Octasubstituted Phthalocyanines. *Synthesis* **2,** 194–196 (1993).

166. Claessens, C. G. & Torres, T. Subphthalocyanine enantiomers: first resolution of a C_3 aromatic compound by HPLC. *Tetrahedron Lett.* **41,** 6361–6365 (2000).

167. Rodríguez-Morgade, M. S. et al. Synthesis, characterization, molecular structure and theoretical studies of axially fluoro-substituted subazaporphyrins. *Chem. - Eur. J.* **14,** 1342–1350 (2008).

168. Hancox, I. et al. The effect of a MoO_x hole-extracting layer on the performance of organic photovoltaic cells based on small molecule planar heterojunctions. *Org. Electron.* **11,** 2019–2025 (2010).

169. Renshaw, C. K., Zimmerman, J. D., Lassiter, B. E. & Forrest, S. R. Photoconductivity in donor-acceptor heterojunction organic photovoltaics. *Phys. Rev. B* **86,** 085324 (2012).

170. Jeong, W.-I. et al. Photoconductivity of C_{60} as an Origin of Bias-Dependent Photocurrent in Organic Photovoltaics. *Adv. Funct. Mater.* **22,** 3089–3094 (2012).

171. Xiao, X., Zimmerman, J. D., Lassiter, B. E., Bergemann, K. J. & Forrest, S. R. A hybrid planar-mixed tetraphenyldibenzoperiflanthene/C_{70} photovoltaic cell. *Appl. Phys. Lett.* **102,** 073302 (2013).

172. Barito, A. et al. Recovering lost excitons in organic photovoltaics using a transparent dissociation layer. *J. Appl. Phys.* **113,** 203110 (2013).

173. Lin, C.-F. et al. Chloroboron subphthalocyanine/C_{60} planar heterojunction organic solar cell with N,N-dicarbazolyl-3,5-benzene blocking layer. *Sol. Energy Mater. Sol. Cells* **122,** 264–270 (2014).

174. Gommans, H. et al. Electro-Optical Study of Subphthalocyanine in a Bilayer Organic Solar Cell. *Adv. Funct. Mater.* **17,** 2653–2658 (2007).

175. Verreet, B. et al. The characterization of chloroboron (III) subnaphthalocyanine thin films and their application as a donor material for organic solar cells. *J. Mater. Chem.* **19,** 5295–5297 (2009).

176. Ma, B., Woo, C. H., Miyamoto, Y. & Frechet, J. M. J. Solution Processing of a Small Molecule, Subnaphthalocyanine, for Efficient Organic Photovoltaic Cells. *Chem. Mater.* **21,** 1413–1417 (2009).

177. Pandey, R., Zou, Y. & Holmes, R. J. Efficient, bulk heterojunction organic photovoltaic cells based on boron subphthalocyanine chloride-C_{70}. *Appl. Phys. Lett.* **101,** 033308 (2012).

178. Chen, G. et al. Chloroboron (III) subnaphthalocyanine as an electron donor in bulk heterojunction photovoltaic cells. *Nanotechnology* **24,** 484007 (2013).

179. Beaumont, N. et al. Boron Subphthalocyanine Chloride as an Electron Acceptor for High-Voltage Fullerene-Free Organic Photovoltaics. *Adv. Funct. Mater.* **22,** 561–566 (2012).

180. Goldmann, C. et al. Hole mobility in organic single crystals measured by a 'flip-crystal' field-effect technique. *J. Appl. Phys.* **96,** 2080–2086 (2004).

181. Sakai, J., Taima, T. & Saito, K. Efficient oligothiophene:fullerene bulk heterojunction organic photovoltaic cells. *Org. Electron.* **9,** 582–590 (2008).

182. Chu, C.-W., Shao, Y., Shrotriya, V. & Yang, Y. Efficient photovoltaic energy conversion in tetracene-C_{60} based heterojunctions. *Appl. Phys. Lett.* **86,** 243506 (2005).

183. Beaumont, B. N. et al. Acceptor Properties of Boron Subphthalocyanines in Fullerene Free Photovoltaics. *J. Phys. Chem. C* **118,** 14813–14823 (2014).

184. Cnops, K., Rand, B. P., Cheyns, D. & Heremans, P. Enhanced photocurrent and open-circuit voltage in a 3-layer cascade organic solar cell. *Appl. Phys. Lett.* **101,** 143301 (2012).

185. Cnops, K. et al. 8.4% Efficient Fullerene-Free Organic Solar Cells Exploiting Long-Range Exciton Energy Transfer. *Nat. Commun.* **5,** 3406 (2014).

186. Jadhav, P. J., Mohanty, A., Sussman, J., Lee, J. & Baldo, M. A. Singlet exciton fission in nanostructured organic solar cells. *Nano Lett.* **11,** 1495–1498 (2011).

187. Esiner, S., van Eersel, H., Wienk, M. M. & Janssen, R. A. J. Triple Junction Polymer Solar Cells for Photoelectrochemical Water Splitting. *Adv. Mater.* **25,** 2932–2936 (2013).

188. Ameri, T., Khoram, P., Min, J. & Brabec, C. J. Organic ternary solar cells: a review. *Adv. Mater.* **25,** 4245–4266 (2013).

189. Lu, L., Xu, T., Chen, W., Landry, E. S. & Yu, L. Ternary blend polymer solar cells with enhanced power conversion efficiency. *Nat. Photonics* **8,** 716–722 (2014).

190. Yang, Y. et al. High-performance multiple-donor bulk heterojunction solar cells. *Nat. Photonics* **9,** 190–198 (2015).

191. Kim, Y., Shin, M., Kim, H., Ha, Y. & Ha, C.-S. Influence of electron-donating polymer addition on the performance of polymer solar cells. *J. Phys. D: Appl. Phys.* **41,** 225101 (2008).

192. Koppe, M. et al. Near IR Sensitization of Organic Bulk Heterojunction Solar Cells: Towards Optimization of the Spectral Response of Organic Solar Cells. *Adv. Funct. Mater.* **20,** 338–346 (2010).

193. Huang, J. et al. Polymer bulk heterojunction solar cells employing Förster resonance energy transfer. *Nat. Photonics* **7,** 479–485 (2013).

194. Wang, J. C. et al. Short circuit current improvement in planar heterojunction organic solar cells by multijunction charge transfer. *Appl. Phys. Lett.* **100,** 053301 (2012).

195. Heidel, T. D. et al. Reducing recombination losses in planar organic photovoltaic cells using multiple step charge separation. *J. Appl. Phys.* **109,** 104502 (2011).

196. Tan, Z.-K. et al. Suppressing Recombination in Polymer Photovoltaic Devices via Energy-Level Cascades. *Adv. Mater.* **28,** 4131–4138 (2013).

197. Shao, Y., Sista, S., Chu, C.-W., Sievers, D. & Yang, Y. Enhancement of tetracene photovoltaic devices with heat treatment. *Appl. Phys. Lett.* **90,** 103501 (2007).

198. Ichikawa, M., Suto, E., Jeon, H.-G. & Taniguchi, Y. Sensitization of organic photovoltaic cells based on interlayer excitation energy transfer. *Org. Electron.* **11,** 700–704 (2010).

199. Schlenker, C. W. et al. Cascade Organic Solar Cells. *Chem. Mater.* **23,** 4132–4140 (2011).

200. Ichikawa, M., Takekawa, D., Jeon, H.-G. & Banoukepa, G. D. R. Cascade-type excitation energy relay in organic thin-film solar cells. *Org. Electron.* **14,** 814–820 (2013).

201. Luhman, W. A. & Holmes, R. J. Investigation of Energy Transfer in Organic Photovoltaic Cells and Impact on Exciton Diffusion Length Measurements. *Adv. Funct. Mater.* **21,** 764–771 (2011).

202. Scully, S. R. & McGehee, M. D. Effects of optical interference and energy transfer on exciton diffusion length measurements in organic semiconductors. *J. Appl. Phys.* **100,** 034907 (2006).

203. Gommans, H., Schols, S., Kadashchuk, A. & Heremans, P. Exciton Diffusion Length and Lifetime in Subphthalocyanine Films. *J. Phys. Chem. C* **113,** 2974–2979 (2009).

204. Hong, Z. R. et al. Antenna effects and improved efficiency in multiple heterojunction photovoltaic cells based on pentacene, zinc phthalocyanine, and C_{60}. *J. Appl. Phys.* **106,** 064511 (2009).

205. Zhou, Y., Taima, T., Kuwabara, T. & Takahashi, K. Efficient Small-Molecule Photovoltaic Cells Using a Crystalline Diindenoperylene Film as a Nanostructured Template. *Adv. Mater.* **25,** 6069–6075 (2013).

206. Griffith, O. L. & Forrest, S. R. Exciton Management in Organic Photovoltaic Multidonor Energy Cascades. *Nano Lett.* **14,** 2353–2358 (2014).

207. Fitzner, R. et al. Correlation of π-conjugated oligomer structure with film morphology and organic solar cell performance. *J. Am. Chem. Soc.* **134,** 11064–11607 (2012).

208. Chen, Y.-H. et al. Vacuum-deposited small-molecule organic solar cells with high power conversion efficiencies by judicious molecular design and device optimization. *J. Am. Chem. Soc.* **134,** 13616–13623 (2012).

209. Cnops, K., Voroshazi, E., De Ruijter, C. H., Heremans, P. & Cheyns, D. Organic photovoltaic cell relying on energy transfer with over 20% efficiency in indoor lighting. in *40th IEEE-PVSC* 143–146 (2014).

210. Steim, R. et al. Organic photovoltaics for low light applications. Sol. Energy Mater. *Sol. Cells* **95,** 3256–3261 (2011).

211. Yang, P. C., Chan, I. M., Lin, C. H. & Chang, Y. L. Thin film solar cells for indoor use. in *37th IEEE-PVSC* 696–698 (2011).

212. Reich, N. H. et al. Crystalline silicon cell performance at low light intensities. *Sol. Energy Mater. Sol. Cells* **93,** 1471–1481 (2009).

213. Reich, N. H., van Sark, W. G. J. H. M. & Turkenburg, W. C. Charge yield potential of indoor-operated solar cells incorporated into Product Integrated Photovoltaic (PIPV). *Renew. Energy* **36,** 642–647 (2011).

214. Hosoya, M. et al. Module Development for Organic Thin-Film Photovoltaics. in *28th Eur. Photovolt. Sol. Energy Conf.* 2236–2238 (2013).

215. Schmidt, H. et al. Efficient semitransparent inverted organic solar cells with indium tin oxide top electrode. *Appl. Phys. Lett.* **94,** 243302 (2009).

216. Ameri, T. et al. Fabrication, optical modeling, and color characterization of semitransparent bulk-heterojunction organic solar cells in an inverted structure. *Adv. Funct. Mater.* **20,** 1592–1598 (2010).

217. Chen, C. C. et al. Visibly transparent polymer solar cells produced by solution processing. *ACS Nano* **6,** 7185–7190 (2012).

218. Lee, J. Y., Connor, S. T., Cui, Y. & Peumans, P. Semitransparent organic photovoltaic cells with laminated top electrode. *Nano Lett.* **10,** 1276–1279 (2010).

219. Colsmann, A. et al. Inverted semi-transparent organic solar cells with spray coated, surfactant free polymer top-electrodes. *Sol. Energy Mater. Sol. Cells* **98,** 118–123 (2012).

220. Lee, Y. Y. et al. Top laminated graphene electrode in a semitransparent polymer solar cell by simultaneous thermal annealing/releasing method. *ACS Nano* **5,** 6564–6570 (2011).

221. Liu, Z. et al. The application of highly doped single-layer graphene as the top electrodes of semitransparent organic solar cells. *ACS Nano* **6,** 810–818 (2012).

222. Kim, Y. H. et al. Semi-transparent small molecule organic solar cells with laminated free-standing carbon nanotube top electrodes. *Sol. Energy Mater. Sol. Cells* **96,** 244–250 (2012).

223. Tanaka, S. et al. Semitransparent organic photovoltaic cell with carbon nanotube-sheet anodes and Ga-doped ZnO cathodes. *Synth. Met.* **159,** 2326–2328 (2009).

224. Chen, K.-S. et al. Semi-transparent polymer solar cells with 6% PCE, 25% average visible transmittance and a color rendering index close to 100 for power generating window applications. *Energy Environ. Sci.* **5,** 9551-9557 (2012).

225. Chen, C.-C. et al. High-performance semi-transparent polymer solar cells possessing tandem structures. *Energy Environ. Sci.* **6,** 2714–2720 (2013).

226. Frangioni, J. V. In vivo near-infrared fluorescence imaging. *Curr. Opin. Chem. Biol.* **7,** 626–634 (2003).

227. Schmitt, J. M., Xiang, S. H. & Yung, K. M. Differential absorption imaging with optical coherence tomography. *J. Opt. Soc. Am. A* **15,** 2288-2296 (1998).

228. Källhammer, J.-E. Imaging:The road ahead for car night-vision. *Nat. Photonics* **sample**, 12–13 (2006).

229. Lenzen, R., Hofmann, R., Bizenberger, P. & Tusche, A. CONICA: The high resolution near-infrared camera for the ESO VTL. in *Proc. SPIE* **3354,** 606–614 (1998).

230. Barton, J., Cannata, R. & Petronio, S. InGaAs NIR focal plane arrays for imaging and DWDM applications. in *Proc. SPIE* **4721,** 37–47 (2002).

231. Cohen, M. J. & Olsen, G. H. Room temperature InGaAs camera for NIR imaging. in *Proc. SPIE* **1946,** 436–443 (1993).

232. Liu, H. C. et al. A study of GaAs/AlGaAs p-type quantum well infrared photodetectors with different barrier heights. *J. Appl. Phys.* **83,** 585–587 (1998).

233. Martyniuk, P. & Rogalski, A. Quantum-dot infrared photodetectors: Status and outlook. *Prog. Quantum Electron.* **32,** 89–120 (2008).

234. Ukei, K. Lead phthalocyanine. *Acta Crystallogr.* **B29**, 2290–2292 (1973).

235. Braun, S., Salaneck, W. R. & Fahlman, M. Energy-Level Alignment at Organic/Metal and Organic/Organic Interfaces. *Adv. Mater.* **21,** 1450–1472 (2009).

236. Scott, J. C. & Malliaras, G. G. Charge injection and recombination at the metal–organic interface. *Chem. Phys. Lett.* **299,** 115–119 (1999).

237. Kröger, M. et al. Temperature-independent field-induced charge separation at doped organic/organic interfaces: Experimental modeling of electrical properties. *Phys. Rev. B* **75,** 235321 (2007).

238. Keivanidis, P. E., Ho, P. K. H., Friend, R. H. & Greenham, N. C. The Dependence of Device Dark Current on the Active-Layer Morphology of Solution-Processed Organic Photodetectors. *Adv. Funct. Mater.* **20,** 3895–3903 (2010).

239. Bergemann, K., Amonoo, J., Song, B., Green, P. F. & Forrest, S. R. Surprisingly High Conductivity and Efficient Exciton Blocking in Fullerene:Wide-Energy-Gap Small Molecule Mixtures. *Nano Lett.* **15,** 3994–3999 (2015).

240. Campbell, I. H. & Crone, B. K. A near infrared organic photodiode with gain at low bias voltage. *Appl. Phys. Lett.* **95,** 263302 (2009).

241. Zimmerman, J. D. et al. Porphyrin-tape/C_{60} organic photodetectors with 6.5% external quantum efficiency in the near infrared. *Adv. Mater.* **22,** 2780–2783 (2010).

242. Rauch, T. et al. Near-infrared imaging with quantum-dot-sensitized organic photodiodes. *Nat. Photonics* **3,** 332–336 (2009).

243. McDonald, S. A. et al. Solution-processed PbS quantum dot infrared photodetectors and photovoltaics. *Nat. Mater.* **4,** 138–142 (2005).

244. Arnold, M. S. et al. Broad Spectral Response Using Carbon Nanotube / Organic Semiconductor / C_{60} Photodetectors. *Nano Lett.* **9,** 3354–3358 (2009).

245. Griffiths, J. & Roozpeikar, B. Synthesis and electronic absorption spectra of dicyano-derivatives of 4-diethylaminoazobenzene. *J. Chem. Soc., Perkin Trans. 1,* 42–45 (1976).

246. Marcuccio, S. M. et al. Binuclear phthalocyanines covalently linked through two- and four-atom bridges. *Can. J. Chem.* **63,** 3057–3069 (1985).

247. Claessens, C. G., Vicente-Arana, M. J. & Torres, T. Post-assembly error-checking in subphthalocyanine based M_3L_2 metallosupramolecular capsules. *Chem. Commun.* **47,** 6378–6380 (2008).

248. Fulford, M. V. et al. Crystal Structures, Reaction Rates, and Selected Physical Properties of Halo-Boronsubphthalocyanines (Halo = Fluoride, Chloride, and Bromide). *J. Chem. Eng. Data* **57,** 2756–2765 (2012).

Curriculum vitae

Kjell Cnops was born in Leuven, Belgium on December 10, 1988. He obtained his degree of Bachelor in Physics in 2009, and his degree of Master in Nanoscience and Nanotechnology in 2011 at the University of Leuven. His master's thesis focused on the growth of thin organic semiconducting films by organic vapor phase deposition, and received the 2010-2011 ArcelorMittal master's thesis award. Inspired by the research in the field of organic electronics, he started his doctoral research in September 2011 at imec to pursue his Ph.D. degree at the Department of Electrical Engineering (ESAT) of the University of Leuven. The topic of his doctoral research included the development of organic solar cells and organic photodetectors based on small-molecule semiconductors. The scientific impact of his publications in international journals was acknowledged by the 2013 imec scientific excellence award.

List of publications

Journal publications

- **Kjell Cnops**, Barry P. Rand, David Cheyns, Paul Heremans, Enhanced photocurrent and open-circuit voltage in a 3-layer cascade organic solar cell, *Applied Physics Letters* **101,** 14, 143301 (2012).

- **Kjell Cnops**, Barry P. Rand, David Cheyns, Bregt Verreet, Max A. Empl, Paul Heremans, 8.4% efficient fullerene-free organic solar cells exploiting long-range exciton energy transfer, *Nature Communications* **5,** 3406 (2014).

- **Kjell Cnops,** German Zango, Jan Genoe, Paul Heremans, M. Victoria Martinez-Diaz, Tomas Torres, David Cheyns, Energy Level Tuning of Non-fullerene Acceptors in Organic Solar Cells, *Journal of the American Chemical Society* **137,** 8991–8997 (2015).

- Christian B. Nielsen, Eszter Voroshazi, Sarah Holliday, **Kjell Cnops**, Barry P. Rand, Iain McCulloch, Efficient truxenone-based acceptors for organic photovoltaics, *Journal of Materials Chemistry A* **1,** 73-76 (2013).

- Bregt Verreet, **Kjell Cnops**, David Cheyns, Paul Heremans, André Stesmans, German Zango, Christiaan Claessens, Tomas Torres, Barry P. Rand, Decreased recombination through the use of a non-fullerene acceptor in a 6.4% efficient organic planar heterojunction solar cell, *Advanced Energy Materials* **4,** 1301413 (2014).

- Christian B. Nielsen, Eszter Voroshazi, Sarah Holliday, **Kjell Cnops**, David Cheyns, Iain McCulloch, Electron-deficient truxenone derivatives and their use in organic photovoltaics, *Journal of Materials Chemistry A* **2,** 12348-12354 (2014).

Conference contributions

- **Kjell Cnops**, Bregt Verreet, David Cheyns, Barry P. Rand, Paul Heremans, Subphthalocyanines as versatile donors and acceptors in high-efficiency organic solar cells, *MRS Spring Meeting 2013*, San Francisco, US (2013).

- **Kjell Cnops**, Bregt Verreet, David Cheyns, Barry P. Rand, Paul Heremans, Subphthalocyanines as effective donors and acceptors in high-efficiency organic solar cells, *Conference on Hybrid and Organic Photovoltaics – HOPV 2013*, Seville, Spain (2013).

- **Kjell Cnops**, Barry P. Rand, David Cheyns, Bregt Verreet, Max A. Empl, Paul Heremans, Fullerene-free organic solar cells exploiting long-range exciton energy transfer, *SPIE Photonics Europe Conference: Organic Photonics*, Brussels, Belgium (2014).

- **Kjell Cnops**, Eszter Voroshazi, Carl de Ruijter, Paul Heremans, David Cheyns, Organic photovoltaic cell relying on energy transfer with over 20% efficiency in indoor lighting, *IEEE Photovoltaic Specialists Conference*, Denver, US (2014).

- **Kjell Cnops**, David Cheyns, Bregt Verreet, Paul Heremans, German Zango, Victoria Martinez-Diaz, Tomas Torres, High-efficiency organic solar cells utilizing subphthalocyanine derivatives as non-fullerene acceptors, *10th International Conference on Electroluminescence and Optoelectronic Devices - ICEL-10*, Cologne, Germany (2014).

- **Kjell Cnops**, Bregt Verreet, David Cheyns, Paul Heremans, Victoria Martinez-Diaz, German Zango, Tomas Torres, Subphthalocyanine Derivatives as Non-Fullerene Acceptors in High-Efficiency Organic Solar Cells, *MRS Fall Meeting 2014*, Boston, US (2014).

- Christian B. Nielsen, Eszter Voroshazi, Sarah Holliday, **Kjell Cnops**, Barry P. Rand, Iain McCulloch, Truxenone-based Small Molecule Acceptors for Efficient Organic Photovoltaic Devices, *MRS Spring Meeting 2013*, San Francisco, US (2013).

- Sarah Holliday, Christian B. Nielsen, Eszter Voroshazi, **Kjell Cnops**, Barry P. Rand, Iain McCulloch, Truxenone-based small molecule acceptors for efficient organic photovoltaic devices, *11th International Symposium on Functional π-Electron Systems*, Bordeaux, France (2013).

- Eszter Voroshazi, Griet Uytterhoeven, Paola Favia, **Kjell Cnops**, David Cheyns, Root-cause analysis of device failure in inverted P3HT:PCBM cells, *International Summit on Organic Photovoltaic Stability*, Chambery, France (2013).

- Barry P. Rand, David Cheyns, **Kjell Cnops**, Bregt Verreet, Incorporating multiple absorbers to improve spectral absorption in high efficiency organic solar cells, *SPIE Optics + Photonics 2014*, San Diego, US (2014).

- David Cheyns, **Kjell Cnops**, Jeffrey G. Tait, Mathieu Turbiez, Versatile Recombination Zone for Organic Solar Cells, *MRS Fall Meeting 2014*, Boston, US (2014).

- Eszter Voroshazi, Griet Uytterhoeven, Paola Favia, Hugo Bender, Thierry Conard, **Kjell Cnops**, David Cheyns, Root-cause failure analysis reveals harmful interaction between non-adjacent MoO_3 and Al layers, *MRS Fall Meeting 2014,* Boston, US (2014).

- Robert Gehlhaar, David Cheyns, Eszter Voroshazi, **Kjell Cnops**, Afshin Hadipour, Luuk van Willigenburg, Tom Aernouts, Fullerene-free organic photovoltaic submodules and semitransparent submodule assemblies, *European Photovoltaic Solar Energy Conference and Exhibition – EUPVSEC*, Amsterdam, Netherlands (2014).

Patents

- Barry P. Rand, **Kjell Cnops**, Organic photovoltaic cells with enhanced photocurrent, WO 2015/011060 A1, 29 January 2015.